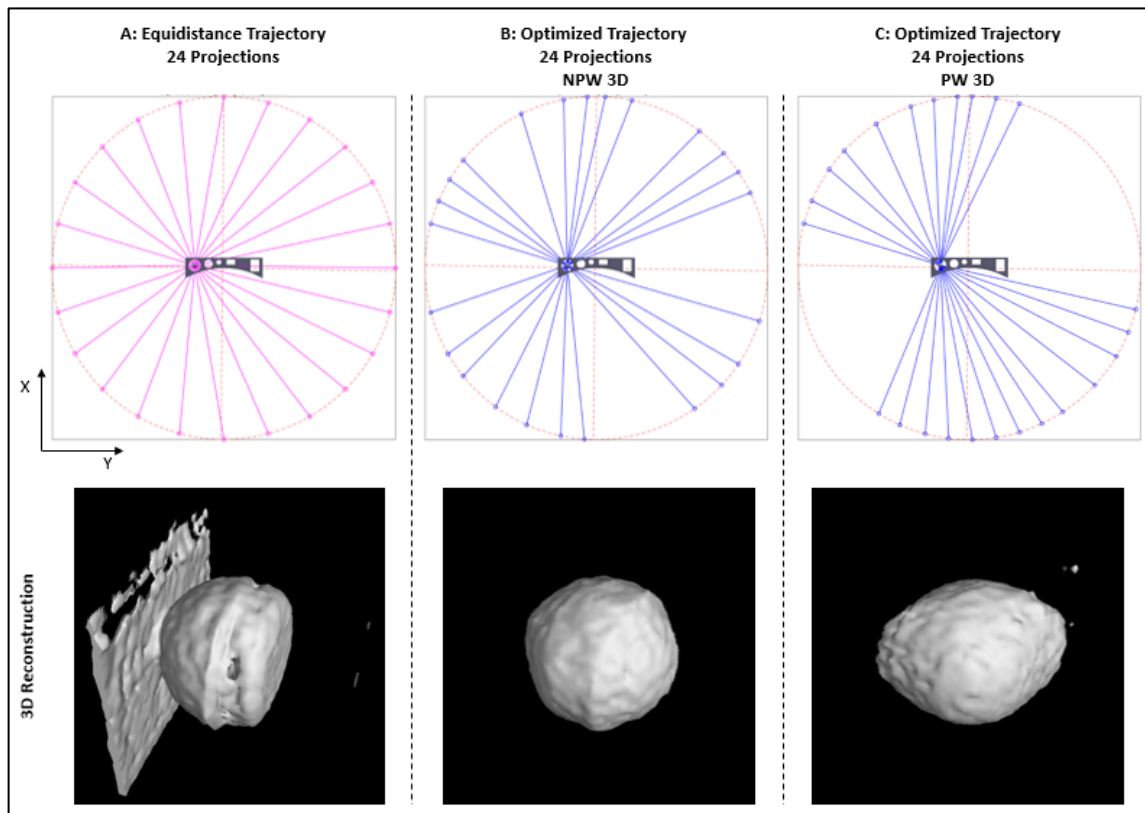


Evaluation of Observer Model Performance in Sparsely Sampled Cone Beam Computed Tomography

Fehmi Bouhaouel



Masterarbeit

Fakultät für Maschinenwesen

Studiengang: Luft- und Raumfahrttechnik

Abgabedatum: 01.05.2019

Betreuer: Fabian Bauer, M.Sc. (Siemens)

Dr. rer. nat. Katja Pinkert (TUM)

Prüfer: Prof. Dr.-Ing. Christian Große

TECHNISCHE UNIVERSITÄT MÜNCHEN - Lehrstuhl für Zerstörungsfreie Prüfung

Prof. Dr.-Ing. habil. Christian Große

Baumbachstr. 7 · 81245 München · Tel.+49-89-289-27221 · www.zfp.tum.de

Aufgabenstellung der Masterarbeit

Titel: Evaluation of Observer Model Performance in Sparsely Sampled Cone Beam Computed Tomography

Betreuer: Fabian Bauer, M.Sc. (Siemens) Dr. rer. nat. Katja Pinkert (TUM)
Tel: +49 (89) 636-631244 Tel.: 089 / 289-27218
fabianbauer@siemens.com katja.pinkert@tum.de

Ausgangssituation und Motivation:

Die industrielle Röntgen Computertomographie (CT) stellt ein häufig verwendetes und sehr vielfältiges Hilfsmittel für die Zerstörungsfreie Prüfung dar. Die CT bietet dabei die einzigartige Möglichkeit, ein vollständiges 3D Volumen eines vorhandenen Bauteils zu liefern und hat sich als exzellentes Werkzeug in der Qualitätssicherung etabliert. Die Scandauer einer Prüfung ist jedoch im Vergleich mit anderen typischen Methoden der ZfP relativ hoch, was bisher den Routineeinsatz in der Inline-Bauteilprüfung erschwert.

Um den Messvorgang zu beschleunigen, können im Rahmen des Scans einzelne Projektionsbilder ausgelassen werden, deren Informationsgehalt vergleichsweise gering ist. Zur Quantifizierung der vorhandenen Bildinformation werden aktuell verschiedene Beobachtermodelle herangezogen, die jedoch weitestgehend auf dem menschlichen Seheindruck des Bildes beruhen. Diese Metriken sind zwar prinzipiell geeignet, betrachten jedoch nicht den tatsächlichen Informationsgehalt oder die Anforderungen des verwendeten Rekonstruktionsalgoritmus.

Aufgabenstellung und Zielsetzung:

Im Rahmen dieser Masterarbeit sollen verschiedene Observermodelle und Kennwerte zur Quantifizierung der Bildqualität auf ihre Brauchbarkeit in der Computertomographie mit reduzierter Projektionszahl (sparsely sampled CT) implementiert und untersucht werden. Hierfür sollen die verschiedenen Metriken auf simulierte Projektionen bereits bekannter Bauteile angewendet und Rekonstruktionen mit den besten Aufnahmewinkel erzeugt werden. Diese werden anschließend mit dem optimalen Rekonstruktionsergebnis verglichen um eine empirische Einschätzung hinsichtlich ihrer Brauchbarkeit geben zu können. Das Ergebnis der Simulationen soll anschließend mittels echter Messungen verifiziert werden.

Schwerpunkte der Masterarbeit:

- Einarbeitung in die Thematik und Software, Literaturrecherche.
- Implementierung verschiedener Bewertungsmetriken für Einzelprojektionen.
- Erzeugung eines optimalen Referenzergebnisses für mehrere Bauteile.
- Bestimmung von Projektionssets anhand unterschiedlicher Metriken.
- Vergleich der Rekonstruktionsergebnisse mit der Referenz anhand geeigneter Kennwerte.
- Abgleich der Simulationsergebnisse durch echte CT-Messungen.
- Anfertigung der schriftlichen Ausarbeitung unter Berücksichtigung des Layouts des Lehrstuhls.
- Vorstellung der Ergebnisse und Abgabe aller Schriftstücke und Daten in elektronischer Form.

Schwerpunkte der Masterarbeit:

- Selbstständige und strukturierte Arbeitsweise.
- Motivation und Begeisterung für wissenschaftliches Arbeiten.
- Grundkenntnisse im Bereich der Computertomographie und der Optik.
- Programmierkenntnisse (C++, Matlab) sind wünschenswert.
- Sehr gute Englischkenntnisse.

Die Durchführung der Masterarbeit erfolgt in Kooperation mit einem Industriepartner, was eine Präsenz u.a. am Firmensitz der Siemens AG in München erfordert.

Die Bewertungskriterien für die Masterarbeit liegen vor und sind dem Masteranden bekannt. Die Vorstellung der Ergebnisse erfolgt in einem etwa 30-minütigen Vortrag am Lehrstuhl, an den sich die Notenfindung anschließt. Zu diesem Zeitpunkt liegt die korrigierte Endversion der Masterarbeit den Prüfern vor.

Beginn der Masterarbeit: sofort

Voraussichtliche Dauer: 6 Monate

Selbstständigkeitserklärung

Fehmi Bouhaouel

Helene Mayer Ring 7A/916

80809 München

Matrikelnummer: 03634166

Hiermit erkläre ich, die vorliegende Masterarbeit selbstständig verfasst zu haben. Es wurden keine anderen als die in der Arbeit angegebenen Quellen und Hilfsmittel benutzt. Die wörtlichen oder sinngemäß übernommenen Zitate habe ich als solche kenntlich gemacht.

Die vorliegende Masterarbeit entstand unter wissenschaftlicher und inhaltlicher Anleitung durch meine Betreuer. Zentrale Ideen und Konzepte wurden gemeinschaftlich mit ihm/ihr erarbeitet.

München, den 01.05.2019

FEHMI BOUHAOUEL

Kurzfassung

Bei der zerstörungsfreien Prüfung spielt die Röntgen-Computertomographie (CT) eine wichtige Rolle bei der Untersuchung von Objekten, wie zum Beispiel, zur Fehlererkennung oder für metrologische Messungen. Heutige CT-Anwendungen verwenden Standardtrajektorien wie die typischen kreisförmigen oder spiralförmigen Bahnen in Kombination mit dem Filtered Back-projection (FBP)-Rekonstruktionsalgorithmus. Große oder stark absorbierende Objekte verursachen jedoch Absorptionsprobleme in bestimmten Richtungen. In solchen Fällen können Bestandteile des Objekts aufgrund fehlender Informationen nicht richtig rekonstruiert werden.

In dieser Arbeit stellen wir zunächst einen aufgabenbasierten Trajektorienoptimierungsalgorithmus vor, der sich auf Basis der CAD-Geometrie eines Bauteils auf die Ermittlung der idealen Projektionen, welche die maximale Information für die anschließende Rekonstruktion beinhalten, konzentriert. Im Gegensatz zu anderen Ansätzen, die den Rekonstruktionsalgorithmus selbst verbessern, liegt der Schwerpunkt unserer Arbeit auf der Optimierung vor der eigentlichen Akquisition, d.h. bevor der tatsächliche CT-Scan stattfindet. Der vorgeschlagene Algorithmus verwendet einen aufgabenbasierten Detektionsindex, der als Zielfunktion auf mehreren numerischen Modellbeobachtern basiert.

Anschließend bewerten wir qualitativ und quantitativ die Ergebnisse verschiedener Modellbeobachter im Vergleich zu verschiedenen Eigenschaften des Features innerhalb des Objekts. Diese Modellbeobachter integrieren Vorwissen über das Feature selbst sowie über das Rauschen und die räumliche Auflösung. Beide Bildmerkmale werden unter Verwendung von Prädiktoren auf der Grundlage des Penalized Likelihood (PL) Rekonstruktionsalgorithmus approximiert, um eine effiziente Berechnung zu ermöglichen.

Die Ergebnisse zeigen, dass unser Optimierungsalgorithmus im Vergleich zu einer früheren Implementierung in der Literatur eine genauere und schnellere Trajektorienoptimierung bietet. Dies ermöglicht es uns, die Beobachtermodelle auf unterschiedliche Eigenschaften zu testen. Generell wurde bei allen Modellen und bei allen Aufgaben eine Verbesserung der Qualität der Rekonstruktion erreicht. Dennoch legen unsere Ergebnisse nahe, dass es kein optimales Modell für alle möglichen Anwendungen gibt. Stattdessen ist die Wahl des bestgeeigneten Beobachtermodells abhängig vom Akquisitionsschema ab (z. B. Anzahl der Projektionen, Komplexität des Features, usw.).

Schlagwörter: Computertomographie, Aufgabenbasierte Beobachtermodelle, Aufgabenbasierte Trajektorienoptimierung, Metriken für Bildqualität, Modulationsübertragungsfunktion, Rauschleistungsspektrum

Abstract

In industrial non-destructive testing, X-ray computed tomography (CT) plays an important role in the investigation of objects, i.e. for defect detection or for dimensional metrology. Currently, CT applications use standard trajectories like the circular or helical orbits in combination with the Filtered Backprojection (FBP) reconstruction algorithm. However, large or strongly attenuating objects cause absorption problems in specific directions. In such cases, specific features of the object cannot be sufficiently reconstructed due to the lack of information about it.

In this thesis, we firstly introduce a task-based trajectory optimization algorithm that focuses on identifying preferable projections that maximize the information content for the subsequent reconstruction based on the CAD data of an object. Unlike other approaches that improve the reconstruction algorithm itself, our work focuses on pre-acquisition optimization, i.e. optimizing the acquisition trajectory before the actual scan takes place. The proposed algorithm uses a task-based detectability index based on different numerical model observers as objective functions.

Secondly, we assess qualitatively and quantitatively the performance of different of such model observers versus different properties of the feature inside the object. These model observers incorporate knowledge about the feature itself and about the noise and spatial resolution around it. Both image characteristics will be approximated using predictors based on the Penalized-Likelihood (PL) reconstruction algorithm in order to reduce the computational effort.

Our optimization algorithm provides more accurate and faster trajectory optimization compared to an earlier implementation in the literature. This has allowed us to test the various model observers for different properties. In general, an improvement of the reconstruction quality was achieved with all model observers and for all imaging tasks. We were also able to assign the performance of these models to specific acquisition schemes, e.g. the NPW model observer has provided better results for a small number of projections, while the PW model observer was a better choice for a large number. We concluded that there is no model that is optimal for all cases, but instead depends on the acquisition scheme (e.g. number of projections, complexity of the feature, etc.).

Keywords:

Computed Tomography, Task-Based Model Observers, Task-Based Trajectory Optimization, Image Quality Metrics, Modulation Transfer Function, Noise Power Spectrum

Table of Contents

Aufgabenstellung der Masterarbeit	I
Selbstständigkeitserklärung	III
Kurzfassung	IV
Abstract	V
Table of Contents	VI
List of Figures	VIII
List of Tables	XI
List of Notations	XII
1 Introduction	1
2 Fundamentals of Computed Tomography	3
2.1 Introduction	3
2.2 Standard Acquisition Trajectories:	5
2.3 System Matrix	9
2.4 Lambert-Beer's Law	12
3 Reconstruction Methods	13
3.1 Iterative Reconstruction Technique	13
3.1.1 Algebraic Reconstruction Technique	14
3.1.2 Penalized-Likelihood Reconstruction	15
3.2 Filtered Backprojection	16
3.3 Quality metrics for the evaluation of reconstructions	20
4 Image Quality Assessment Metrics and Approaches	22
4.1 Traditional Metrics and Approaches	22
4.2 Task-Based Quality Assessment	25
5 Model Observers	28
5.1 Pre-Whitening Model Observer (PW)	29
5.2 Non-Pre-Whitening Model Observer (NPW)	35
5.3 The Region-of-Interest Observer (ROI)	37
5.4 Hotelling Observer (HO)	38

5.5 Channelized Hotelling Observer (CHO)	39
5.6 Definition of the parameters in Model Observers	44
5.6.1 MTF & NPS	44
5.6.2 Task Function W	49
5.6.3 Eye Filter E	51
5.6.4 Internal Noise N	53
6 Methods	54
6.1 Trajectory Optimization for 3D features	54
6.1.1 Flowchart of the task-based 3D detectability index	54
6.1.2 Object module	56
6.1.3 Simulation module	57
6.1.4 Optimization module	59
6.1.5 Reconstruction module	64
6.1.6 Evaluation module	65
6.2 Trajectory Optimization for 2D features	66
6.2.1 Flowchart of the task-based 2D detectability index	66
6.2.2 Object module	66
6.2.3 Simulation module	66
6.2.4 Observer module	68
6.2.5 Optimization module	69
6.2.6 Reconstruction module	69
6.2.7 Evaluation module	70
7 Results and Discussion	73
7.1 Trajectory Optimization for 3D features	73
7.1.1 Feature 1: Sphere	73
7.1.2 Feature 2: Cylinder	82
7.2 Trajectory Optimization for 2D features	87
8 Conclusions	90
Bibliography	95
Appendix	100

List of Figures

Figure 2.1: Geometry and notation for a cone beam CT setup with opening angle θ [Schrapp 2015]	4
Figure 2.2: Overview of modern CT scanners used in the medical and industrial fields. The figures are reproduced from [Schoener 2012] [Fraunhofer EZRT 2019]	5
Figure 2.3: Overview of different acquisition geometries. Source, detector and trajectory are marked as red, black and blue. The figures are adapted from [Buzug 2008]	6
Figure 2.4: Extension of the simple circular orbit to fulfill the Tuy-Smith sufficiency condition	7
Figure 2.5: Typical acquisition geometries for long objects. The figures are reproduced from [Siemens 2016]	8
Figure 2.6: Visualization of the weighting factors A_{ji} in a 2D algebraic forward projection model for cone-beam configuration	9
Figure 2.7: Schematic overview of the relation between the system matrix, the attenuation values of the object and the measurements for multiple projections	11
Figure 3.1: The relevant steps of iterative reconstruction algorithms [Schrapp 2015]	14
Figure 3.2: Illustration of the penalized pixels in a 2D slice reconstruction	16
Figure 3.3: Workflow of the filtered back-projection (FBP) with a ramp filter [Schrapp 2015]	17
Figure 3.4: (A) Illustration of the effect of the high-pass filtering. Left: Unfiltered back- projection. Right: Filtered Back-projection with Ram-Lak filter ($G(q) = q $) [Buzug 2008]. (B) Filter kernels of the Ram-Lak filter and the Shepp-Logan filter [Lee et al. 2011]	18
Figure 4.1: Example of projections selection for equiangular (A) and entropy-based acquisition (B) [Placidi et al. 1995]	23
Figure 4.2: Reconstruction of a square with projections covering the X-rays tangent to the edges (A) and projections shifted by 45° [Fischer 2014]	24
Figure 4.3: Probability distribution of the likelihood-ratio decision function for the hypothesis H_1 (left) and H_2 (right)	26
Figure 4.4: Probability distributions curves for two different signal strengths and two different noise levels. The figures are reproduced from [Heeger 1997]	27
Figure 5.1: Three examples of noise models: (A) White Gaussian Background, (B) Correlated Gaussian Background, and (C) Lumpy Background [Zhangh 2014]	30
Figure 5.2: Unlike the human eye, for an ideal observer like the PW model observer both disks are equally difficult to distinguish from the background	33
Figure 5.3: Different task functions presented in spatial (first column) and frequency domain (second and third columns). The value bars have no unit, like the features too	50

Figure 5.4: Use of the discrete Laplace operator to model the edge profile of the feature. (A) The circle in spatial domain. (B) The edge profile differentiated by the Laplace operator. (C) The task function of the edge profile of the circle in frequency domain	51
Figure 5.5: The Human Contrast Sensitivity Function. It has a peak at approximately $f = 1$ to 8 [Archibald et al. 2009]	52
Figure 5.6: The spatial frequency defines the number of cycles seen at the eye per 1 degree. Adopted from [Archibald et al. 2009]	52
Figure 6.1: Flowchart of the task-driven trajectory optimization for 3D features	55
Figure 6.2: A customized phantom used to characterize the performance of the model observer	56
Figure 6.3: GUI of the X-ray simulation tool aRTist	58
Figure 6.4: Reconstruction of a cylinder for two different inclination angles. (A) shows strong FDK artifacts. The figures are reproduced from [Xue et al. 2015]	58
Figure 6.5: A greedy algorithm is used as an optimization algorithm to find out the set of ideal projections	60
Figure 6.6: Example of a reconstruction of a low-contrast sphere for varying values of β [Uneri et al. 2018]	62
Figure 6.7: Flowchart of the task-driven trajectory optimization for 2D features	67
Figure 6.8: 2D and 3D visualization of the eye filter. f_x and f_y are the spatial frequencies in the x and y directions, respectively	68
Figure 6.9: Spatial form of the first 15 Gabor channels	71
Figure 6.10: Images of the used 3 S-DOG channels and the first 5 D-DOG channels	72
Figure 6.11: 2D and 3D representation of the used SQR channels	72
Figure 7.1: Phantom with the indicated sectional views (XY, XZ and YZ) for each feature (Sphere and Cylinder)	73
Figure 7.2: Four FDK reconstructions of the phantom with focus on the sphere are shown. A: Reference reconstruction with full angular range (360 projections). B: Reconstruction with 8 equidistance distributed projections. C and D: Reconstructions with 8 projections selected based on the NPW and PW model observers, respectively	74
Figure 7.3: Illustration of the task-based optimized trajectories with 8 projections using the PW and NPW model observers for the feature “Sphere”	75
Figure 7.4: Trajectory optimization evaluated with 24 projections. As in Figure 7.2, both model observers improve the quality of the reconstruction compared with a reconstruction with 24 equidistance distributed projections	77
Figure 7.5: Illustration of the task-based optimized trajectories with 24 projections using the PW and NPW model observers	78
Figure 7.6: Trajectory optimization evaluated with 90 projections. For a high number of projections, the PW model observer improves the quality of the	

- reconstruction better than the NPW model observer. The equidistance trajectory still shows some artifacts 79
- Figure 7.7: Map of the normalized detectability index for each iteration of the trajectory optimization algorithm. The detectability index is shown over all circular angles for both the PW and NPW model observers. In each iteration the projection with the highest detectability index is chosen. The dotted blue line indicates the selected projection 81
- Figure 7.8: Four FDK reconstructions of the phantom with focus on the Cylinder are plotted. A: Reference reconstruction with 360 projections. B: Reconstruction with 18 equidistance distributed projections. C and D: Reconstructions with 18 projections selected based on the NPW and PW model observers, respectively 83
- Figure 7.9: Illustration of the task-based optimized trajectories with 18 projections using the PW and NPW model observers for the feature “Cylinder” 83
- Figure 7.10: Trajectory optimization evaluated with 24 projections. As in Figure 7.8, both model observers improved considerably the quality of the reconstruction compared with a reconstruction with 24 equidistance distributed projections 85
- Figure 7.11: Trajectory optimization evaluated with 90 projections. For a high number of projections, the PW model observer improves the quality of the reconstruction better than the NPW model observer. The equidistance trajectory and the NPW-based optimized trajectory still show some artifacts 86
- Figure 7.12: Reconstruction of a single slice with 18, 24 and 90 equidistant projections. The same slice is also reconstructed with 18, 24 and 90 optimized projections based on five different 2D model observers 89

List of Tables

Table 5-1: Parameters for S-DOG and D-DOG channel models	42
Table 6-1: Detectability Index for various 3D model observer	61
Table 6-2: Measurement and prediction formulas for MTF and NPS	61
Table 6-3: Detectability Index for various 2D model observer	69
Table 7-1: Quantitative evaluation of standard trajectories with 360 and 8 equidistant distributed projections and optimized trajectories for a set of 8 projections with NPW and PW model observers in comparison to the reference reconstruction with 2000 projections (lower values of SD and RMSE correspond to better results)	75
Table 7-2: Quantitative evaluation of standard trajectories with 360 and 18 equidistant distributed projections and optimized trajectories for a set of 18 projections with NPW and PW model observers in comparison to the reference reconstruction with 2000 projections	82
Table 7-3: Quantitative evaluation (SD and RMSE) of the optimized trajectories for different number of projections (N). The CHO model observers serve here to calculate the test statistic L for the set of projections selected by the NPW- or PW-based model observer	88

List of Notations

ART	Algebraic Reconstruction Technique
CBCT	Cone-Beam Computed Tomography
CHO	Channelized Hotelling Observer
CSF	Contrast Sensitivity Function
CT	Computed Tomography
CUDA	Compute Unified Device Architecture
DFT	Discrete Fourier Transform
FBP	Filtered-Backprojection
FDK	Reconstruction Algorithm developed by Feldkamp, Davis and Kress
HO	Hotelling Observer
MO	Model Observer
MTF	Modulation Transfer Function
NPS	Noise Power Spectrum
NPW	Non-Pre-Whitening Model Observer
NPWE	Non-Pre-Whitening Model Observer with Eye Filter
NPWEi	Non-Pre-Whitening Model Observer with Eye Filter and Internal Noise
PL	Penalized-Likelihood Reconstruction
PSF	Point Spread Function
PW	Pre-Whitening Model Observer
PWEi	Pre-Whitening Model Observer with Eye Filter and Internal Noise
ROI	Region of Interest
SNR	Signal to Noise Ratio
SOD	Source-Object Distance
SDD	Source-Detector Distance
VOI	Volume-of-Interest

1 Introduction

The correct and targeted quantification of image quality in computed tomography (CT) is essential for several reasons: not only does this serve as a tool for evaluating and assessing imaging systems performance, it also provides the ability to optimize the acquisition parameters such as the source-detector trajectory or the X-ray intensity [Fischer et al. 2016].

In the literature, there are many physical metrics for image quality. Several standard approaches, such as Signal-to-Noise Ratio (SNR), Modulation Transfer Function (MTF), or Noise Power Spectrum (NPS), can characterize the properties of an imaging system to some degree. However, since they do not consider the objective of the imaging system, they may not be very meaningful for assessing its imaging performance. In order to counteract these limitations, Robert Wagner proposed in his paper of 1972 to best define the image quality by considering the task that the image is to fulfill [Wagner et al. 1972]. For example, micro cracks detection requires an image of high spatial resolution to enhance sensitivity towards small objects while an edge detection can be best performed on an image with a low noise level to suppress small contrast variation.

This task-based approach, combined with the statistical decision theory and signal processing, has been further developed in recent years and is now one of the standards for assessing image quality in medical CT. The further developments of the reconstruction methods and the technical advances in computer capacity have led to many attempts to apply this approach to optimize the acquisition parameters [Vennart 1997].

In this thesis different models of task-based image quality assessment are investigated. Their performance in terms of the design and optimization of the acquisition trajectory is examined. This optimization focuses on identifying the best projections prior to the X-ray acquisition rather than improving the reconstruction itself [Gang et al. 2011]. Typical applications of this approach are CT configurations with a small number of projections or a shorter acquisition time. Both use cases are typical for an industrial inline CT application. With the identified projections, a CT scan can be performed on a customized trajectory. As a future goal, this optimized trajectory can be accessed using a robot-assisted CT system, where the X-ray source and the detector are mounted on two separate robot arms. Due to its flexibility, projections from almost any position are possible.

This thesis is divided into 7 chapters:

Chapter 1 introduces the motivation and the targeted scope of this work. It contains the synopsis of the following chapters as well.

Chapter 2 provides the theoretical background of cone-beam computed tomography (CBCT). It presents briefly the system matrix and the general forward projection model of a cone-beam setup and the associated Lambert-Beer's Law. The standard acquisition trajectories will be illustrated as well.

In **Chapter 3** we will contemplate with the mathematical framework of the reconstruction methods used in this work with focus on the Penalized-Likelihood (PL) estimation and the Filtered Backprojection (FBP). In the following, we introduce the Standard Deviation (SD) and the Root-Mean-Square-Error (RMSE). Both metrics are used to assess the quality of the reconstruction.

In section 1 of **chapter 4** we present standard image quality metrics and approaches for trajectory optimization. After the discussion of their limitations, we will introduce in section 2 the principle of task-based metrics. The presented general framework serves as a design and development basis for all the numerical model observers.

The detailed presentation of the different model observers is conducted in **chapter 5**. Here we will explain the mathematical background and the specific motivation for each model. This is the major part of the theoretical basics. Further, we will discuss their features and their limitations. The model observers are divided into two categories:

- The **Fourier-based Pre-Whitening and Non-Pre-Whitening observers**: Due to the high dimensionality of today's CT images, the inversion of the covariance matrix of an image is difficult to compute. In order to avoid the inversion, these model observers are presented in the Fourier domain instead of the spatial domain.
- The **Channelized Hotelling Observers** reduce this dimensionality of the covariance matrix through channelization. This technique decomposes an image into different spatial frequency channels. As a result, the inversion of the covariance matrix is easy to calculate.

Subsequently, the flowchart of the task-based trajectory optimization for 3D and 2D features is given in **chapter 6**. Here the application of the theoretical framework is demonstrated just in certain contexts (we will focus on optimization and detection with respect to one single feature), as the motivation of this work is on the more theoretical aspects, which can then be adapted to a specific application.

Finally, **Chapter 7 and 8** summarize the results of this thesis. Here, we will discuss the performance of the examined model observers regarding trajectory optimization and features detection. We will also highlight the areas of possible future investigations based on the experience gained during this work.

2 Fundamentals of Computed Tomography

This chapter describes the physical and mathematical details of an X-ray imaging system.

These are necessary for the implementation of the reconstruction methods and the task-based performance metrics that will be discussed later.

2.1 Introduction

The first applications of X-ray imaging were established for medical purposes. This has been extended to non-medical use because of its advantages in diversifying different materials with different densities. Today it is a widely used non-destructive testing method for industrial applications. It offers the unique opportunity to deliver a full 3D representation of a single component or a very complex assembly. This makes X-ray imaging an excellent tool for quality assurance and control in many technological areas such as materials science, metrology and manufacturing. Today, a very accurate inspection can be achieved as the new generation of X-ray imaging systems can examine an object with a very high resolution.

To scan an object, an X-ray source and a detector are required. The X-rays generated by an X-ray tube pass through the object, which absorbs photons depending on its geometry and material, and then hit the detector. The detector measures the remaining photons and converts this information into greyscale images [Buzug 2008].

Geometry of an X-ray System:

The geometry of the X-rays can be divided into three major categories: Parallel-beam, Fan beam and Cone-beam. However, the cone-beam geometry has become more popular due to the short scanning time. This is very advantageous because the heat generated in the x-ray tube, which limits the measurement time, can be better controlled [Buzug 2008]. For the CT measurements in this work we use the cone beam configuration. An illustration of this setup with the main parameters is given in Figure 2.1.

The distance between the X-ray source and the object (more precisely its rotation axis) is called SOD (Source-Object-Distance), while the Source-Detector-Distance is denoted as SDD. Each X-ray cone beam is characterized by its opening angle Ω . For every CT setup, the magnification M is given as:

$$M = \frac{SDD}{SOD} \quad (2.1)$$

This value is required to calculate the voxel size. If the voxels that define the volume of the object are isotropic, the voxel size can then be estimated as:

$$VoxelSize = \frac{PixelSize}{M} = \frac{SOD}{SDD} PixelSize \quad (2.2)$$

The PixelSize refers to the size of the pixels on the detector, which are also assumed to be isotropic.

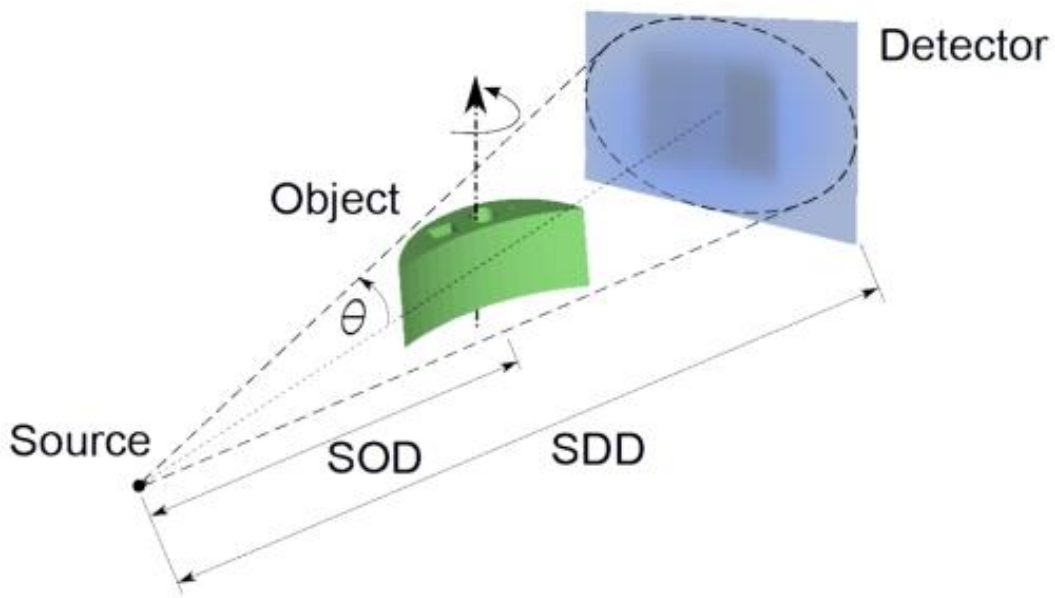


Figure 2.1: Geometry and notation for a cone beam CT setup with opening angle θ [Schrapp 2015]

CT devices:

A CT device that is equipped by such a cone-shaped X-ray and a flat-panel detector is categorized in the seventh generation. Figure 2.2 gives an overview of modern CT scanners used in the medical field (left side) and for industrial applications (right side). (A) is a C-arm scanner which is used in angiography. (B) is a conventional whole-body CT scanner. However, this variant has fan beam geometry and an arced detector with multiple-slices. (C) is a granite-based system. It allows to scan large objects and to achieve high magnification M . Since this system is open, it must be installed in a room with radiation protection and therefore can't be positioned next to a production line. In (D) we see the robot-assisted CT (RoboCT) of the vehicle manufacture BMW. In this configuration, the X-ray source and the detector are mounted on two separate robots that provide the ability to reach any inspection position around the vehicle [Buzug 2008] [Schoener 2012].

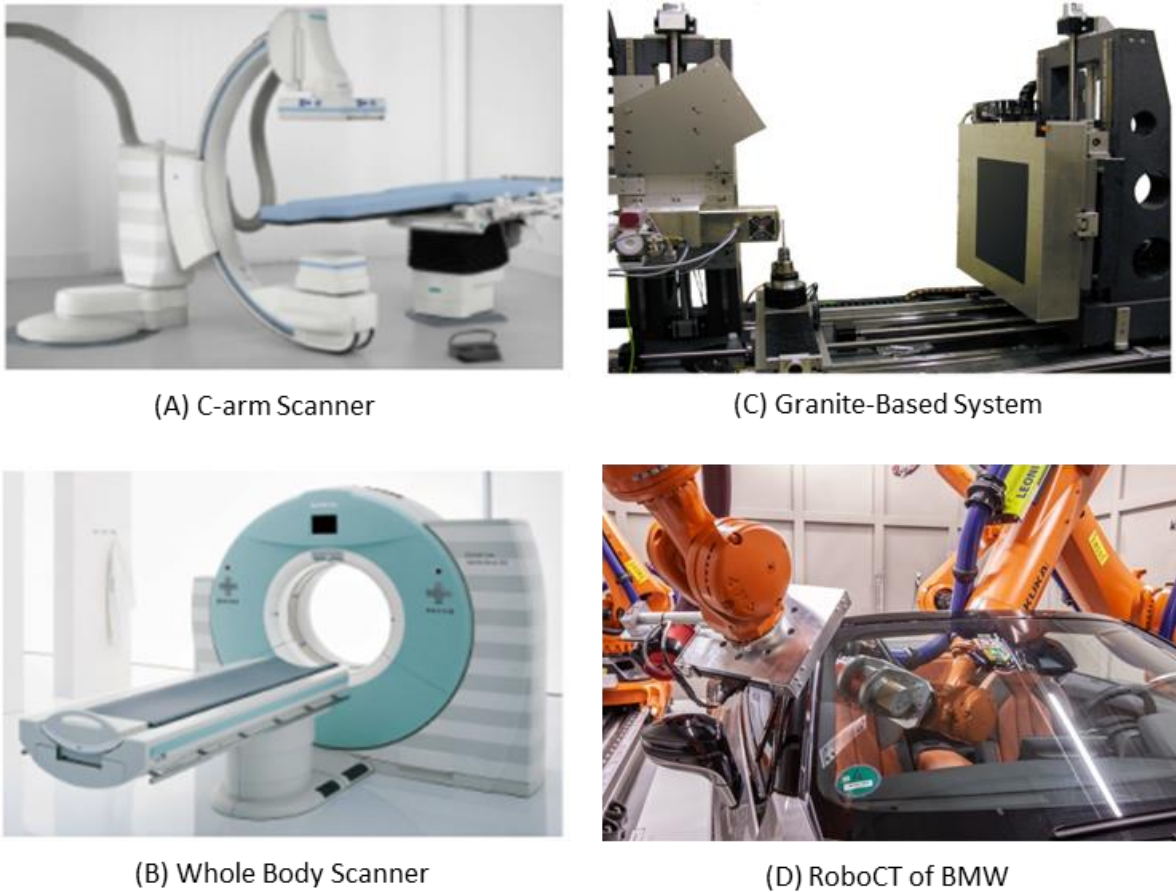


Figure 2.2: Overview of modern CT scanners used in the medical and industrial fields. The figures are reproduced from [Schoener 2012] [Fraunhofer EZRT 2019]

2.2 Standard Acquisition Trajectories:

In the following, some widely used standard trajectories in the industrial CT are presented. For each discrete position on the trajectory, a 2D projection is created. Once all required projections have been made, a 3D reconstruction of the object is performed. For this purpose, various reconstruction methods have been developed and refined over the years. Some of these algorithms are presented in the next chapter.

For a better illustration the trajectories are sketched in Figure 2.3. The positions of source and detector are highlighted. It does not matter if the detector-source moves against the object or vice versa. The acquired projections from both trajectories are identical.

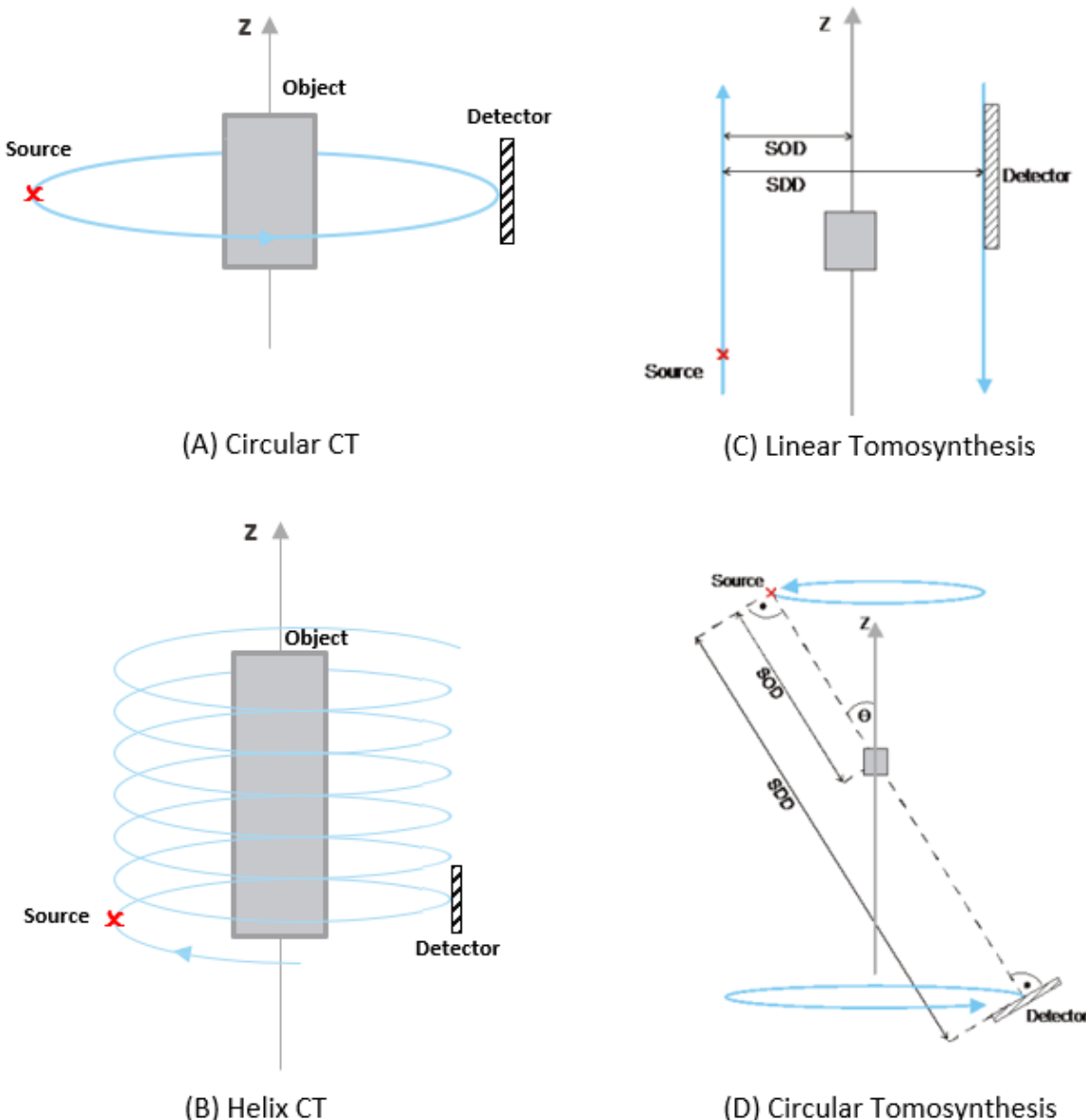


Figure 2.3: Overview of different acquisition geometries. Source, detector and trajectory are marked as red, black and blue. The figures are adapted from [Buzug 2008]

- **Circular orbit:**

In standard cone-beam CT, the projections are recorded with a 2D detector moving on a circular orbit around the object to be X-rayed. The source lies on the opposite side of the object and moves in the same direction as the detector (i.e. clockwise or counter-clockwise). The data is usually recorded over the full 360-degree of the circle. However, the circular orbit does not fulfill the Tuy-Smith sufficiency condition. This condition requires that every plane intersecting the object must intersect the source-detector trajectory at least once for an exact reconstruction. This is guaranteed just for the object plane that contains the acquisition orbit. The incompleteness of the data with this scan setup results in a high impact of the cone artifacts

during reconstruction. The contrast resolution is also reduced due to the insufficient data [Buzug 2008]. Figure 2.4 shows how the circular orbit can be extended to meet this condition.

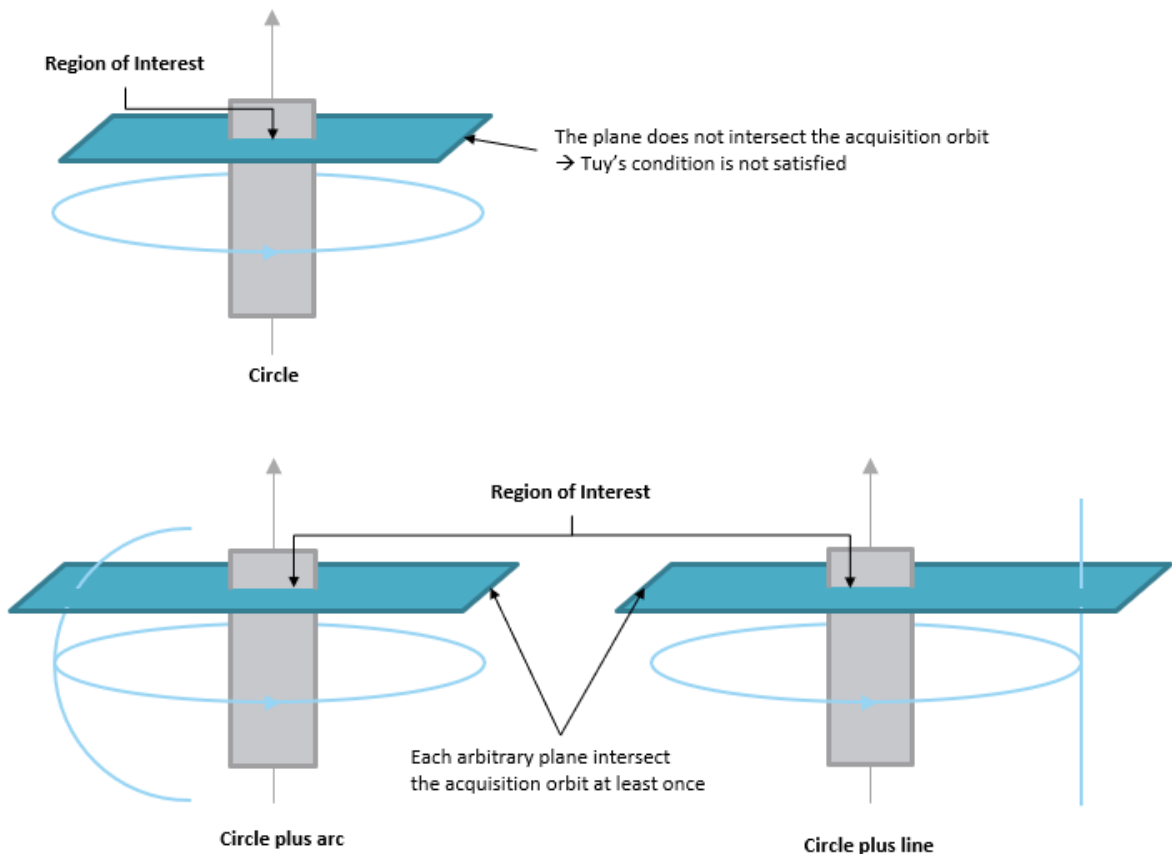


Figure 2.4: Extension of the simple circular orbit to fulfill the Tuy-Smith sufficiency condition

- **Helix orbit:**

The helical geometry can be used to scan long objects. It requires that either the object or the source and detector are moveable in the direction orthogonal to the circular trajectory.

The helical acquisition fulfills the Tuy-Smith condition and is therefore mathematically complete. It delivers a cone artifact free reconstruction. However, the iterative reconstruction of a volume-of-interest which is part of the entire volume is problematic. The reason for this is that each voxel of the volume has a different tomographic angle for each imaging location.

The latest is the angle between the X-ray passing through the voxel and the axis of rotation of the helix [Buzug 2008].

The classic helical trajectory with a small pitch requires long acquisition times. As illustrated in Figure 2.5 this can be replaced by the circles-plus-line trajectory to image the object in less time without affecting the reconstruction quality.

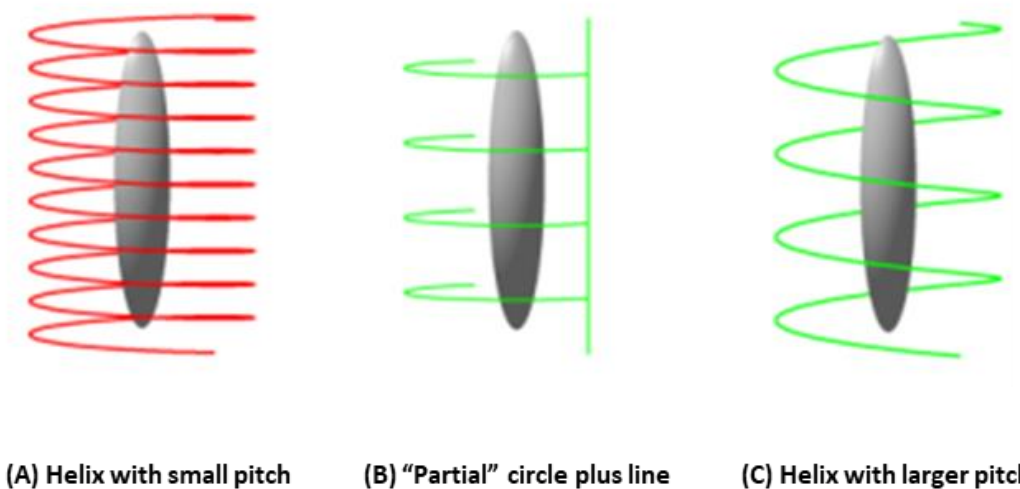


Figure 2.5: Typical acquisition geometries for long objects. The figures are reproduced from [Siemens 2016]

- **Linear and Circular Tomosynthesis:**

For large and flat objects whose dimensions exceed the dimensions of the imaging system, volume information can be obtained with the help of the linear or circular tomosynthesis. In the geometry of linear tomosynthesis, the source and detector move on linear trajectories parallel to a major axis and on opposite sides of the object. The object itself remains fixed. In the circular arrangement, they move on circular paths in planes that are parallel to an object plane. The detector can be orthogonal to the main X-ray of the source or parallel to the plane containing the detector trajectory [Buzug 2008].

As it was discussed previously, the limited imaging angle range of tomosynthesis results in incomplete projection data. Therefore, the Tuy-Smith condition is not fulfilled, and the reconstruction using IR methods leads to the typical reconstruction artifacts that limit the axial resolution of the reconstructed volume [Ebensperger 2014].

2.3 System Matrix

For the reconstruction, the object volume must be discretized in a finite number of voxels.

Each voxel i is then presented with a constant value parameter, called attenuation coefficient or density μ_i . These parameters are unknown and will be calculated using a reconstruction algorithm. For the sake of simplicity, we consider the X-ray examination of a 2D slice of a 3D object. The formulas shown here are thus legal for the 3D case.

Within a cone-beam CT the X-rays are modelled as elongated triangles. The ratio between the area illuminated by the j -th X-ray within the i -th cell and the entire area of the i -th cell is defined as the weighting factor A_{ji} . In other words, each element A_{ji} reflects the contribution of a specific cell to a specific pixel measurement. The term b_j , which specifies the projection data obtained at the detector, is notated as the measurement gain along the j -th X-ray. The relationship between the unknown densities μ_i and the measured values b_j is then given for each detector pixel as [Buzug 2008]:

$$b_j = \sum_{i=1}^n A_{ji} \mu_i \quad \text{with } j = 1, \dots, m \quad (2.3)$$

where, n is the number of cells (voxels in 3D) and m is the number of pixels of the detector.

Figure 2.6 shows this concept schematically for a cone-beam CT.

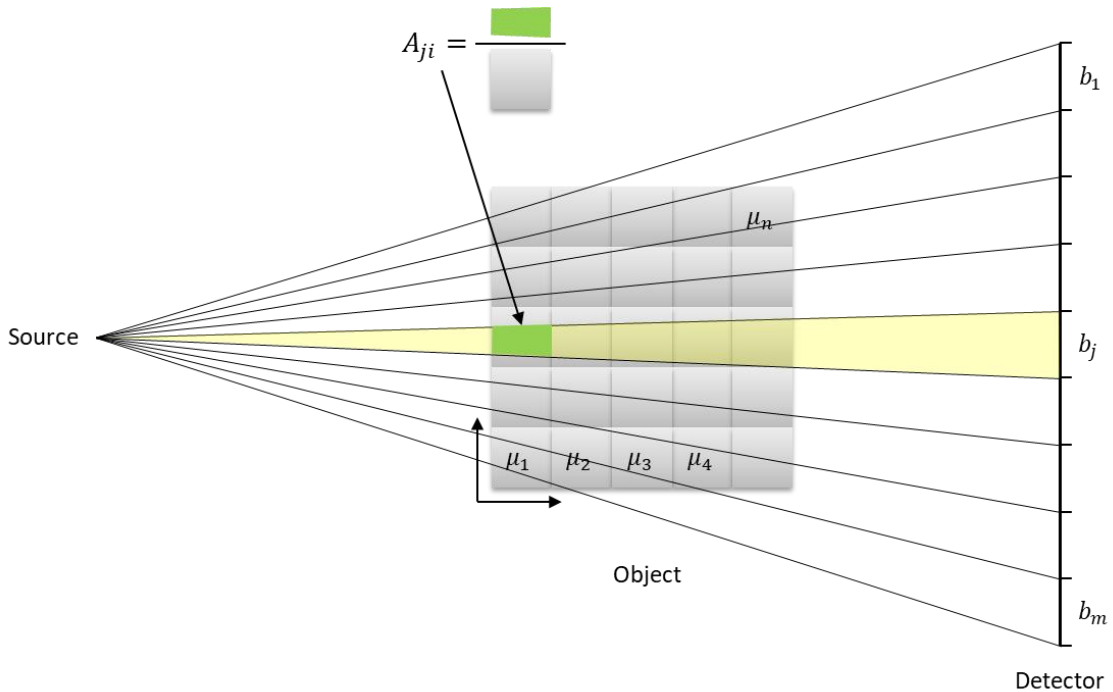


Figure 2.6: Visualization of the weighting factors A_{ji} in a 2D algebraic forward projection model for cone-beam configuration

Equation (2.3) can be expanded to express b_j as a function of all cells. In this way we obtain a system of linear equations for each projection. In general form we have:

$$\begin{aligned} A_{11}\mu_1 + A_{12}\mu_2 + \cdots + A_{1n}\mu_n &= b_1 \\ A_{21}\mu_1 + A_{22}\mu_2 + \cdots + A_{2n}\mu_n &= b_2 \\ &\vdots \\ A_{m1}\mu_1 + A_{m2}\mu_2 + \cdots + A_{mn}\mu_n &= b_m \end{aligned} \quad (2.4)$$

The system of equations for each projection can also be rewritten in matrix form as:

$$\begin{bmatrix} A_{11} & \cdots & A_{1n} \\ \vdots & \ddots & \vdots \\ A_{m1} & \cdots & A_{mn} \end{bmatrix} \cdot \begin{pmatrix} \mu_1 \\ \vdots \\ \mu_n \end{pmatrix} = \begin{pmatrix} b_1 \\ \vdots \\ b_m \end{pmatrix} \quad \text{or} \quad [A\mu = b]_{Proj\ k} \quad (2.5)$$

where, b (size m) and μ (size n) are column vectors for the measurements and the attenuation values, the geometry matrix A (size $m*n$) is called system or design matrix, and k refers to the k -th projection.

The equation (2.5) can be expanded to include all measured projections and it becomes:

$$A\mu = b \quad (2.6)$$

The composition of the system matrix A during acquisition is shown graphically step by step in the following Figure 2.7.

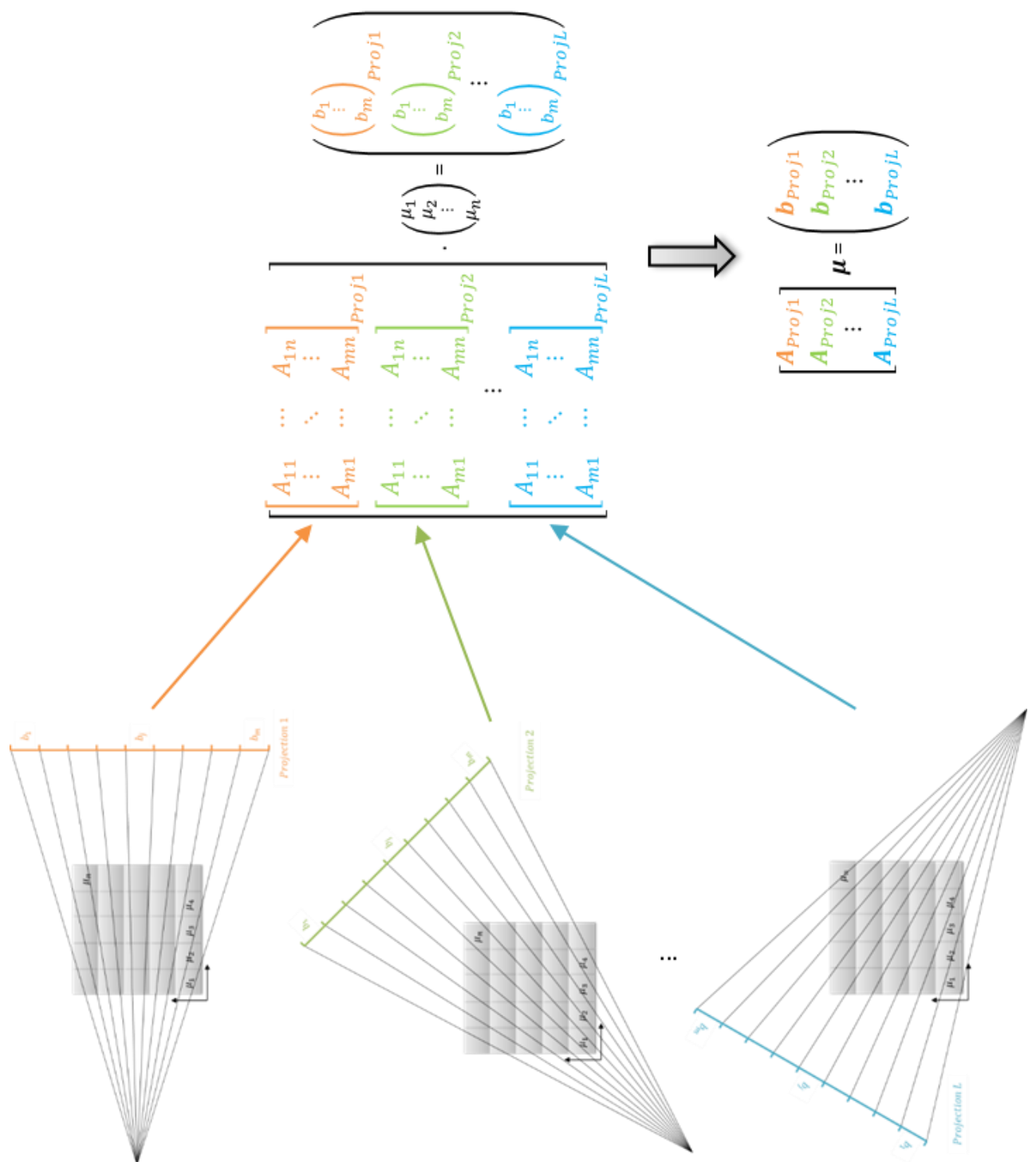


Figure 2.7: Schematic overview of the relation between the system matrix, the attenuation values of the object and the measurements for multiple projections

2.4 Lambert-Beer's Law

When an X-ray passes through an object of thickness s with a constant attenuation value μ , it undergoes attenuation due to various physical mechanisms, such as photoelectric absorption or inelastic Compton scattering. The intensity I after attenuation of a monochromatic X-ray beam with initial intensity I_0 is determined by the Lambert-Beer's Law [Buzug 2008]:

$$I_j = I_0 e^{-\mu s} \quad (2.7)$$

The attenuation of the X-ray, running through a sequence of multiple discontinuous elements with different attenuation coefficients μ_i and different thickness s_i , can be described as:

$$I_j = I_0 e^{-\sum \mu_i s_i} \approx I_0 e^{-\int \mu(s) ds} \quad (2.8)$$

The attenuated intensity I_j after passing through the object is given by the pixel values on the detector. The initial intensity I_0 can be measured by performing a first scan without the object. The thickness s_i , which represents the length travelled by the X-ray beam through the i -th element, can be approximated as the element size (corresponding to the voxel size in 3D). Knowing I_j , I_0 and s_i , the relationship between the unknown attenuation coefficients μ_i , can be expressed as follows:

$$b_j = \int \mu(s) ds \approx \sum \mu_i s_i = -\ln\left(\frac{I_j}{I_0}\right) \quad (2.9)$$

The line integral b_j generally describes the attenuation of the j -th X-ray through the object and corresponds to the definition in equation (2.3).

By substituting (2.6) and (2.9) into (2.7), we obtain the simplified general forward model for the measurement I :

$$I(\mu) = \mathbf{D}\{I_0\} \cdot e^{-A\mu} \quad (2.10)$$

Where, the diagonal matrix $\mathbf{D}\{I_0\}$ includes the measurement-dependent gains. Assuming that each detector pixel in the free jet (i.e., without an object in the X-ray path) is the same, all the diagonal entities have the same value I_0 . However, this is an idealization which is not typically the case.

3 Reconstruction Methods

Numerous previous publications have described the tomographic system models and the associated iterative reconstruction methods. This chapter presents the important information that will be needed for this work.

The system matrix, A , and the measurements, b , are known before reconstruction. Knowing the Source-Object (SOD) and Source-Detector (SDD) distances, number & size of voxels (volume of the object) and number & size of pixels (size of the detector), the system matrix can be calculated. To obtain the unknown attenuation coefficients, μ , equation (2.6) must be solved.

However, the explicit calculation of the inverse matrix of A is very time-consuming. And since A is very large, storing the matrix requires a lot of memory [Buzug 2008]. Memory requirement is explained using an example from this work:

The volume of an object is discretized using (512 x 512 x 512) voxels. The flat detector has 512 pixels in each direction. An equiangular acquisition on a rotation orbit with an angle step of 1° provides 360 projections. The size of the system matrix for each projection is then:

$$[512 * 512] * [512 * 512 * 512]$$

Each coefficient in the matrix is defined as a float (= 4 bytes). The storage requirement for this system matrix is then 128 Terabytes. An inversion of the entire system matrix (128 Terabytes * 360 projections) is very demanding even for modern computers with powerful hardware and software. Furthermore, since an X-ray illuminates just a small number of voxels in 3D (cells in 2D), a reconstruction approach without explicit formation of the system matrix, A , can be applied to solve the equation (2.6).

3.1 Iterative Reconstruction Technique

The principle of IR algorithms is to reconstruct a tomographic volume from measured projections by iterative estimation. At the beginning, a first estimate is arbitrarily created. This could be a uniform object, where all voxels are equal zero or one. As next, simulated projections of this first estimate are created. Then, these projections are compared with the measured projections. The result of the comparison is then used to change the current estimate based on a specific applied method. By that, an adjusted estimate is created, and a new iteration starts. This is repeated until the measured and the adjusted projections agree according to a condition predefined by the algorithm [Buzug 2008]. A simplified schematic of the IR algorithms is given in Figure 3.1.

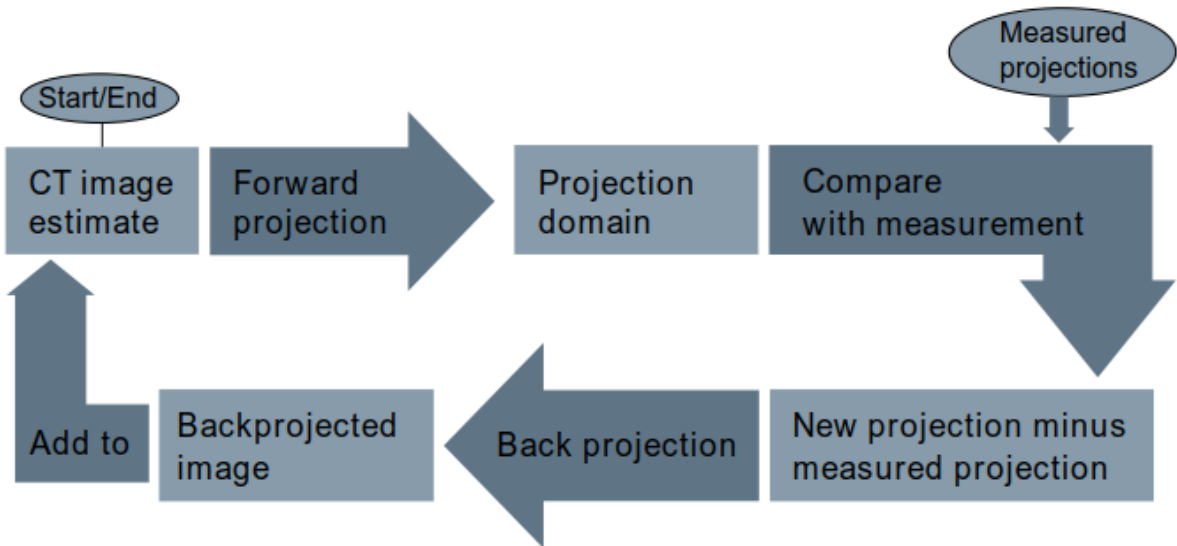


Figure 3.1: The relevant steps of iterative reconstruction algorithms [Schrapp 2015]

IR methods support the acquisition with arbitrary geometry that satisfy the Tuy-Smith sufficiency condition and recent advances in computational power have made IR algorithms a valuable option for industrial CT imaging [Schrapp 2015].

3.1.1 Algebraic Reconstruction Technique

First introduced by Gordon et al. in 1970, the algebraic reconstruction approach solves the equation (2.6) iteratively for each voxel $i = 1, \dots, n$ and X-ray $j = 1, \dots, m$ [Gordon et al. 1970].

$$\mu_i^{n+1} = \mu_i^n + \lambda_n \frac{A_{ji}(b_j - \sum_{i=1}^n \widehat{A_{ji}\mu_i^n})}{(\sum_{i=1}^n A_{ji})^2} \quad (3.1)$$

$\overbrace{\hspace{10em}}$ *Weighting*
 $\overbrace{\hspace{10em}}$ *Backprojection*
 $\overbrace{\hspace{10em}}$ *Measured minus new projections*
 $\overbrace{\hspace{10em}}$ *Forwardprojection*

The forward projection of the current estimate given by $\sum_{i=1}^n A_{ji}\mu_i^n$ is compared with the logarithmized measured values $b_j = -\ln(\frac{I_j}{I_0})$. The difference is then back-projected into the volume domain, weighted with a positive defined real number λ and finally added to the current estimation of the object. The term λ is called the relaxation parameter and serves to accelerate the convergence of the iterations. This is necessary because of the expensive calculation of each iteration. It also minimizes the impact of data inconsistency and the order of the

processed X-rays. It has also been proven that for each iteration there is an optimal value of λ which maximize the rate of convergence [Buzug 2008].

Compared to other IR approaches, ART is relatively fast and provides respectable reconstruction quality. However, when dealing with “very” noisy data, this method is ineffective. To overcome this restriction and improve the quality of the reconstructed volume, the projections can be examined simultaneously. In each iteration there is only one forward- and back-projection step. This method is called the Simultaneous Iterative Reconstruction Technique (SIRT) [Andersen et al. 1984].

3.1.2 Penalized-Likelihood Reconstruction

In this work, we focus on the Penalized-Likelihood reconstruction which belongs to the category of iterative reconstruction methods. It maximizes an objective function $\Phi(\mu; y)$, which represents for this approach the difference between the log-likelihood function L and a penalty term. The general form for the PL reconstruction ($\hat{\mu}$) from projections (y) acquired from arbitrary trajectory is defined as:

$$\hat{\mu} = \text{argmax}[\Phi(\mu; y)] = \text{argmax}[logL(\mu; y) - \beta R(\mu)] \quad (3.2)$$

Where, the penalty function $R(\mu)$ is weighted by a regularization strength parameter β . This penalty term allows controlling the balance between resolution and noise.

This formulation offers the possibility to investigate different noise models, which are related to different likelihood functions. In addition, we could examine several types of regularization strategies. Selecting the commonly used Poisson model for the variations of the independent measurements yields to the following log-likelihood function [Stayman et al. 2011]:

$$L(\mu; y) = p(y|\mu) = \prod_{i=1}^N p(y_i|\mu) = \prod_{i=1}^N \underbrace{e^{-\bar{y}_i(\mu)} \frac{(\bar{y}_i(\mu))^{y_i}}{y_i!}}_{\text{Poisson distribution}} \quad (3.3)$$

$$\log L(\mu; y) \cong \sum_{i=1}^N y_i \log[I_0 e^{(-A\mu)}]_i - [I_0 e^{(-A\mu)}]_i \quad (3.4)$$

where, N is the number of the noisy measurements.

For the regularization, we choose a quadratic penalty which can be expressed mathematically as follows:

$$R(\mu) = \frac{1}{2} \mu^T R \mu \quad (3.5)$$

where, \mathbf{R} is a $n_{Voxels} \times n_{Voxels}$ constant matrix that is defined as the Hessian of $R(\mu)$. The latter illustrates how voxels are combined and penalized and can be written as:

$$R(\mu) = \frac{1}{2} \sum_j \sum_k w_{j,k} (\mu_j - \mu_k)^2 \quad (3.6)$$

This special type of quadratic penalty penalizes the voxel differences in a first order neighborhood around a voxel location j . The weighting function $w_{j,k}$ is equal to the inverse of the distance between the j -th voxel and the nearest k -th neighbor voxel (4 or 8 in 2D and 6 or 26 in 3D reconstruction). Otherwise it is 0. Figure 3.2 illustrates the penalized pixels in a slice reconstruction with two different ways [Gang et al. 2017].

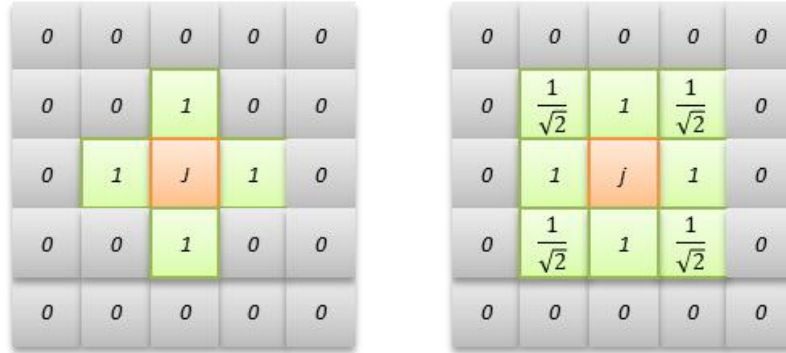


Figure 3.2: Illustration of the penalized pixels in a 2D slice reconstruction

The PL reconstruction provides better results when dealing with incomplete data, e.g. acquisition of projections with limited angle. However, it is mostly difficult to analyze compared with analytic methods such as the Filtered-Backprojection [Gang 2014].

3.2 Filtered Backprojection

In this section we want to introduce the widely used Fourier-transform based filtered back-projection (FBP), which belongs to the analytical reconstruction algorithms. Assuming the completeness of the projection data, the reconstruction with FBP is fast and precise and requires less computational effort than IR methods. However, it can lead to certain strong artifacts like the cupping artifact, which is induced by beam-hardening [Buzug 2008]. It is often used for standard circular trajectories. But, it can also support other acquisition geometries in a modified form [Zikuan et al. 2006]. In this work we will use this method for the optimization as well as the final volume reconstruction.

- **Radon transform:**

For sake of simplicity, we consider the parallel-beam geometry to image a single 2D slice of an object. Nevertheless, the extension to cone-beam geometry to reconstruct a 3D object is

straightforward and will be discussed at the end of this section. For a monochromatic X-ray source and an object with unknown attenuation coefficient μ , the Lambert-Beer's law (see section 2.4) for the measured intensity I on the detector position ξ along one parallel X-ray L , is written as:

$$I(\xi) = I_0 e^{-\int_L \mu(x,y)dl} \quad (3.7)$$

The representation of the attenuation coefficient $\mu(x, y)$ in the fixed coordinate system (x, y) will be replaced by the more general form $f(x, y)$, which has also the same distribution as $\mu(\xi, \eta)$ in the rotating coordinate system (ξ, η) . In other words, $f(x, y) \equiv \mu(\xi, \eta)$. For a fixed projection angle γ and at a position ξ on the detector, the projection integral is given as [Buzug 2008]:

$$p_\gamma(\xi) = \ln \left(\frac{I_0}{I(\xi)} \right) = \int_L \mu(\xi, \eta) d\eta \quad (3.8)$$

The path L is a straight line and can be parametrized by:

$$\xi = x \cos(\gamma) + y \sin(\gamma), \quad \eta = -x \sin(\gamma) + y \cos(\gamma) \quad (3.9)$$

Changing from the rotating to the fixed coordinate system leads to the two-dimensional Radon transform of the object:

$$p_\gamma(\xi) = \int_{-\infty}^{\infty} \int_{-\infty}^{\infty} f(x, y) \delta(x \cos(\gamma) + y \sin(\gamma) - \xi) dx dy \quad (3.10)$$

- **FBP for Parallel-Beam geometry:**

The approach of the filtered back-projection is visualized in the following figure.

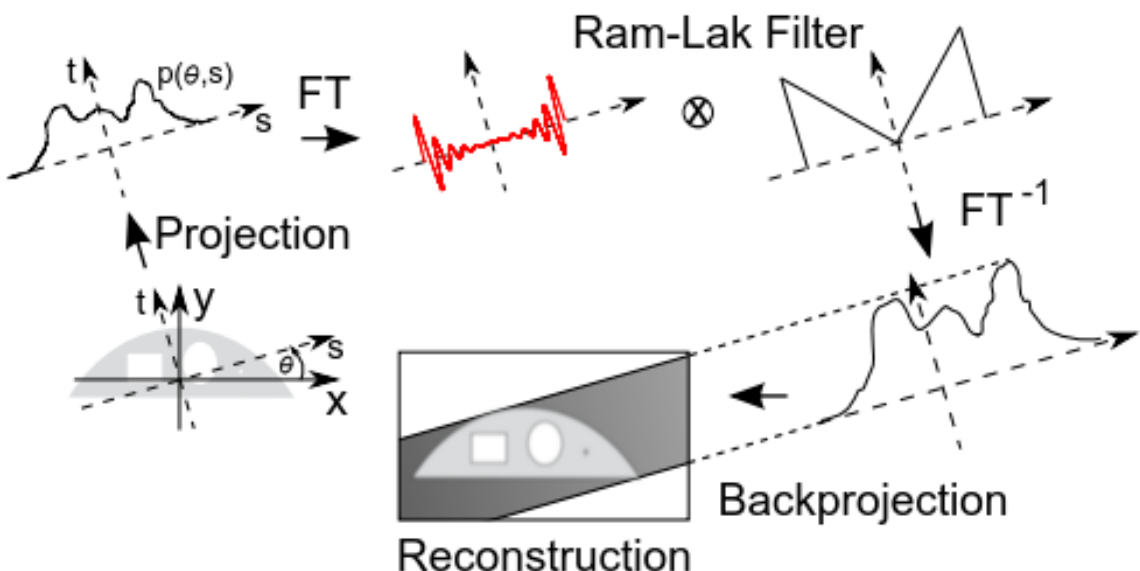


Figure 3.3: Workflow of the filtered back-projection (FBP) with a ramp filter [Schrapp 2015]

The main four steps of the filtered back-projection can be summarized as follows [Buzug 2008] [Schrapp 2015]:

1. For each projection angle γ , the Fourier transform of the measured projection profiles is calculated:

$$P_y(q) = \mathcal{F}\{p_\gamma(\xi)\} = \int_{-\infty}^{\infty} p_\gamma(\xi) e^{-2\pi i q \xi} d\xi \quad (3.11)$$

2. High-pass filtering of $P_y(q)$ by multiplying it with the filter function $G(q)$:

$$P_\gamma(q) G(q) \quad (3.12)$$

The difference between filtered and unfiltered back-projection is demonstrated in Figure 3.4 (A) using the simple example of a square with only one attenuation coefficient.

3. The inverse Fourier transform of the high-pass filtered $P_y(q)$ lead to the so-called filtered projection $h_\gamma(\xi)$:

$$h_\gamma(\xi) = \mathcal{F}^{-1}\{P_\gamma(q) G(q)\} = \int_{-\infty}^{\infty} P_\gamma(q) G(q) e^{2\pi i q \xi} dq \quad (3.13)$$

4. Each filtered projection $h_\gamma(\xi)$ is back-projected along the line ξ :

$$f(x, y) = \int_0^\pi h_\gamma(\xi) d\gamma \quad (3.14)$$

This step is very important for this work, as it equals the multiplication with the inverse of the system matrix A .

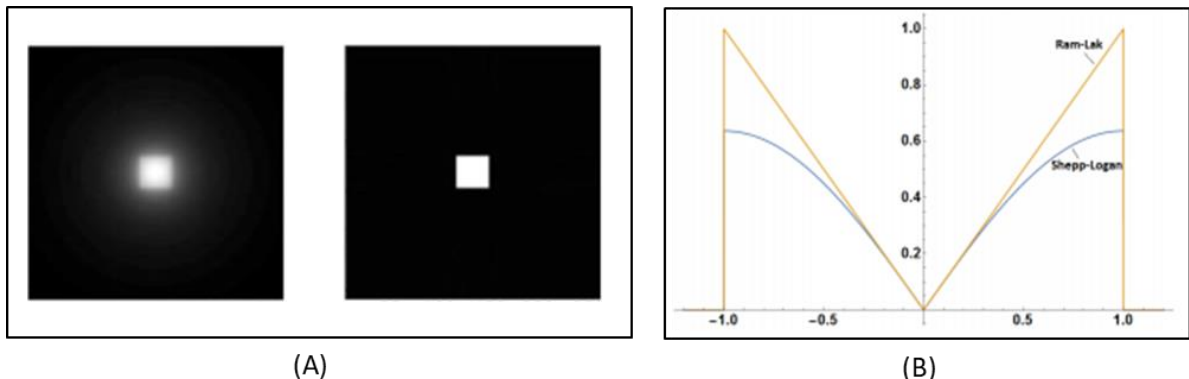


Figure 3.4: (A) Illustration of the effect of the high-pass filtering. Left: Unfiltered back-projection. Right: Filtered Back-projection with Ram-Lak filter ($G(q) = |q|$) [Buzug 2008]. (B) Filter kernels of the Ram-Lak filter and the Shepp-Logan filter [Lee et al. 2011]

Due to the Fourier transform, low frequencies are weighted more heavily for a simple summation than high frequencies. To avoid this problem, a high-pass filter can be used as a simple solution. For complete and continuous data, the Ram-Lak filter with $G(q) = |q|$ is

appropriate. However, as high frequencies are over-weighted, signal noise in this range can be amplified. To compensate this, the Shepp-Logan filter kernel can be used. This limits the frequency band with a rect-function and lowers the high-pass weighting at high frequencies with a sinc function. Its function is then given by $G(q) = |q| \text{rect}(q) \text{sinc}(\pi q)$ [Lee et al. 2011]. Using the convolution theorem, the filtering can be applied directly to the non-Fourier transformed data. The multiplication in the frequency domain becomes a convolution in the spatial domain [Buzug 2008].

- **FBP for Cone-Beam geometry:**

For cone beam geometry, two major modifications must be taken in the previously formulated filtered back-projection [Lee et al. 2011]:

1. According to the Inverse-Square Law, the intensity of a divergent X-ray decreases proportional to the square of the source-voxel-distance (SVD). This can be considered via a quadratic voxel-dependent weighting in the back-projection step.
2. The filter kernel has also to be changed depending on the distance between the detector midpoint and the pixel that represents the projection of the considered voxel on the detector. The distances in the row and column direction are denoted respectively by a and b .

Using the filter kernel $g(a)$ in the spatial domain and the convolution operator \otimes , the distribution of the attenuation values can then be written as:

$$f(x, y, z) = \frac{1}{2} \int_0^{2\pi} \underbrace{\frac{SOD^2}{SVD^2}}_{\substack{\text{Reconstruction} \\ \text{weighting}}} \underbrace{\left(\left[p_\gamma(a, b) \underbrace{\frac{SOD}{\sqrt{SOD^2 + a^2 + b^2}}}_{\substack{\text{Filter} \\ \text{weighting}}} \right] \otimes g(a) \right)}_{\substack{\text{Filtered projection} \\ \text{Back-projection}}} d\gamma \quad (3.15)$$

3.3 Quality metrics for the evaluation of reconstructions

Quality metrics for image evaluation are often not uniform but used on a case-by-case basis. In this work, reference data such as the 3D geometry of the part are available and will be used to evaluate the reconstructed volume. Most used approaches are the Mean-Square Error and the Peak Signal-to-Noise Ratio. These are simple and easy to compute, and its physical interpretation is clear and straightforward. If no reference data set is available, metrics that evaluate the noise and the edge accuracy can be used. In particular, the Shannon entropy and the line spread function are convenient in the context of optimization. However, a mathematically interesting objective metric is the Standard Deviation. It quantifies the variation of the attenuation coefficients, which can be understood as noise in the raw measurements [Dremel 2017].

- **Root-Mean-Square Error (RMSE)**

The simplest and most commonly used metric is the root mean square error (RMSE), which is calculated by summing all the squared differences of the attenuation coefficients of the reference and the reconstructed volume voxels. Due to the quadratic weighting, large deviations are considered more strongly [Suresh et al. 2014].

$$\sigma_{RMSE} = \sqrt{\frac{1}{n} \sum_{i=1}^n (\mu_i - \mu_{i,ref})^2} = \sqrt{\sigma_{MSE}} \quad (3.16)$$

where, n is the number of voxels and σ_{MSE} is the mean square error.

- **Standard Deviation (SD)**

Although very similar to the RMSE, a difference measure may be used not only between the reconstructed and the reference volume but also only within the reconstruction. It is defined as the standard deviation and can be written as [Fischer et al. 2016]:

$$\sigma_{SD} = \sqrt{\frac{1}{n-1} \sum_{i=1}^n (\mu_i - \bar{\mu})^2} \quad \text{with: } \bar{\mu} = \frac{1}{n} \sum_{i=1}^n \mu_i \quad (3.17)$$

When this parameter is applied to a volume region of known constant attenuation coefficients, then the standard deviation gives a measure of the noise.

- **Peak Signal to noise ratio (PSNR)**

PSNR measures the peak error between two images in decibels and can be physically understood as the ratio between the signal and noise. Mathematically, it is defined as the logarithm of the inverse of the root-mean-square error. This means that a lower value of RMSE yields to smaller error and thus PSNR has a higher value. It is given as [Suresh et al. 2014]:

$$\sigma_{PSNR} = 20 \log\left(\frac{R}{\sigma_{RMSE}}\right) \quad (3.18)$$

Where, R is the largest possible value in the reconstruction. For CT it is usually the attenuation coefficient of the highest density material.

4 Image Quality Assessment Metrics and Approaches

As described in the introduction, not all projections have the same value for the reconstruction. In order to successfully evaluate the image quality depending on selected projections, some approaches are presented below. The first subsection presents the traditional assessment metrics and methods. Then their limits are illustrated. The task-based image quality assessment, which is the core approach for selecting projections in this work, is described in the second subsection.

4.1 Traditional Metrics and Approaches

To evaluate the performance of a CT imaging system, a set of standard and generally accepted metrics such as the contrast-to-noise ratio are available.

Contrast-to-Noise Ratio (CNR):

CNR is a very common measure of image quality, which is directly related to the physical properties (mainly signal and noise) of the imaging systems. It rates the contrast degradation due to the noise in the image. In the spatial domain the CNR is defined as [Desai et al. 2010]:

$$CNR = \frac{\mu_{object} - \mu_{background}}{\sigma_{background}} \quad (4.1)$$

where, μ_{object} and $\mu_{background}$ are each the signal intensities of the object and the background. $\sigma_{background}$ is the noise in background and is given as the standard deviation.

However, information such as object size and shape as well as the pixel size of the image are not taken into account. This does not make CNR an optimal metric of image quality [Tseng 2015].

Several approaches have been developed to optimize the trajectory of the image acquisition. Below are some of them listed briefly.

Entropy-Based Projection Selection:

For a circular orbit, Placidi et al. (1995) have developed an adaptive acquisition method to reduce the number of projections necessary for the reconstruction.

The algorithm starts with four initial projections at 0, 45, 90 and 135 degree. Then the entropy of each of these projections is calculated. The entropy is defined as an objective function that quantifies the information content of each projection. Afterwards, the next projection between

the two projections with the highest entropy difference is added. The last two steps are then repeated until the number of the required projections or a predefined entropy difference is reached [Placidi et al. 1995]. An example to illustrate this approach is given below:

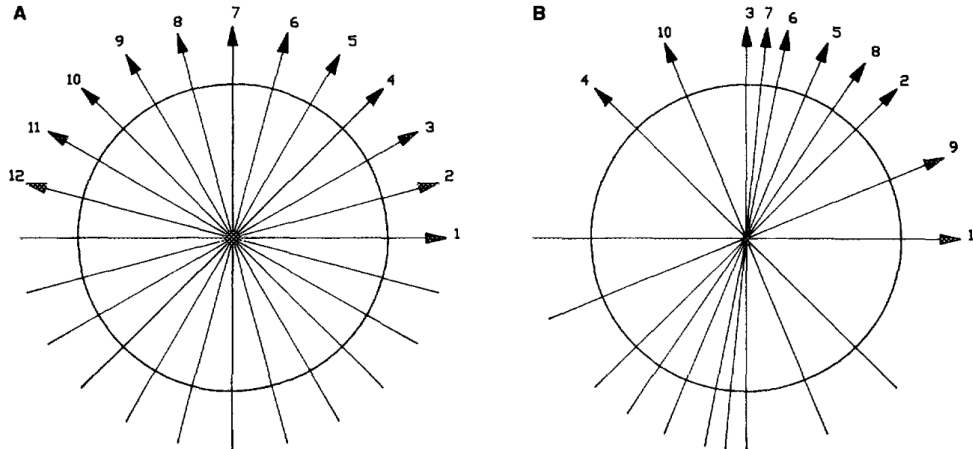


Figure 4.1: Example of projections selection for equiangular (A) and entropy-based acquisition (B) [Placidi et al. 1995]

Especially for smooth objects or objects with internal symmetries, a reconstruction with up to 30 % fewer projections without loss of information can be performed. Another advantage of this approach is that the evaluation occurs during acquisition, which requires less memory. However, this method doesn't incorporate prior knowledge of the object [Placidi et al. 1995].

Numerical Condition of System Matrix:

Vogel et al. (2013) proposed an optimization algorithm for freehand SPECT (Single Photon Emission Computed Tomography) based on the numerical condition of the system matrix. The system matrix A detailed in section 2.3 is created dynamically during real-time acquisition. Its numerical condition is chosen as a cost function, which determines the next best position of the detector [Vogel et al. 2013].

In detail, the system matrix is decomposed using the pivoted QR decomposition. And we get: $A = Q R P^T$. Then using the diagonal entities of the upper triangular matrix R , an energy function is defined as: $\eta(A) = \sum_i |R_{ii}|$. To determine the next best position, the energy value is calculated for each possible next position as: $\eta\left(\begin{matrix} A \\ P_{j+1} \end{matrix}\right)$. The projection with the highest energy value is added.

However, the optimization performance for random trajectories decreases as the size of the system matrix increases and the algorithm can no longer compute all possible positions [Vogel et al. 2013]

Concept of Information Gain:

Batenburg et al. (2012) have presented an algorithm for the dynamic selection of the next best projections. A new projection is added to a set of preselected projections, if the amount of information gained by acquiring this projection is maximized. This approach does not require prior information about the object.

However, due to the high complexity of the proposed algorithm, the optimization for 3D volumes with large dataset can be computationally very expensive [Batenburg et al. 2012].

Cover Most Relevant Edges:

As shown in Figure 4.2, the reconstruction of an edge requires X-rays that are tangent to this edge. Based on this, and using good prior knowledge of the object, Zheng and Mueller (2011) proposed an optimization framework that identifies a minimal set of projections covering the most relevant sharp discontinuities (edges).

First, the edges of the volume are detected using an edge detection algorithm and then converted to points via Hough transform. After recognizing the most salient points, a set-covering algorithm finds the set of projections that contain them.

Although this method uses prior object information, artifacts are not considered. This can lead to wrong results [Zheng et al. 2011].

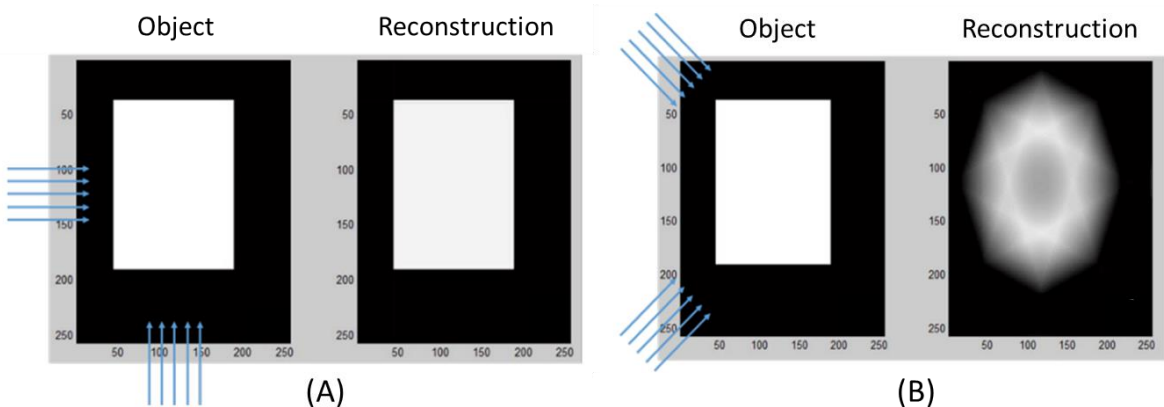


Figure 4.2: Reconstruction of a square with projections covering the X-rays tangent to the edges (A) and projections shifted by 45° [Fischer 2014]

4.2 Task-Based Quality Assessment

Previous works in the medical field have shown that image quality assessment is best evaluated when defining the clinically interesting task. Stayman et al. (2013) have proven that a task-based metric is apt to optimize the acquisition orbit. They developed a general optimization framework, which will be introduced in chapter 6. In this section we will explain the theory of task-based assessment and what limitations and analytical advantages this approach has.

Detection Task:

An industrially important and in our case relevant task is the detection task. It determines which of two possible categories the acquired CT image belongs to (e.g., a feature either exists or does not exist). To make this decision, a likelihood-ratio decision function is introduced [Vennart 1997]:

$$L = \frac{p(\mu|H_1)}{p(\mu|H_2)} \quad (4.2)$$

Where, μ is the true or approximated data set representing the object being x-rayed; and $p(\mu|H_k)$ corresponds to the conditional probability distributions of the data given hypothesis H_k . So, for the detection task the observer must decide which of the following hypotheses is more compatible with the data:

$$\begin{aligned} H_1 : \mu &= \mu_b && (\textit{feature absent}) \\ H_2 : \mu &= \mu_b + \mu_f && (\textit{feature present}) \end{aligned} \quad (4.3)$$

Where, μ_f refers to the feature to be detected and μ_b is the object background.

A comparison of the decision function L with a criterion or threshold L_c determines which hypothesis is true. There are several approaches to determine L_c . It can also be set directly by the observer. Finally, to measure how well the observer can detect the feature, a figure of merit is needed.

Figure of Merit:

We consider the probability distributions of the likelihood-ratio decision function L for both hypotheses. A very simple example is shown in Figure 4.3 [Vennart 1997].

To quantify the detection performance of an observer, a figure of merit like the Signal-to-Noise Ratio (SNR) can be used. It quantifies the overlap between the probability distributions and indicates how well the observer distinguishes between data of both hypotheses.

In other words, SNR is mathematically defined as:

$$SNR^2 = \frac{\text{Signal}}{\text{Noise}} = \frac{[\langle L \rangle_2 - \langle L \rangle_1]^2}{\frac{1}{2} \cdot [\sigma_1^2 + \sigma_2^2]} \quad (4.4)$$

Where, the mean $\langle L \rangle_k$ and variance σ_k^2 are calculated for the decision variable L under each hypothesis. SNR can be replaced by the detectability index d' , when the decision function L is Gaussian-distributed under both hypotheses. This means L must be linear in the data, which is true for Gaussian-distributed noise.

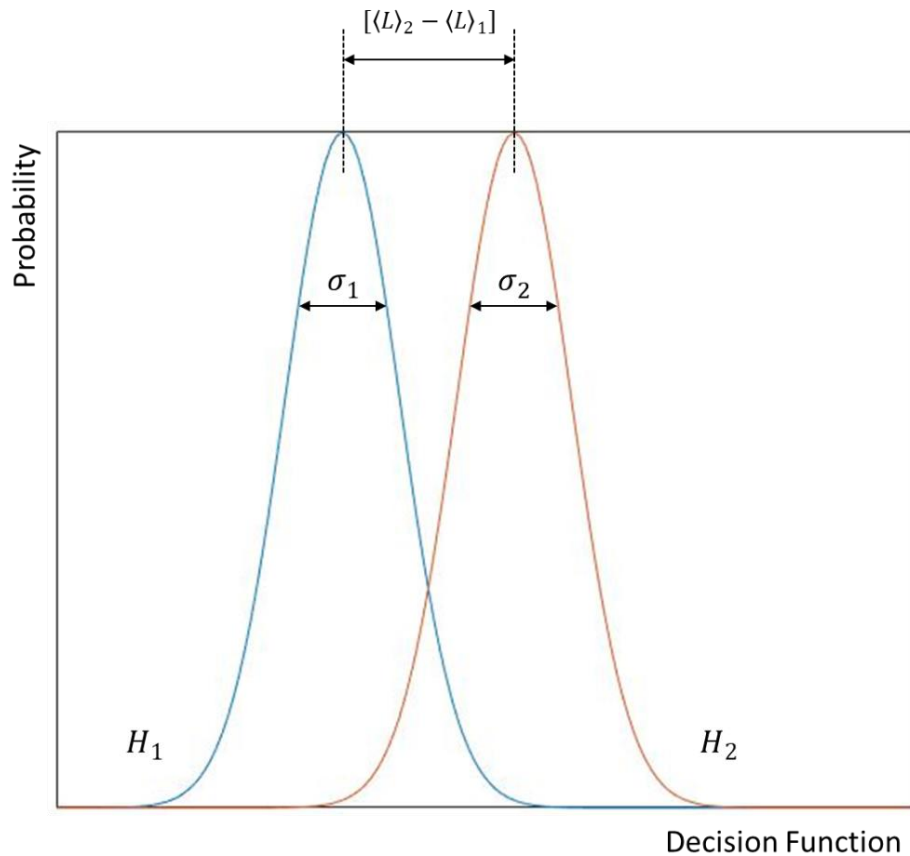


Figure 4.3: Probability distribution of the likelihood-ratio decision function for the hypothesis H_1 (left) and H_2 (right)

Figure 4.4 shows how the detectability and thus the observer performance vary for different cases. A strong signal increases the distance between the probability curves, and thus the square of the difference of the means, $[\langle L \rangle_2 - \langle L \rangle_1]^2$, rises. On the other hand, a low amount of noise reduces the spread of the curves and makes them much thinner. The distance between the peaks stays constant. As a result, the average of the variance, $\frac{1}{2} \cdot [\sigma_1^2 + \sigma_2^2]$, decreases. In both cases, the detectability index increases as the curves overlap less [Heeger 1997].

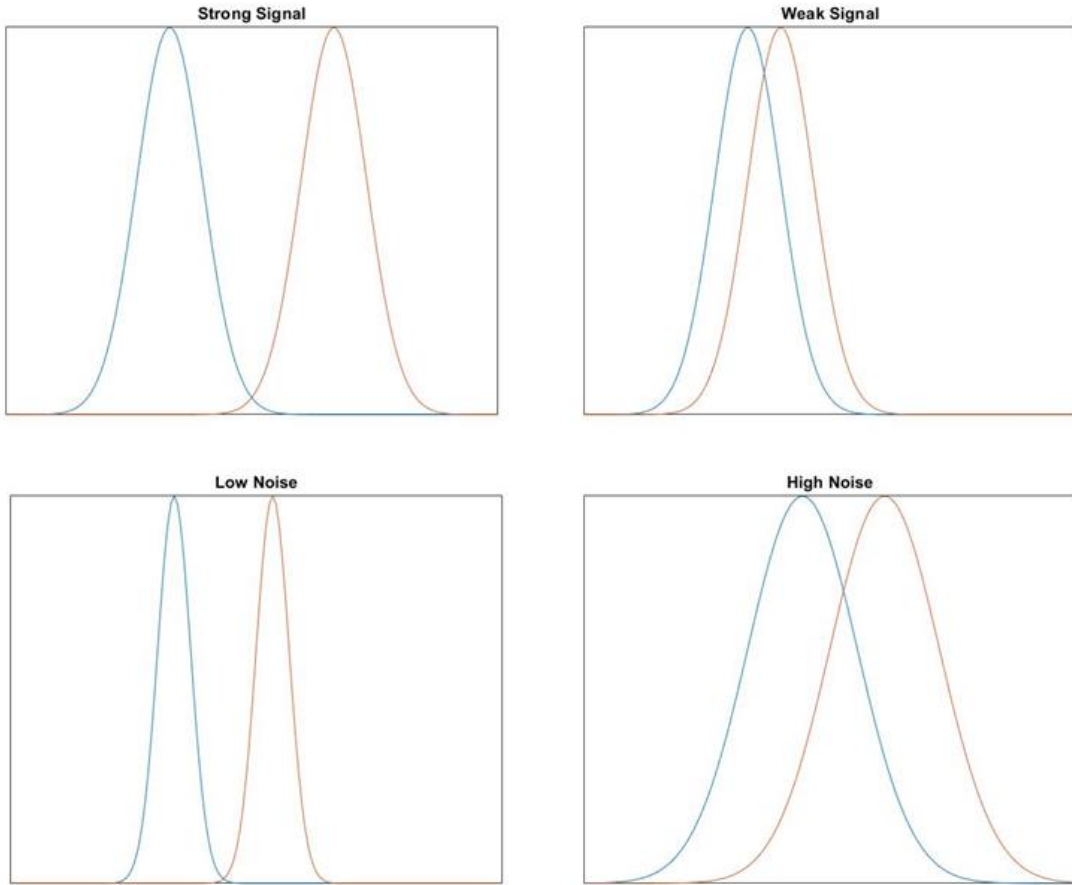


Figure 4.4: Probability distributions curves for two different signal strengths and two different noise levels. The figures are reproduced from [Heeger 1997]

For the task-based assessment, a detailed description of the selected observer is of crucial importance in addition to the definition of the task and figure of merit. The observer is defined as the entity (human or numerical) that performs the task and makes the decision. In chapter 5 we will introduce and analyze the performance of the widely used numerical observers by means of a detection task.

5 Model Observers

In this chapter, different model observers for the calculation of the detectability index d' will be described. We will focus on three different categories and illustrate their mathematical and physical approaches. The parameters displayed in these models are explained in the last section of this chapter. We will also present the methods and approaches with which they are determined.

As a common figure of merit for the model observers, we use the signal-to-noise ratio (SNR) already presented in section 4.2. For a detection task and a Gaussian distributed likelihood-ratio decision function L (also noted as test statistic), we define the detectability index d' as:

$$d'^2_{3D} = \frac{[\langle L \rangle_2 - \langle L \rangle_1]^2}{\frac{1}{2} \cdot [\sigma_1^2 + \sigma_2^2]} \quad (5.1)$$

The subscript “3D” assumes that the observer can capture the full correlations within the volume data, e.g. detection of a sphere in a 3D part. However, in order to compare the performance of a model observer with a human observer who scrolls through the slices of a volume, it is necessary to calculate a 2D detectability index for each slice, e.g. detection of a disk in a 2D image [Gang et al. 2011].

The model observers are applied on the reconstructed images. This is comprehensible since it is difficult for a human to detect very small features in a sinogram. Therefore, for a reconstructed object μ from the projections y , we use the test statistic in the form $L = L(\mu(y))$. Here we assume that the true and the reconstructed objects are equal ($\mu = \hat{\mu}$). For the different types of the linear model observers mentioned in this chapter, the test statistic is defined as the inner product in spatial domain of a template w and the reconstructed object μ . The difference between them lies in the expression of the template [Vennart 1997]:

$$L(\hat{\mu}) = w^T \cdot \mu(y) \quad (5.2)$$

The use of linear model observers has another positive aspect, as they can also be applied to assess the reconstruction methods [Yendiki et al. 2004]. Therefore, we will use the detectability index to quantify the quality of the reconstructed feature.

5.1 Pre-Whitening Model Observer (PW)

The first model observer represents the so-called Pre-Whitening Model Observer, which is formulated to remove or minimize correlations present in the noise. The noise is treated here as white noise. The PW observer assumes that both the mean and the variance of the background μ_b and only the mean of the feature signal μ_f are known. The PW template is then defined as the difference between the signals expected for the feature-present and feature-absent cases weighted by a noise factor [Vennart 1997] [Yendiki et al. 2004]:

$$w_{PW} = \text{Cov}\{\mu\}_1^\dagger (\langle\mu\rangle_2 - \langle\mu\rangle_1) \quad (5.3)$$

Where, the superscript “ \dagger ” denotes the pseudo-inverse of a matrix. It is a generalization of the known inverse matrix to singular and non-square matrices. For the sake of simplicity, we will replace it with the superscript “ $-I$ ” in the other equations. $\langle\mu\rangle_i$ and $\text{Cov}\{\mu\}_i$ are the mean and the covariance of the reconstructed data under hypothesis H_i . The inverse of $\text{Cov}\{\mu\}_i$ is the term responsible for removing noise correlations in the feature and background signals.

The mean values of the data can be obtained by using a linear system transfer function g and we write [Vennart 1997]:

$$\begin{aligned} \langle\mu\rangle_1 &= g \mu_b \\ \langle\mu\rangle_2 &= g (\mu_b + \mu_f) \end{aligned} \quad (5.4)$$

To simplify the notation of the image noise covariance matrix, we introduce:

$$C_{n_i} \equiv \text{Cov}\{\mu\}_i \quad (5.5)$$

Where, n stands for noise. In the case of an additive (independent of the signal amplitude), zero-mean and Gaussian distributed noise, then the covariance C_{n_i} and the variance σ_i^2 under both hypotheses are equal:

$$\begin{aligned} C_n &= C_{n_1} = C_{n_2} \\ \sigma_n^2 &= \sigma_1^2 = \sigma_2^2 \end{aligned} \quad (5.6)$$

The diagonal elements of the covariance matrix $(C_n)_{jj}$ are equal to the variance σ_n^2 . And if the noise is position-independent, then C_n is a diagonal matrix and we have:

$$C_n = \sigma_n^2 I \quad (5.7)$$

Where, I is the unit matrix.

In image quality assessment of CT images, there are numerous models of noisy backgrounds. Examples of the main three of these models are shown in Figure 5.1 [Zhangh 2014], where:

- Additive White Gaussian Noise: is the simplest noise model. It is statistically independent of the signal and has a Gaussian amplitude distribution. Like white color, the white noise has a uniform power across all frequency bands.
- Correlated Gaussian Noise: is generated by convolving the additive white noise with a 2D Gaussian kernel.
- Lumpy Background: is a more complex noise model in clinical images. A random number of Gaussian functions are applied at random locations of the image. These functions are also called lumps. Their number is selected according to a Poisson distribution.

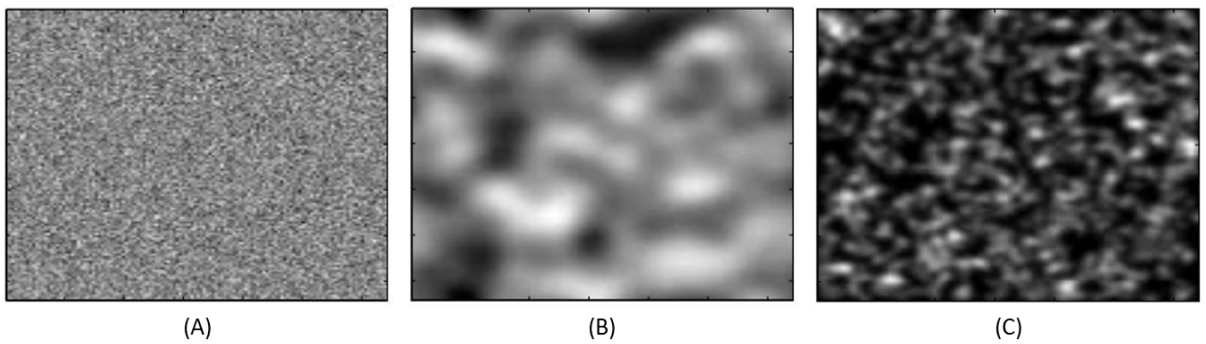


Figure 5.1: Three examples of noise models: (A) White Gaussian Background, (B) Correlated Gaussian Background, and (C) Lumpy Background [Zhangh 2014]

With the above definitions in equations (5.4) and (5.5) the PW template in (5.3) can be rewritten as [Vennart 1997]:

$$w_{PW} = C_n^{-1} g \mu_f \quad (5.8)$$

Inserting the template from (5.8) in the expression of the test statistic of (5.2) results in:

$$\begin{aligned} L_{PW} &= w_{PW}^T \mu \\ &= (C_n^{-1} g \mu_f)^T \mu \\ &= (g \mu_f)^T (C_n^{-1})^T \mu \\ &= (g \mu_f)^T C_n^{-1} \mu \end{aligned} \quad (5.9)$$

Like equation (5.4), the mean values of the test statistics for both hypotheses can be written as follows:

$$\begin{aligned} \langle L_{PW} \rangle_1 &= (g \mu_f)^T C_n^{-1} (g \mu_b) \\ \langle L_{PW} \rangle_2 &= (g \mu_f)^T C_n^{-1} (g (\mu_b + \mu_f)) \end{aligned} \quad (5.10)$$

For the case of Gaussian distributed noise (as assumed in equation (5.6)), the test statistic L_{PW} is also Gaussian distributed, so that the difference of the means is equal to the average of the variances. This assumption is true for almost all linear model observers because the test statistic in equation (5.2) is equivalent to a summation operation over all voxels of the volume. Thus, the Central Limit Theorem guarantees that this assumption is usually satisfied. It assumes that the statistical distribution of a normalized sum of randomly distributed variables can be approximated to be a normal distribution [Vaishnav et al. 2014].

This yields to the following spatial representation of the detectability index in equation (5.1):

$$\begin{aligned} d'^2_{PW} &= \langle L_{PW} \rangle_2 - \langle L_{PW} \rangle_1 = \frac{1}{2} \cdot [\sigma_1^2 + \sigma_2^2] = \sigma_n^2 \\ &= (g \mu_f)^T C_n^{-1} (g \mu_f) \end{aligned} \quad (5.11)$$

Computing the inversion of the covariance matrix in spatial domain can be very difficult and time-consuming due to its high dimensionality. For the reconstruction of an object represented by (512 x 512 x 512) voxels, C_n has ca. 18×10^{15} elements. As will be discussed in detail in section 5.6.1, the calculation in the frequency domain is more convenient. For this we substitute the parameters presented above by the corresponding Fourier transforms, with:

$$\begin{aligned} C_n &\xrightarrow{\mathcal{F}} NPS \\ \mu_f &\xrightarrow{\mathcal{O}} W_{Task} \\ g &\xrightarrow{\mathcal{O}} OTF \end{aligned} \quad (5.12)$$

Where, NPS is the Noise Power Spectrum, W_{Task} is the task Template, and OTF is the Optical Transfer Function. In section 5.6 these individual parameters and their physical meanings are discussed in detail [Vennart 1997].

When replacing the spatial coordinates with the frequency coordinates of the test statistic on equation (5.9), one obtains [Vennart 1997]:

$$L_{PW} = \iiint \frac{OTF \cdot W_{Task}}{NPS} \mathcal{F}\{\mu\} df_x df_y df_z \quad (5.13)$$

As a next step and identical to (5.10), the mean values can be directly transformed to the frequency domain, such that:

$$\begin{aligned} \langle L_{PW} \rangle_1 &= \iiint \frac{|OTF|^2 \cdot W_{Task}}{NPS} \mathcal{F}\{\mu_b\} df_x df_y df_z \\ \langle L_{PW} \rangle_2 &= \iiint \frac{|OTF|^2 \cdot W_{Task}}{NPS} \mathcal{F}\{\mu_b + \mu_f\} df_x df_y df_z \end{aligned} \quad (5.14)$$

Through subtraction of both equations in (5.14) and by knowing that $W_{Task} = \mathcal{F}\{\mu_f\}$, the detectability index can be modeled by the following equation in the frequency domain:

$$d'^2_{PW,3D} = \iiint \frac{(MTF \cdot W_{Task})^2}{NPS} df_x df_y df_z \quad (5.15)$$

Where, MTF is the Modulation Transfer Function and is defined as the modulation (i.e. the real part) of the Optical Transfer Function OTF. As will be shown in section 5.6.1, MTF is an appropriate measure for the spatial resolution of an image. In general, the spatial resolution is defined as the imaging system's ability to distinguish between two neighboring lines [Buzug 2008].

The pre-whitening step (modeled in frequency domain by NPS) causes frequencies at which the noise is large to be downplayed.

According to the current state of knowledge, the behavior of the detectability index applied on images with high-contrast is best evaluated with a Pre-Whitening Model Observer in Fourier-domain [Racine et al. 2017].

- **Pre-Whitening Model Observer with Eye Filter and internal Noise (PWEi)**

The second model observer in this thesis evaluates the detectability based on an anthropomorphic observer. This takes in consideration the human Contrast Sensitivity Function (CSF). The purpose of considering the human performance is to have a good correlation between model and human observers. This was mainly studied when the model observer was to replace or imitate a human, e.g. a radiologist in the field of medicine or a tester/inspector in the industry. The human Contrast Sensitivity Function (CSF) can be mathematically approximated by an Eye Filter and an Internal Noise model [Gang et al. 2011].

In the literature several eye filters are introduced, depending on which model observer is applied. Most of the developers of the model observers have also introduced a corresponding eye filter. For the sake of simplicity, we will introduce only two different eye filters in section 5.6.3. The internal noise describes the human inefficiency when performing different perceptual tasks. This perceptual disturbance has root in different processes e.g. the fluctuations in neural firing or information loss during neural transmission. We will go over it in more detail in section 5.6.4.

The PW model observer has a higher detection index than a human observer. This is well illustrated in Figure 5.2. For an ideal observer, the disks on both images are almost equally visible. In other words, it can detect small or hard-to-see features with high accuracy. For the trajectory optimization this can be problematic as we are looking for the best projections. Here,

the purpose of the eye filter and the internal noise is to downgrade the performance of the ideal observers for bad projections.

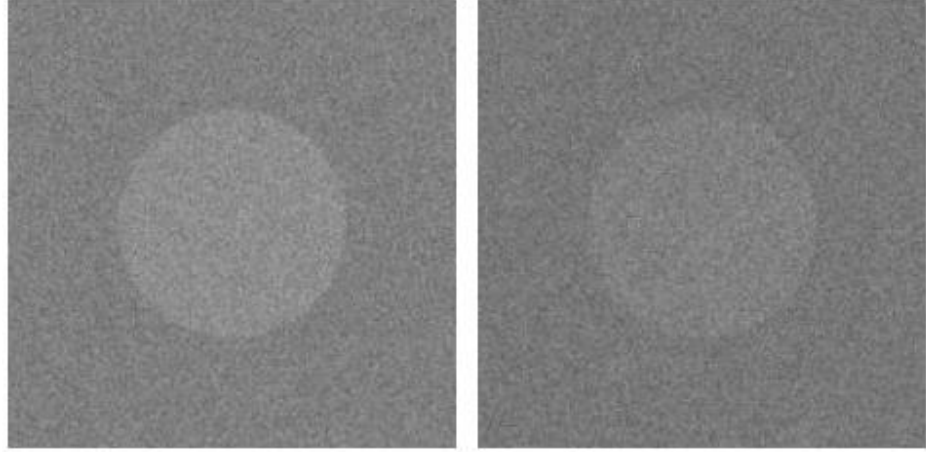


Figure 5.2: Unlike the human eye, for an ideal observer like the PW model observer both disks are equally difficult to distinguish from the background

The test statistic of an anthropomorphic model observer in equation (5.2) can be estimated in spatial domain using [Vaishnav et al. 2014]:

$$\begin{aligned} L(\hat{\mu}) &= \overbrace{(E \cdot w)^T}^{\triangleq w^T} \cdot \overbrace{(E \cdot \mu)}^{\triangleq \mu} \\ &= (E^T \cdot E \cdot w)^T \cdot \mu \end{aligned} \quad (5.16)$$

Where, E is the eye filter which is assumed to be radially symmetric in the frequency domain. To present $L(\hat{\mu})$ in the spatial coordinates, then the inverse of the Fourier Transform of the Eye filter must be applied. Inserting the PW template from equation (5.8) into the test statistic gives the following expression:

$$L(\hat{\mu}) = (E^T \cdot E \cdot (C_n^{-1} g \mu_f))^T \cdot \mu \quad (5.17)$$

The derivation scheme explained for the PW model observer is used here to obtain the PWEi detectability index. After some algebra we get [Gang et al. 2011]:

$$d'^2_{PWEi,3D} = \iiint \frac{E^2 \cdot (MTF \cdot W_{Task})^2}{E^2 \cdot NPS + N_i} df_x df_y df_z \quad (5.18)$$

Where, N_i is the internal noise.

- **2D PW-based Model Observers**

However, 3D eye filters and exact form of internal noise for fully 3D data are subjects of current research. There are no established models for 3D images [Gang 2014]. This means that the anthropomorphic observers can only be used if the trajectory is optimized for a 2D feature in a single 2D object slice. For this reason, the 2D detectability index is derived from the 3D formulation by integrating the above equations across the direction orthogonal to the 2D image [Gang et al. 2011]. In this work, we defined the direction perpendicular to the 2D slices as f_z . The integration leads to:

PW Model Observer:

$$d'^2_{PW,2D} = \iint \frac{(\int MTF \cdot W_{Task} df_z)^2}{\int NPS df_z} df_x df_y \quad (5.19)$$

PWEi Model Observer:

$$d'^2_{PWEi,2D} = \iint \frac{E^2 (\int MTF \cdot W_{Task} df_z)^2}{E^2 \int NPS df_z + N_i} df_x df_y \quad (5.20)$$

As the eye filter is assumed to be circularly symmetric, the equation for PWEi model observer can be mathematically simplified by introducing the radial spatial frequency f . The detectability index can then be obtained by a single integration over f , giving [Burgess et al. 1997]:

$$d'^2_{PWEi,2D} = 2\pi \int_0^\infty \frac{E^2 (\int MTF \cdot W_{Task} df_z)^2}{E^2 \int NPS df_z + N_i} f df \quad (5.21)$$

Where, $f = \sqrt{f_x^2 + f_y^2}$.

Furthermore, the 2D formulation allows the comparison with human performance, which can be measured with the 9AFC tests. However, this is not part of this work and may be the subject of future research.

5.2 Non-Pre-Whitening Model Observer (NPW)

Unlike the PW observer, which assumes full knowledge of the noise in background, the Non-Pre-Whitening Model Observer, which was first introduced by Wagner and Weaver in 1972, is modeled by applying a detection template in form of the expected signal. Mathematically, it requires only knowledge of the means of the background μ_b and of the feature signal μ_f . The NPW template is given by [Vennart 1997]:

$$w_{NPW} = \langle \mu \rangle_2 - \langle \mu \rangle_1 \quad (5.22)$$

Comparing with the PW template the term representing the inverse of the covariance matrix does not appear. Therefore, the NPW model observer cannot remove the correlations present in the noise and thus it can correctly handle only white noise.

Using the definition in (5.4) the template transforms into:

$$w_{NPW} = g \mu_f \quad (5.23)$$

The decision function L is then implemented by weighting the image data directly with the template:

$$\begin{aligned} L_{PW} &= w_{NPW}^T \mu \\ &= (g \mu_f)^T \mu \end{aligned} \quad (5.24)$$

The difference of the means of the test statistic from equation (5.24) under both hypotheses can then be expressed by:

$$\langle L_{PW} \rangle_2 - \langle L_{PW} \rangle_1 = (g \mu_f)^T (g \mu_f) \quad (5.25)$$

The average variance of the test statistic under both hypotheses is given by (see equation (5.11)):

$$\sigma_n^2 = (g \mu_f)^T C_g (g \mu_f) \quad (5.26)$$

The average covariance matrix of the data C_g is generalized to include the covariance matrix of the object C_f as an additional source of noise. In medicine, C_f corresponds to the anatomical noise and can be modeled by the anatomical background power spectrum. However, for industrial application, this term disappears, which means [Vennart 1997]:

$$\underbrace{C_g}_{\substack{\text{Average covariance} \\ \text{of the data}}} = g^T \underbrace{C_f}_{\substack{\text{Covariance} \\ \text{of the object}}} g + \underbrace{C_n}_{\substack{\text{covariance} \\ \text{of the noise}}} = C_n \quad (5.27)$$

When applying (5.25) and (5.26) to (5.1), we obtain the detectability index of an NPW model observer in the spatial domain as follows [Vennart 1997]:

$$d'^2_{NPW,3D} = \frac{[(g \mu_f)^T (g \mu_f)]^2}{(g \mu_f)^T C_n (g \mu_f)} \quad (5.28)$$

Just as the PW model observer, the Fourier representation of the NPW detectability index can be written in terms of the definitions in equation (5.12) as [Gang et al. 2011]:

$$d'^2_{NPW,3D} = \frac{[\iiint (MTF \cdot W_{Task})^2 df_x df_y df_z]^2}{\iiint NPS \cdot (MTF \cdot W_{Task})^2 df_x df_y df_z} \quad (5.29)$$

Since the NPW model observer does not contain information about the noise correlation, this is suitable for complicated tasks with an inhomogeneous background. On contrast, the strategy of the PW model observer is not applicable because the probability density function of the data is not known. Here, the assumption of a normal distribution does not apply [Vennart 1997].

- **Non-Pre-Whitening Model Observer with Eye Filter (NPWE):**

The NPW model observer can only be used on certain backgrounds. For example, it fails to predict the performance of a human observer in lumpy backgrounds. Burgess et al. have shown that by adding a spatial frequency filter that mimics the contrast sensitivity function (CSF) of the human eye, the predictive performance of the NPW model observer is significantly improved [Burgess et al. 1997]. Several subsequent studies have confirmed the good applicability of this model [Gang et al. 2011]. The test statistic of the NPWE model observer is then given as [Vaishnav et al. 2014]:

$$\begin{aligned} L(\hat{\mu}) &= (E^T \cdot E \cdot w)^T \cdot \mu \\ &= (E^T \cdot E : (g \mu_f))^T \cdot \mu \end{aligned} \quad (5.30)$$

Thus, we write the equation of the detectability index as [Burgess et al. 1997]:

$$d'^2_{NPWE,3D} = \frac{[\iiint E^2 \cdot (MTF \cdot W_{Task})^2 df_x df_y df_z]^2}{\iiint E^4 \cdot NPS \cdot (MTF \cdot W_{Task})^2 df_x df_y df_z} \quad (5.31)$$

- **Non-Pre-Whitening Model Observer with Eye Filter and Internal Noise (NPWEi)**

The NPW model observer can be extended to include the eye filter and internal noise. First formulated by Ishida et al. in 1984, they proved that adding the internal noise term improves the detection of features with low contrast [Ishida et al. 1984].

$$d'^2_{NPWEi,3D} = \frac{[\iiint E^2 \cdot (MTF \cdot W_{Task})^2 df_x df_y df_z]^2}{\iiint E^4 \cdot NPS \cdot (MTF \cdot W_{Task})^2 + N_i df_x df_y df_z} \quad (5.32)$$

- **2D PW-based Model Observers**

The 2D detectability corresponding to the 3D model observers are [Gang et al. 2011]:

NPW Model Observer:

$$d'^2_{NPW,2D} = \frac{[\iint (\int MTF \cdot W_{Task} df_z)^2 df_x df_y]^2}{\iint (\int NPS df_z) \cdot (\int MTF \cdot W_{Task} df_z)^2 df_x df_y} \quad (5.33)$$

NPWE Model Observer:

$$d'^2_{NPWE,2D} = \frac{[\iint E^2 \cdot (\int MTF \cdot W_{Task} df_z)^2 df_x df_y]^2}{\iint (E^4 \cdot \int NPS df_z) \cdot (\int MTF \cdot W_{Task} df_z)^2 df_x df_y} \quad (5.34)$$

NPWEi Model Observer:

$$\begin{aligned} d'^2_{NPWEi,2D} \\ = \frac{[\iint E^2 \cdot (\int MTF \cdot W_{Task} df_z)^2 df_x df_y]^2}{\iint (E^4 \cdot \int NPS df_z) \cdot (\int MTF \cdot W_{Task} df_z)^2 + N_i df_x df_y} \end{aligned} \quad (5.35)$$

5.3 The Region-of-Interest Observer (ROI)

The simplest model observer is the ROI observer. It requires knowledge only of the mean of the feature signal μ_f . Information about the background is not considered in the ROI template.

Then we can write the template as a simple matched filter step [Yendiki et al. 2006]:

$$w_{ROI} = \langle \mu_f \rangle_2 = g \mu_f \quad (5.36)$$

However, for the detection task of a known feature, the ROI template is the same as the NPW template. Thus, the ROI model observer can be considered as a special case of the NPW model observer, which in our case is the same.

5.4 Hotelling Observer (HO)

Rather than the Pre-Whitening observer, the Hotelling observer requires knowledge of the mean and the covariance of both the background μ_b and the feature signal μ_f . The corresponding template is [Yendiki et al. 2006] [Ott 2016]:

$$w_{HO} = S_\mu^\dagger (\langle \mu \rangle_2 - \langle \mu \rangle_1) \quad (5.37)$$

with

$$S_\mu^\dagger = \frac{1}{2} \left(\overbrace{\text{Cov}\{\mu\}_2}^{c_{n1}} + \overbrace{\text{Cov}\{\mu\}_1}^{c_{n2}} \right) \quad (5.38)$$

Where, S_μ is called the unconditional covariance of μ and built based on two data sets. For the sake of simplicity, the pseudo-inverse index will be replaced by the superscript “-I”.

To determine the detectability index, we need first to calculate the difference of the means and the average covariance. Analogous to the PW approach, we obtain:

$$\langle L_{HO} \rangle_2 - \langle L_{HO} \rangle_1 = (g \mu_f)^T S_\mu^{-1} (g \mu_f) \quad (5.39)$$

And,

$$\begin{aligned} \sigma_1 &= (g \mu_f)^T S_\mu^{-1} C_{n1} S_\mu^{-1} (g \mu_f) \\ \sigma_2 &= (g \mu_f)^T S_\mu^{-1} C_{n2} S_\mu^{-1} (g \mu_f) \end{aligned} \quad (5.40)$$

The equations (5.39) and (5.40) substituted in (5.1) deliver the Hotelling detectability index in the spatial domain as:

$$d'^2_{HO} = (g \mu_f)^T S_\mu^{-1} (g \mu_f) \quad (5.41)$$

Since we are using Gaussian distributed additive noise and background, the covariance matrices of the data under both hypotheses are equal. It follows that

$$S_\mu = C_{n1} = C_{n2} = C_n \quad (5.42)$$

This leads to:

$$d'^2_{HO} = (g \mu_f)^T C_n^{-1} (g \mu_f) = d'^2_{PW} \quad (5.43)$$

In this special case, the Hotelling observer reduces to a PW approach if there is no object variability.

In general, the Hotelling observer can be interpreted as a generalized PW model observer.

5.5 Channelized Hotelling Observer (CHO)

As explained in section 5.1, the computational effort for computing the inverse of the covariance matrix is extremely high. One approach to solve this problem is the use of the Fourier Transform. This has been applied for the PW and NPW model observers (see sections 5.1 and 5.2). However, another widely used method is the channelization. This approach in combination with a model observer has been first examined by Myers and Barrett in 1987. Conceptually, the reconstructed image μ undergoes a set of frequency-based channels prior to processing. This filtering step is not invertible and provides the channelized image v as [Myers et al. 1987]:

$$\underset{N_c \times 1}{\underline{\underline{v}}} = \underset{M \times N_c}{U}^T \cdot \underset{M \times 1}{\underline{\underline{\mu}}} \quad (5.44)$$

Where, the reconstructed image μ with the original dimension M must be given in the Fourier domain before processing by the channels and, the dimension of the channelized image v is equal to the number of selected channels N_c . As $N_c \ll M$, the introduction of the channeling operator U allows to reduce immensely the dimension of the data with only minimal loss of information. This operator includes a set of channels u_i , that will be introduced later in this section, and is defined as:

$$U = [u_1, u_2, \dots, u_{N_c}] \quad \text{with } u_i^T u_i = 1 \quad (5.45)$$

Instead of defining the template based on the original image like the PW model observer (see equation (5.3)), The template of the channelized Hotelling observer is defined as the product of the inverse of the covariance matrix of the channel responses and the difference of the means of the feature-present and feature-absent channel responses vectors, or equivalently [Brankov 2013]:

$$w_{CHO} = C_v^{-1} (\langle v \rangle_2 - \langle v \rangle_1) \quad (5.46)$$

With:

$$\overbrace{\langle v \rangle_2 - \langle v \rangle_1}^{\Delta \bar{v}} = U^T \left(\overbrace{\langle \mu \rangle_2 - \langle \mu \rangle_1}^{\Delta \bar{\mu}} \right) = U^T \Delta \bar{\mu} \quad (5.47)$$

And,

$$C_v = \frac{1}{2} (C_{v_2} + C_{v_1}) \quad (5.48)$$

For a Gaussian-distributed additive noise, as assumed in the previous model observers, the average covariance matrices of the channel responses are the same under both hypotheses. This

means: $C_v = C_{v_2} = C_{v_1}$. In their work, Myers and Barrett have proven that C_v can be expressed in relation to the original noise covariance matrix C_n as follows [Myers et al. 1987]:

$$\underbrace{C_v}_{N_c \times N_c} = U^T \underbrace{C_n}_{M \times M} U \quad (5.49)$$

The size of the covariance matrix C_n of the Hotelling observer (see equation (5.42)) is then reduced to the number of channels. For example, C_n has 512^4 elements for a 512×512 image, where the size of C_v is only 100 for the channelization with 10 channels. This huge simplification allows to calculate the inverse of the new reduced covariance matrix C_v without any computational burden. However, it remains that C_n is more difficult to calculate than MTF and NPS for the PW and NPS model observers [Russo 2017]. Per definition, the covariance matrix can be calculated as:

$$C_v = \langle [v - \bar{v}] [v - \bar{v}] \rangle \quad (5.50)$$

Or in dependence of the original image:

$$C_v = U^T \overbrace{\langle [\mu - \bar{\mu}] [\mu - \bar{\mu}]^T \rangle}^{C_n} U \quad (5.51)$$

Where, $\bar{\mu}$ can be understood as the expectation value of the image μ .

By applying the equations (5.47) and (5.49) into (5.46), the CHO template can be modeled as:

$$w_{CHO} = (U^T C_n U)^{-1} (U^T \Delta \bar{\mu}) \quad (5.52)$$

The test statistic in equation (5.2) can be then expressed as:

$$\begin{aligned} L(v) &= w_{CHO}^T \cdot v \\ &= [(U^T C_n U)^{-1} (U^T \Delta \bar{\mu})]^T (U^T \mu) \\ &= [U (U^T C_n U)^{-1} (U^T \Delta \bar{\mu})]^T \mu \\ &= w_{CHO,\mu}^T \cdot \mu \end{aligned} \quad (5.53)$$

Where, the CHO test statistic applies the spatial template $w_{CHO,\mu}$ to the reconstructed image μ . As discussed in section 5.1 for the PW observers, the difference of the means is equal to the average of the variances for Gaussian-distributed test statistic, and we obtain

$$\begin{aligned} d'^2_{CHO} &= \langle L_{CHO}(v) \rangle_2 - \langle L_{CHO}(v) \rangle_1 \\ &= w_{CHO,\mu}^T \cdot \Delta \bar{\mu} \end{aligned} \quad (5.54)$$

In radiology, CHO observers are often used to detect nodules. They gained popularity as they correlate very well with the performance of human observers [Vaishnav et al. 2014]. Thus, they are used to evaluate low-contrast detectability [Racine et al. 2017].

- **Channels**

Channelization with so called anthropomorphic channels, that incorporate knowledge about the human visual system (HVS), can better model the frequency selectivity of human observers. The idea behind this approach is to assume that the human visual system can be discretized by multiple channels, while each channel is sensitive to a different frequency range [Vaishnav et al. 2014]. Example of these channels that can be used with the CHO observers are: Square (SQR), Gabor (GB), Sparse Difference of Gaussians (S-DOG) and Dense Difference of Gaussians (D-DOG) channels. Additionally, there exist some channels that are used to correlate with the detection performance of ideal observers. An example is the use of Laugerre-Gauss (LG) channels [Petrov et al. 2019].

Gabor Channels (GB):

The Gabor channels have physiological and psychophysical bases. They describe the frequency response of neurons to a small spot of light as a function of position [Vaishnav et al. 2014].

The function of each Gabor channel is defined by multiplying a Gaussian function with a Sinusoidal wave in the spatial domain [Ferrero et al. 2017].

$$C_j(x, y) = e^{-4\ln(2)} \frac{(x - x_0)^2 + (y - y_0)^2}{\omega_s^2} \cos[2\pi f_c((x - x_0)\cos\theta + (y - y_0)\sin\theta) + \gamma] \quad (5.55)$$

Where,

j	The number of the channel
(x_0, y_0)	The position of the feature
(x, y)	The coordinates of each pixel on the image
ω_s	The channel width (given in cycles per pixels)
f_c	The central frequency (given in cycles per pixels and is related to ω_s)
θ	The orientation angle
γ	A phase offset

Each Gabor channel will be parametrized by the channel width and the angular orientation.

Sparse and Dense Difference-of-Gaussians Channels (S-DOG and D-DOG):

The Difference-of-Gaussians Channels (DOG) are radially symmetrical overlapping functions. They are expressed as the difference between two Gaussian functions with two different

standard deviations. In dependency of the radial frequency, the function of the j -channel is defined as [Petrov et al. 2019]:

$$C_j(f) = e^{-\frac{1}{2}\left(\frac{f}{Q\sigma_j}\right)^2} - e^{-\frac{1}{2}\left(\frac{f}{\sigma_j}\right)^2} \quad (5.56)$$

Where,

j The number of the channel

f The radial frequency. It is equal to $\sqrt{f_x^2 + f_y^2}$

σ_j The standard deviation of each channel

Q defines the width of the channel

σ_j will be expressed using the standard deviation of the first channel and we obtain: $\sigma_j = \alpha^j \sigma_0$. The parameter α gives the difference of the standard deviation between the channels.

Depending on these parameters, two different DOG channel models have been introduced according to Table 5-1 [Abbey et al. 2001].

Table 5-1: Parameters for S-DOG and D-DOG channel models

	S-DOG	D_DOG
σ_0	0.015	0.005
α	2.0	1.4
Q	2.0	1.67

This type of channels has been only used in few studies. However, it has shown little advantage in predicting human observer performance [Abbey et al. 2001].

Square Channels (SQR):

The simplest type of channels are the square channels. They are radially symmetric and have a square bandpass profile. The radial symmetry is justified by the assumption that the noise covariance and the expected signal profile are also radially symmetric. This leads to a lower number of needed channels. Each SQR-channel is given by a lower and an upper frequency, while the upper frequency of the previous channel defines the starting frequency of the next channel. The upper frequency of the j -channel can be represented by: $f_j = f_0 \alpha^j$. Here, f_0 is the starting frequency of the first channel and is assumed to be 0.015, while the parameter α is set to 2.0. The general form of an SQR channel can be summarized as [Abbey et al. 2001]:

$$C_j(f) = \begin{cases} 0 & \text{for } f \leq f_0 \alpha^{j-1} \\ 1 & \text{for } f_0 \alpha^{j-1} < f \leq f_0 \alpha^j \\ 0 & \text{for } f > f_0 \alpha^j \end{cases} \quad (5.57)$$

Laguerre-Gauss Channels (LG):

The LG channels are symmetrically rotational channels with no preferred orientation formed as a product of Laguerre polynomials and Gaussian functions. Thus, they are suitable for orientation-independent features like circular and spherical targets [Vaishnav et al. 2014]. Each LG channel is given by [Petrov et al. 2019]:

$$C_j(r) = \frac{\sqrt{2}}{a} e^{\frac{-\pi r^2}{a^2}} L_j\left(\frac{2\pi r^2}{a^2}\right) \quad (5.58)$$

Where,

- j The number of the channel
- a The width of the LG functions
- L_j The Laguerre polynomial
- $r = (x - x_0)^2 + (y - y_0)^2$

For the LG channels, only the term a is tuned to match the performance of a human observer.

It is defined as $a = \sqrt{2\pi}\sigma$. The standard deviation factor σ ranges typically from 3 to 100.

The Laguerre polynomial is given as:

$$L_j(x) = \sum_{k=0}^j (-1)^k \binom{j}{k} \frac{x^k}{k!} \quad (5.59)$$

The LG channels are efficient when performing detection tasks on Gaussian noise or Gaussian backgrounds.

5.6 Definition of the parameters in Model Observers

5.6.1 MTF & NPS

As can be seen from the derivation of the model observers, the detectability index d' requires two specific image quality metrics, namely the Modulation Transfer Function (MTF) and Noise Power Spectrum (NPS).

Definition:

Modulation Transfer Function (MTF): is an important characteristic of an imaging system. It describes its overall spatial resolution at all available frequencies. Unlike CNR (see section 4.1), MTF is directly dependent of the pixel size of the image and the properties of the hardware (e.g. X-ray source) and software (e.g. Reconstruction algorithm) used in the imaging system [Buzug 2008].

MTF can be estimated as the absolute value of the Optical Transfer Function (OTF). OTF itself can be obtained from the Fourier Transform of the Point Spread Function (PSF). The determination of PSF takes place directly on the acquired image. For a 2D CT image the relationship between MTF and PSF can be summarized in the following equation [Williams et al. 2002]:

$$MTF(f_x, f_y) = |OTF(f_x, f_y)| \quad (5.60)$$

with $OTF(f_x, f_y) = \mathcal{F}\{PSF(x, y)\}$

In other words, MTF describes how well frequencies are transmitted through the imaging system. For the ideal case the system is independent of the input frequency and thus MTF can be directly obtained from the Line Spread Function (LSF).

Noise Power Spectrum (NPS): describes in the Fourier domain the noise amplitude as a function of the entire range of frequency in the image. The Noise in an imaging system can be divided into two main categories: Quantum Noise and Electronic Noise. The quantum noise is generated by the variation of the X-ray quanta that are transmitted to the detector through the object. On the other hand, the detector noise is caused by the electronics of the detector [Buzug 2008].

To compute the 2D NPS, the image is split into small homogenous ROIs. Then the following equation is applied [Tseng 2015]:

$$NPS(f_x, f_y) = \frac{\Delta x}{L_x} \frac{\Delta y}{L_y} \frac{1}{N} \sum_{i=1}^N |\mathcal{F}\{ROI_i(x, y) - \overline{ROI}_i\}|^2 \quad (5.61)$$

where, Δx and Δy are the pixel sizes in the horizontal and vertical directions; L_x and L_y are the dimensions of the ROI; N is the number of the ROIs; and \overline{ROI}_i is the mean value of i -th ROI.

The relationship between the variance σ^2 and NPS for the 2D case is given by:

$$\sigma^2 = \iint NPS(f_x, f_y) df_x df_y \quad (5.62)$$

Requirements for Fourier Transformation:

Linearity and Shift-Invariance:

Due to the importance of linearity and shift-invariance for the application of the Fourier transform in the field of signal processing for CT [Gang 2014], they are briefly presented here.

An imaging system is linear when the output from a weighted sum of input signals is equal to the weighted sum of the output from each input signal. For a system using the Fourier transform \mathcal{F} , this means in the 3D case [Gang 2014]:

$$\mathcal{F}\{a f_1(x, y, z) + b f_2(x, y, z)\} = a \mathcal{F}\{f_1(x, y, z)\} + b \mathcal{F}\{f_2(x, y, z)\} \quad (5.63)$$

The shift-invariance, or alternatively position or translation invariance, requires that an argument shifting in the input signal produces an identical shift in the output signal. If $g(x, y, z)$ is the Fourier transform of $f(x, y, z)$, then the system must also fulfill for arbitrary x_0, y_0, z_0 [Gang 2014]:

$$g(x - x_0, y - y_0, z - z_0) = \mathcal{F}\{f(x - x_0, y - y_0, z - z_0)\} \quad (5.64)$$

For a linear and shift-invariant system (LSI), the Fourier analysis can then be used. This results in MTF and NPS being the same for all positions in the image.

However, these requirements are only met by a few imaging systems. In the case of a flat panel detector, linearity is satisfied just within an exposure range below a certain pixel saturation value. E.g. a detector is nonlinear if 50 % of its pixels are saturated. On the other side, the shift-invariance condition is violated by digital imaging systems as they divide an image to a limited number of pixels. Nevertheless, these systems are considered to be cyclically invariant because a translation equal to pixel spacing under certain imaging conditions allows the use of the Fourier analysis [Gang 2014].

Stationarity:

A random process is stationary if the probability distribution of its properties, such as the mean signal and the variance, are constant in space.

There are different degrees of stationarity. A process is called wide-sense stationary (WSS) or weakly stationary if the mean and the autocorrelation (first and second-order of its image statistics) are invariant to translation in space. This assumption is sufficient for power spectral analysis. Processes that have statistical properties that vary cyclically in space are referred to as cyclostationarity. The stationarity can be quantified by the difference between the diagonal and off-diagonal elements of the covariance matrix in Fourier domain.

A linear and shift-invariant imaging system that has a WSS process as input will reproduce a WSS process as output. This is a key property for the calculation of the Fourier domain NPS [Gang 2014].

Mathematical Formulation for Penalized-Likelihood Reconstruction:

Due to the spatially variable properties of the image quality when using iterative reconstruction techniques, conventional methods for determining MTF and NPS, can only be used to a very limited extent since these originate from location-independent image quality properties. However, the PL reconstruction (see section 3.1.2) allows a local estimation of these metrics [Stayman et al. 2004]. Due to this important property, we will continue to work with this reconstruction method.

As will be shown in the general framework for trajectory optimization in section 6.1.1, MTF and NPS must be calculated for every set of projections in each iteration. This means first computing the 3D reconstruction for this set of projections and then measuring both metrics. This is time consuming and can be avoided by using appropriate predictors for MTF and NPS without performing the actual reconstruction.

Stayman and Fessler (2004) proposed a method for predicting the local MTF and local NPS for a quadratic penalty PL reconstruction since both are the Fourier transforms of the Point Spread Function (PSF) and the Covariance (Cov). For an implicitly defined estimator, such as the PL estimator presented in section 3.1.2, the local PSF and Covariance can be written by applying the first-degree Taylor Polynomial and the implicit function theorem as follows [Stayman et al. 2004]:

$$[PSF\{\hat{\mu}\}]_j = [-\nabla^{20}\Phi(\hat{\mu}; \bar{y}(\mu))]^{-1} \cdot \nabla^{11}\Phi(\hat{\mu}; \bar{y}(\mu)) \cdot \frac{\partial}{\partial \mu_j} \bar{y}(\mu) \quad (5.65)$$

$$\begin{aligned} [Cov\{\hat{\mu}\}]_j &= [-\nabla^{20}\Phi(\hat{\mu}; \bar{y}(\mu))]^{-1} \cdot \nabla^{11}\Phi(\hat{\mu}; \bar{y}(\mu)) \cdot Cov\{y(\mu)\} \cdot \\ &\quad [\nabla^{11}\Phi(\hat{\mu}; \bar{y}(\mu))]^T \cdot [-\nabla^{20}\Phi(\hat{\mu}; \bar{y}(\mu))]^{-1} \end{aligned} \quad (5.66)$$

Where,

$y(\mu)$	The tomographic measurements
$\bar{y}(\mu)$	The mean of the tomographic measurements
$\hat{\mu}$	The reconstructed object with the mean measurements
μ	The exact representation of the object
∇^{20}	Operator that yields a 2D matrix where the (j, k) -th element is $\frac{\partial^2}{\partial \mu_j \partial \mu_k}$
∇^{11}	Operator that yields a 2D matrix where the (j, i) -th element is $\frac{\partial^2}{\partial \mu_j \partial y_i}$
$Cov\{y(\mu)\}$	The covariance of the measurements. It is assumed to be a diagonal matrix

These approximations are expressed in a closed form and depend only on the partial derivatives of the objective function $\Phi(\hat{\mu}; \bar{y}(\mu))$.

Applying (5.5) and (5.6) for the PL estimator in (3.2) gives:

$$[PSF\{\hat{\mu}\}]_j = [\mathbf{A}^T \mathbf{D}\{\bar{y}\} \mathbf{A} + \beta \mathbf{R}]^{-1} \mathbf{A}^T \mathbf{D}\{\bar{y}\} \mathbf{A} e_j \quad (5.67)$$

$$[Cov\{\hat{\mu}\}]_j = [\mathbf{A}^T \mathbf{D}\{\bar{y}\} \mathbf{A} + \beta \mathbf{R}]^{-1} \mathbf{A}^T \mathbf{D}\{y\} \mathbf{A} [\mathbf{A}^T \mathbf{D}\{\bar{y}\} \mathbf{A} + \beta \mathbf{R}]^{-1} e_j \quad (5.68)$$

Here the system matrix \mathbf{A} is called the forward projector, its transpose \mathbf{A}^T is the back-projection operator, $\mathbf{D}\{y\}$ denotes a square diagonal matrix with the measurements y as diagonal entries, e_j is a unit vector with the j -th element equal 1 and otherwise zero. This vector extracts a column from $PSF\{\hat{\mu}\}$ and $Cov\{\hat{\mu}\}$ corresponding to the location given by voxel j . When the mean data of the measurements $\bar{y}(\mu)$ are not available, the noisy measurement $y(\mu)$ can be used. This is possible as the forward- and back-projection operators are smoothing operators and both estimators of PSF and Cov are robust against noise effects [Stayman et al. 2004]. The local PSF and Cov are circulant matrices for locally space-invariant imaging system. This means that every row is the same as the previous but shifted to the right by one column. In this case a circulant approximation can be used to avoid the expensive computation of the matrix inverses, resulting in [Stayman et al. 2004]:

$$[PSF\{\hat{\mu}\}]_{j,circulant} = \mathcal{F}^{-1} \left\{ \frac{\mathcal{F}\{e_j\} \odot \mathcal{F}\{\mathbf{A}^T \mathbf{D}\{y\} \mathbf{A} e_j\}}{\mathcal{F}\{\mathbf{A}^T \mathbf{D}\{y\} \mathbf{A} e_j + \beta \mathbf{R} e_j\}} \right\} \quad (5.69)$$

$$[Cov\{\hat{\mu}\}]_{j,circulant} = \mathcal{F}^{-1} \left\{ \frac{\mathcal{F}\{e_j\} \odot \mathcal{F}\{\mathbf{A}^T \mathbf{D}\{y\} \mathbf{A} e_j\}}{\left| \mathcal{F}\{\mathbf{A}^T \mathbf{D}\{y\} \mathbf{A} e_j + \beta \mathbf{R} e_j\} \right|^2} \right\} \quad (5.70)$$

The operator \odot represents an element-by-element multiplication. The division of both Fourier transform terms is also an element-by-element division. $\mathcal{F}\{\cdot\}$ is a discrete Fourier transform.

If MTF and NPS are also locally stationary within a small neighborhood to voxel j , then the local MTF and NPS can be written as follows [Gang et al. 2017]:

$$MTF_j = \frac{|\mathcal{F}\{\mathbf{A}^T \mathbf{D}\{y\} \mathbf{A} e_j\}|}{|\mathcal{F}\{\mathbf{A}^T \mathbf{D}\{y\} \mathbf{A} e_j + \beta \mathbf{R} e_j\}|} \quad (5.71)$$

$$NPS_j = \frac{|\mathcal{F}\{\mathbf{A}^T \mathbf{D}\{y\} \mathbf{A} e_j\}|}{\left| \mathcal{F}\{\mathbf{A}^T \mathbf{D}\{y\} \mathbf{A} e_j + \beta \mathbf{R} e_j\} \right|^2} \quad (5.72)$$

5.6.2 Task Function W

As mentioned in the introduction, the performance of an imaging system is best evaluated in terms of the imaging task. It can be defined by the location, frequency content and shape of the object of interest. In general, the task function W_{Task} is defined as the difference of the Fourier transforms of two hypotheses presented in the spatial domain. For a detection task, the first hypothesis (signal-present) contains the feature while the second hypothesis (signal-absent) presents the background [Gang et al. 2011].

The spatial representation of a volume-of-interest (VOI) or region-of-interest (ROI) is denoted by $O(x,y,z)$ and the difference of the attenuation coefficients of the signal and background is symbolized by $\Delta\mu$. By applying the above definition for detection on a uniform background, we obtain [Gang et al. 2011]:

$$\begin{aligned} W_{Task} &= \Delta\mu \cdot \mathcal{F}\{O(x,y,z)\} \\ &= (\mu_{Feature} - \mu_{Background}) \cdot \mathcal{F}\{O(x,y,z)\} \end{aligned} \quad (5.73)$$

For pre-whitening and non-pre-whitening model observers, the task function usually occurs as a product with MTF. In other words, we obtain a good detectability if the frequencies of interest defined in the task function are well transmitted by the imaging system.

For industrial applications, a 3D CAD model is mostly available and can be used to determine the task function. This approach will be illustrated in the next chapter. For simple features, the task function can be modeled by using the Heaviside step function. E.g. for the detection of a sphere of a radius r the task function is described by:

$$W_{Task} = \Delta\mu \cdot \mathcal{F}\{O\} = \Delta\mu \cdot \mathcal{F}\{H[r^2 - (x^2 + y^2 + z^2)]\} \quad (5.74)$$

Examples of task functions and their corresponding Fourier transforms are shown in Figure 5.3. To illustrate, we consider $O(x,y,z)$ to be 1 within the circular and rectangular regions and 0 everywhere else. Since the Fourier transform delivers complex numbers, the following Figure 5.3 shows only the magnitude of the Fourier transform $|\mathcal{F}\{O(x,y,z)\}|$.

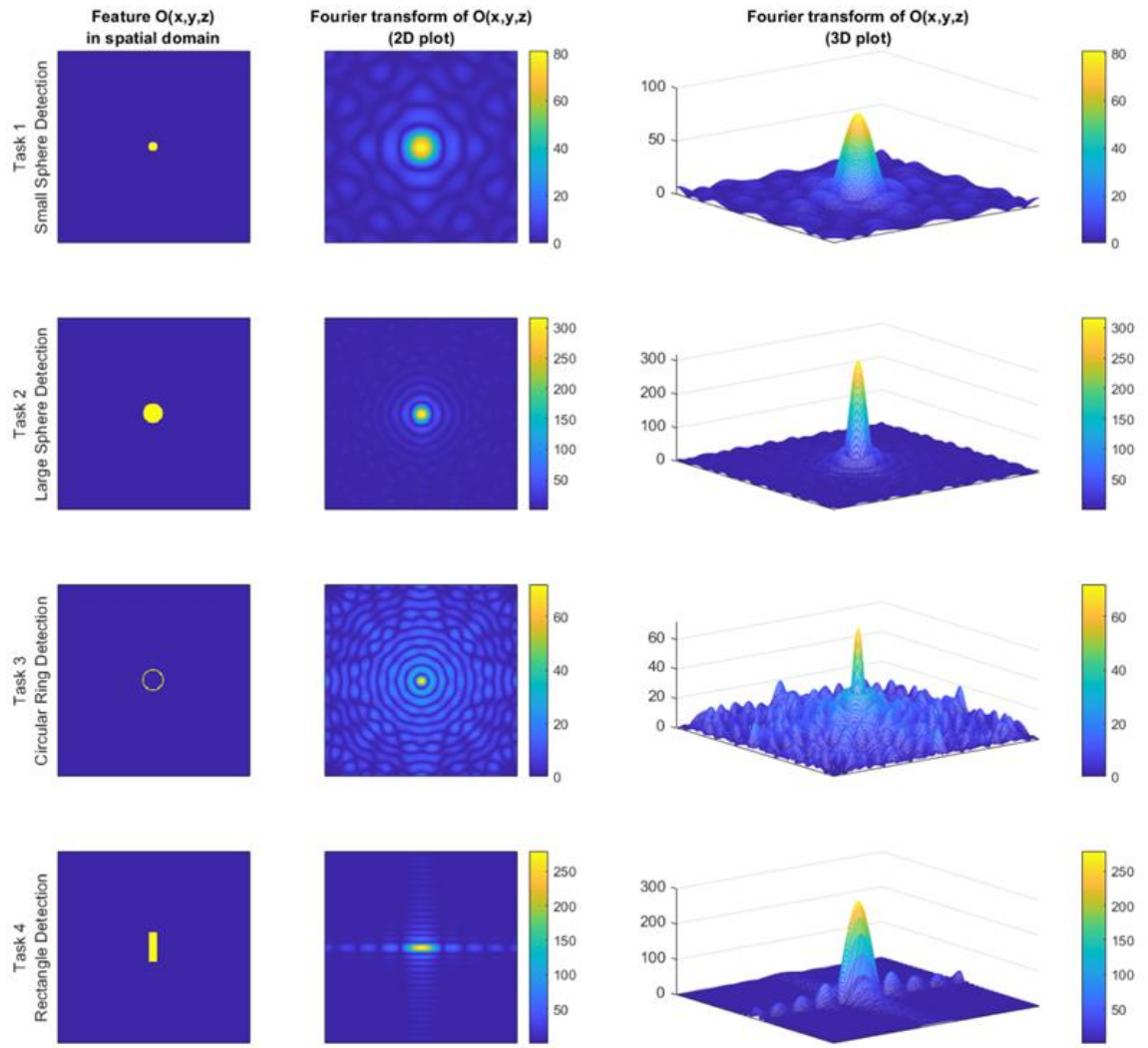


Figure 5.3: Different task functions presented in spatial (first column) and frequency domain (second and third columns). The value bars have no unit, like the features too

For special cases, where the edge profile of the feature matters and not the content, the discrete Laplace operator can be used prior to the Fourier transform. The new task function is then given as [Samei et al. 2018]:

$$W_{Task} = C \cdot \mathcal{F}\{\nabla^2[O(x, y, z)]\} \quad (5.75)$$

Where,

$$\nabla = \left(\frac{\partial O}{\partial x} + \frac{\partial O}{\partial y} + \frac{\partial O}{\partial z} \right) \quad (5.76)$$

The factor C adjusts the magnitude of the task function, so that the integral of the task function in the frequency domain equals the integral of the task function in spatial domain. Figure 5.4 represent the task function for the edge profile of a circle.

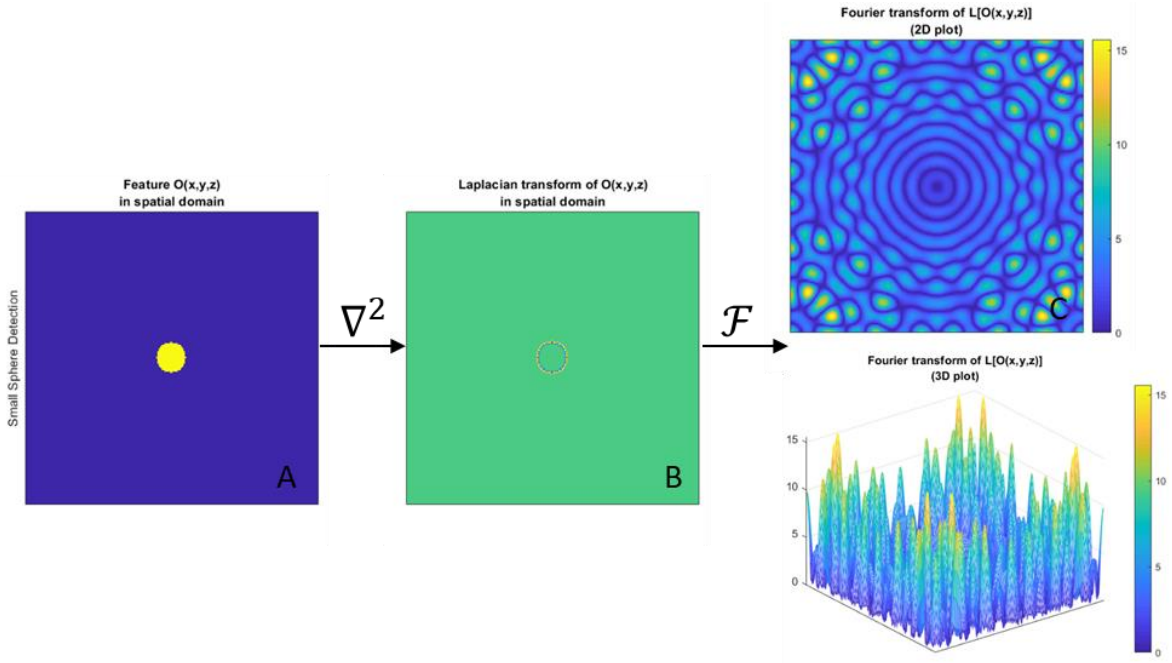


Figure 5.4: Use of the discrete Laplace operator to model the edge profile of the feature. (A) The circle in spatial domain. (B) The edge profile differentiated by the Laplace operator. (C) The task function of the edge profile of the circle in frequency domain

5.6.3 Eye Filter E

Model observers which are supposed to imitate the performance of human observer could be valuable in assessing image quality. For this purpose, a spatial frequency filter is used to correct the detectability according to the performance of the human eye. This filter represents a mathematical approximation of the human contrast sensitivity function (CSF) in relation to the spatial frequency [Gang et al. 2011].

The human CSF describes the ability to perceive changes of contrast between regions that are not separated by definite borders and can be presented as a curve of the spatial frequency as illustrated in Figure 5.5. The spatial frequency is given in cycles per degree. It describes how many vertical black and white stripes can be seen through an angle of 1 degree. Figure 5.6 shows the number of the cycles detected by the human eye per degree. Due to the limited number of photoreceptors in human eye, the detection of high spatial frequencies is very difficult and beyond a certain value is no longer possible [Archibald et al. 2009].

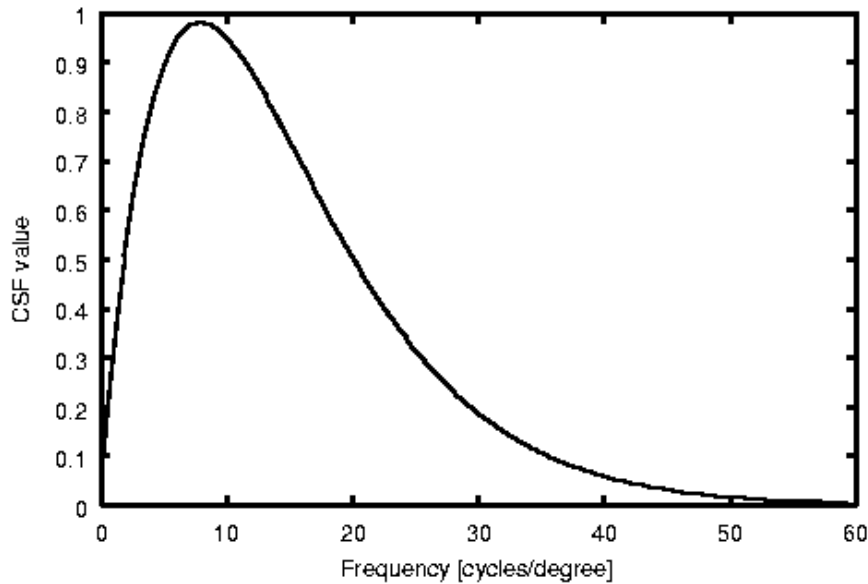


Figure 5.5: The Human Contrast Sensitivity Function. It has a peak at approximately $f = 1$ to 8 [Archibald et al. 2009]

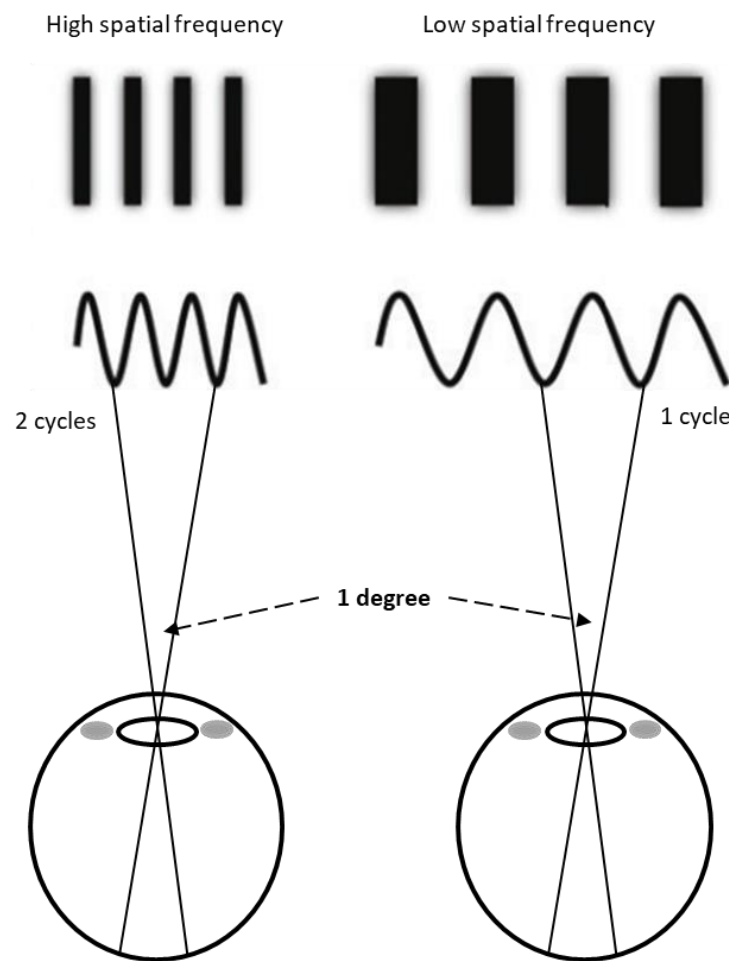


Figure 5.6: The spatial frequency defines the number of cycles seen at the eye per 1 degree. Adopted from [Archibald et al. 2009]

One possible filter defined in the frequency domain is the eye filter, for which several formulations have been cited in the literature. In this work, we will consider two eye filters that have proven their applicability in earlier works [Bouwman et al. 2014].

Eye Filter 1:

In combination with their work on the NPWE model, Burgess et al. have demonstrated that the CSF of the human eye can be expressed mathematically and proposed the following equation [Burgess et al. 1997]:

$$E(f) = f^{1.3} \cdot e^{-bf^2} \quad (5.77)$$

where, f is the spatial radial frequency (cycles/degree). The parameter b is so chosen that the maximum response of the eye filter occurs at $f = 4$ cycles/degree. For a typical viewing distance of 50 cm, b equals 2.2.

Eye Filter 2:

Based on a simple approximation of the Barten's contrast sensitivity curve of the human eye, Burgess has also suggested a second eye filter [Bouwman et al. 2014]:

$$E(f) = f \cdot e^{-bf} \quad (5.78)$$

Like the first eye filter, b is also chosen here to obtain E_{max} at $f = 4$ cycles/degree

5.6.4 Internal Noise N

In this work, it is assumed that the internal noise is uncorrelated. It is defined as a 0.01-fraction of the DC component of the noise power spectrum at a viewing distance of 100 cm [Li et al. 2013].

$$N_i = 0.01 \left(\frac{D}{100} \right)^2 NPS(0,0) \quad (5.79)$$

Where, the viewing distance D is set to be 50 cm.

$NPS(0,0)$ represents the amplitude of the white noise-equivalent NPS of the background. It is also called the DC component of NPS and is given by:

$$NPS(0,0) = \frac{\iint NPS df_x df_y}{\iint df_x df_y} \quad (5.80)$$

Compared with the total NPS, the internal noise N_i has a small magnitude. Its effect over the performance of the model observer is insignificant.

6 Methods

This chapter describes the approach and methods for implementing the Optimization algorithm. For this purpose, we will present the performed experiments to compare the performance of the model observers. These are divided into two main categories according to the dimensional representation of the feature.

The first implementation of a task-based trajectory design was demonstrated on a clinical C-arm system in 2013. A team from the Johns Hopkins University in Baltimore has defined a general framework for the optimization of the acquisition parameters. In this context, Stayman et al. have developed a task-based algorithm for optimizing the source-detector-trajectory for intraoperative operations [Stayman et al. 2013]. A first attempt to transfer this procedure into an industrial application took place in 2014 at Siemens Corporate Technology by Fisher et al. [Fischer et al. 2016]. However, both used the NPW model observer to determine the detectability index. This simple numerical observer delivers good agreement with human observers, especially for simple imaging tasks [Stayman et al. 2013].

6.1 Trajectory Optimization for 3D features

6.1.1 Flowchart of the task-based 3D detectability index

The task-based trajectory optimization algorithm developed in this work consists of five main modules: Object module, Simulation module, Optimization module, Reconstruction module, and Evaluation module. Figure 6.1 shows the flowchart of this algorithm for 3D features. In the following sections, we will discuss each module in more detail.

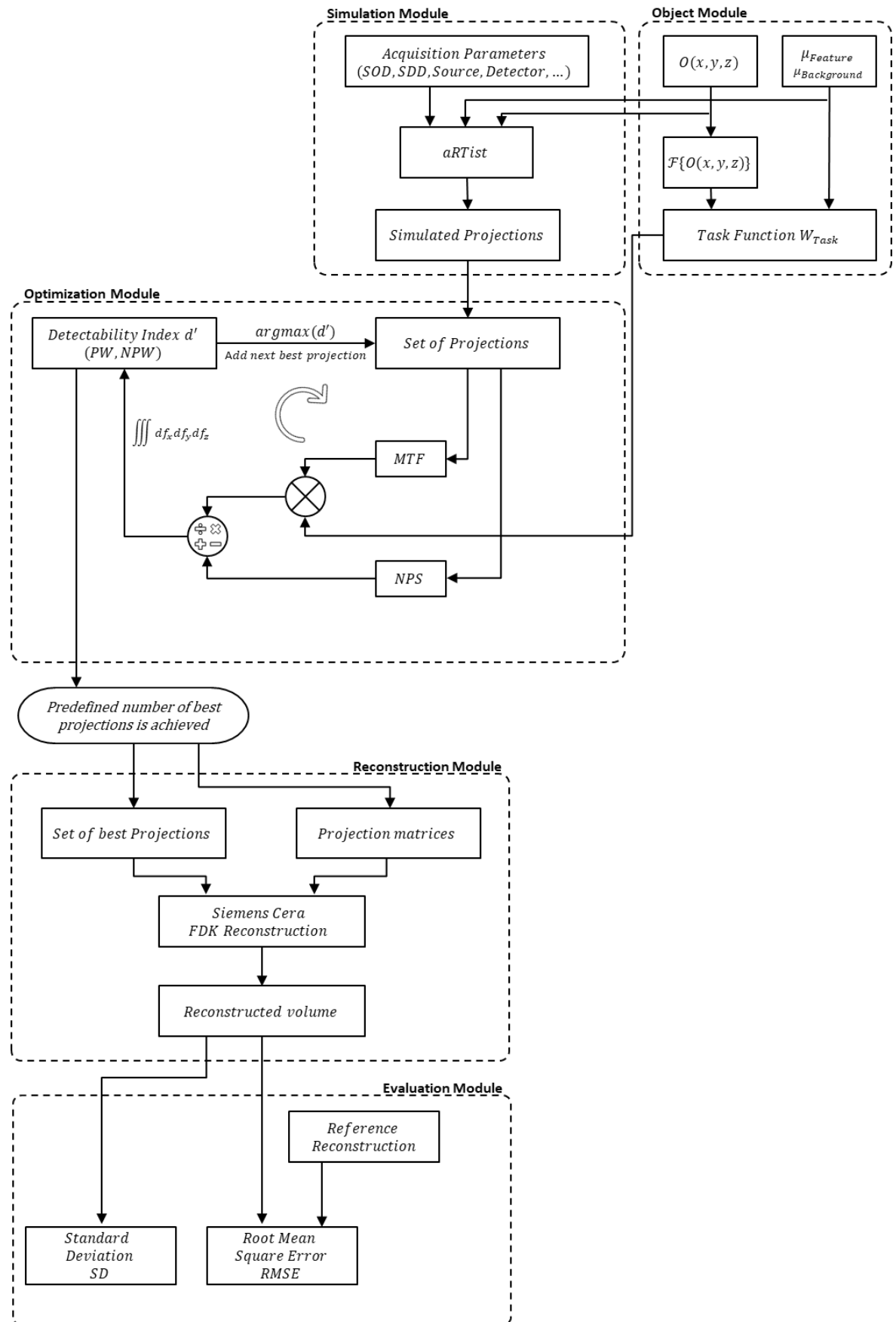


Figure 6.1: Flowchart of the task-driven trajectory optimization for 3D features

6.1.2 Object module

To determine the task function (e.g. feature is a nodule), Stayman et al. used a scan prior to the intraoperative operation. This is necessary since shape, location and attenuation coefficient of the feature are patient-dependent [Stayman et al. 2013].

On the other side, Fisher et al. have defined the task function directly in the frequency domain. For strongly directed features like edges, is this approach legible, as the Fourier transform of a line has a line shape in the Fourier domain. However, for further features, they set the task function to be equal to 1 [Fischer et al. 2016]. Doing so, the detectability index e.g. for the PW model observer becomes:

$$d'^2_{PW,3D} = \iiint \frac{(MTF)^2}{NPS} df_x df_y df_z \quad (6.1)$$

In this case the detectability index considers only projections that deliver a good resolution (MTF) with a little noise (NPS) without incorporating the properties of the feature. As demonstrated in Section 5.6.1, MTF and NPS are locally dependent. This means the optimization is done for a high Signal-to-Noise Ratio (SNR) on the feature location specified by the feature vector e . Instead, we use the presence of a CAD model to define the imaging task functions. As a phantom, we modified an existing object as shown in Figure 6.2, which was used in an earlier study [Krimmel 2006]. As features, we positioned a sphere and a cylinder in two different positions within the phantom. However, the trajectory optimization will be performed separately for each feature. A design drawing is shown in Appendix A.

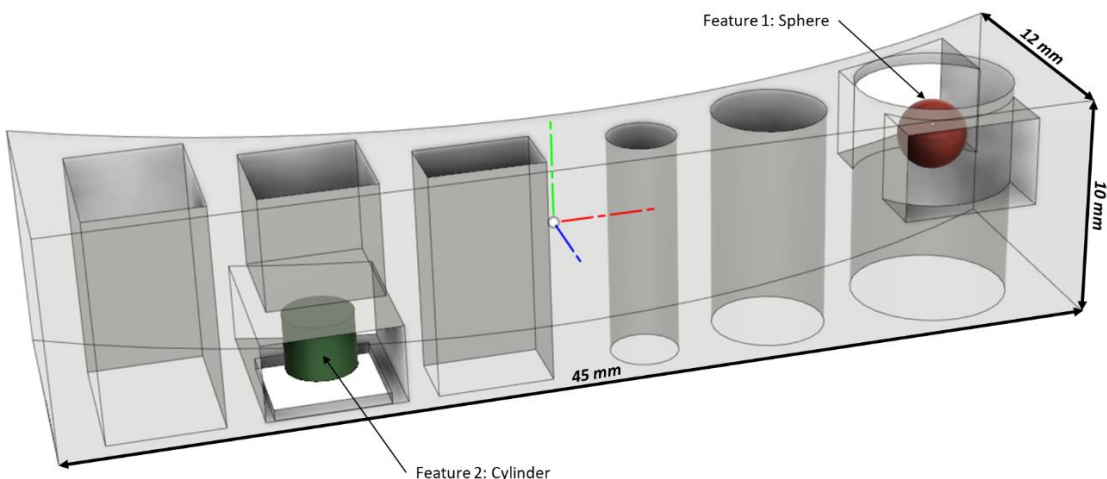


Figure 6.2: A customized phantom used to characterize the performance of the model observer

The sphere is of 3.1 mm diameter and is made of steel (Fe). The cylinder is made of titanium (Ti) and has a diameter of 3.1 mm and a height of 2.5 mm. The remaining body of the phantom is made of steel and has the following dimensions: 45 x 12 x 10 mm.

The different choice of material for both features has the advantage that we can test the model observers on two different contrast levels. Then for the configuration established in this work (will be introduced in the simulation module), steel and titanium have the following attenuation coefficients: 1.5433 cm^{-1} for steel and only 0.742 cm^{-1} for titanium. This allows us to examine the performance of the model observers for both high- and low-contrast detection.

As shown above in Figure 6.2, the detection of the features is performed against the air as a background and the definition of the task function simplifies to:

$$W_{Task} = \mu_{Feature} \cdot \mathcal{F}\{O(x, y, z)\} \quad (6.2)$$

The value of $\mu_{Feature}$ will be taken from a reconstruction of the phantom with 2000 projections.

6.1.3 Simulation module

To generate the CT projection data, we used the radiographic simulation tool, aRTist (Analytical RT Inspection Simulation Tool), which is graphically displayed in Figure 6.3. This tool has been developed by the Bundesanstalt für Materialforschung und -prüfung (BAM). The CAD file in STL format of the phantom can be loaded and the corresponding materials (attenuation coefficients) can be assigned. This software allows the simulation of arbitrary trajectories. The generation of the X-ray images is based on X-ray tracing algorithms. The influence of scattering can be additionally simulated by a Monte-Carlo tool and a noise factor for the detector can also be set [Schrapp 2015].

In this work, the X-ray tube current was fixed at 250 kV. The dataset was generated with a 360-degree field-of-view and a total of 360 equidistant distributed projections over a circular orbit (1° angle step). The acquisition time of a single projection was 0.5 s. The detector has a resolution of (512 x 512) and a noise factor of 1 %. For a good image quality, we selected a pixel pitch of 0.2 mm. The SOD and SDD are chosen as 100 and 200 mm, respectively. The object to be X-rayed is modeled with (512 x 512 x 512) voxels and the edge length of each voxel is set to 0.1 mm.

For a reference reconstruction required in the evaluation module, 2000 angularly equidistant projections are recorded under the same geometry configuration as the 360 projections intended for the optimization.

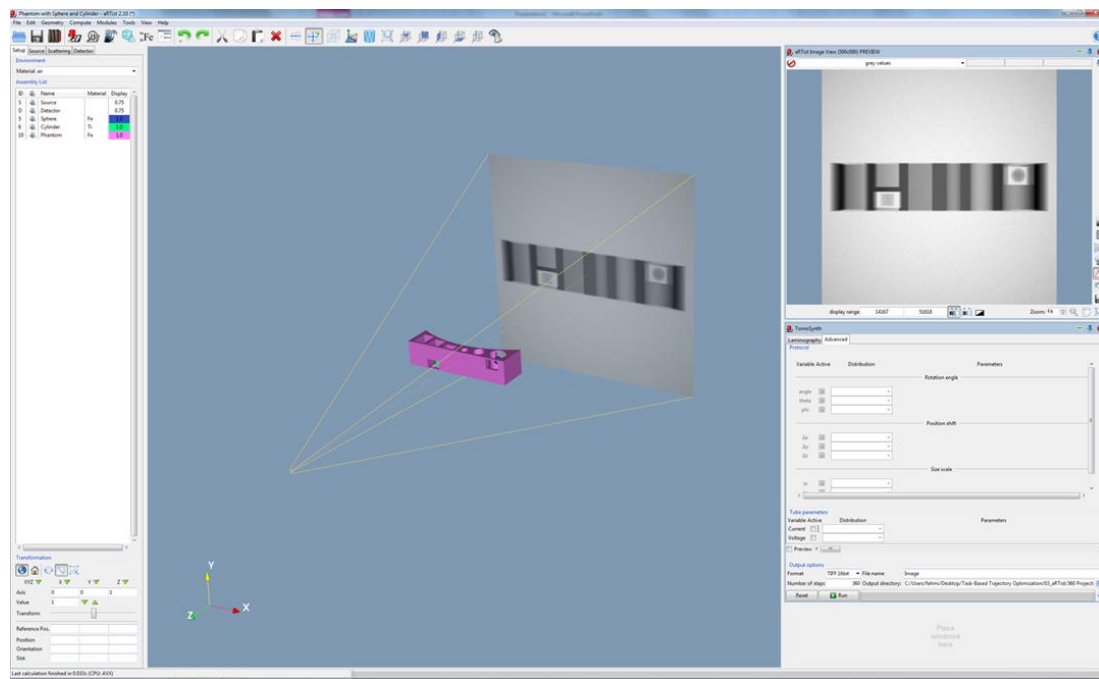


Figure 6.3: GUI of the X-ray simulation tool aRTist

The rotation axis of the object must be carefully selected to reduce the influence of artifacts. That means that it should best not coincide with the rotation axes of rotational parts like a cylinder. Otherwise, CT artifacts like the Feldkamp artifacts (streaks in the reconstruction due to the data incompleteness, also called cone beam artifacts) are enhanced by the cone-beam CT [Xue et al. 2015] [Herminso et al. 2015]. Figure 6.4 illustrates this type of artifacts for a cylinder depending on the position of the CT axis of rotation “Z” to the cylinder axis.

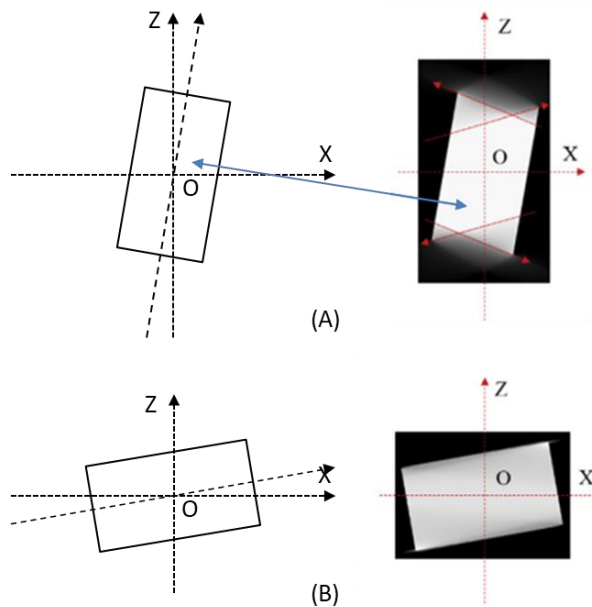


Figure 6.4: Reconstruction of a cylinder for two different inclination angles. (A) shows strong FDK artifacts. The figures are reproduced from [Xue et al. 2015]

6.1.4 Optimization module

In the work of Stayman et al., the locations of source-detector system are parameterized by a series of arc trajectories forming a sphere. Each position on the arc is defined by a tilt angle φ_n and a rotation angle θ_n . With a gradual increase of the tilt angle below a fixed rotation angle, it was then examined under which angle the detectability index d' is the highest. In total, one projection was selected for each arc orbit. The purpose of this approach is to have more angle information during the reconstruction [Stayman et al. 2013].

However, as the goal of this work is to evaluate the efficiency of the model observers, we limit the optimization to projections acquired over a simple circular orbit.

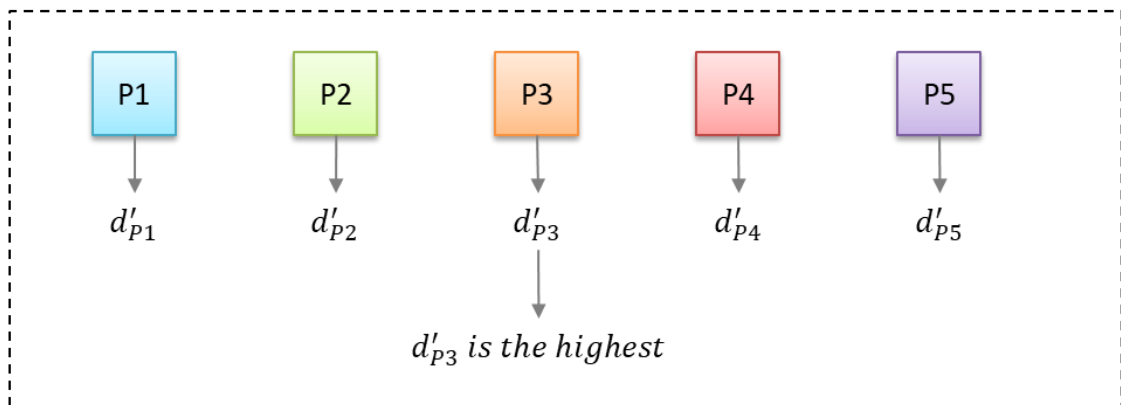
- **Greedy Algorithm**

To have the first N best projections from the 360 acquired projections, the general optimization task requires computing the detectability index for all possible combinations of N angles. This would require $\prod_{k=0}^{N-1} (360 - k)$ iterations. If N is equal 18, then we would need 6.6958e+45 iterations. However, this is computationally extremely expensive to perform. To avoid this limitation, Stayman et al. applied a greedy algorithm [Stayman et al. 2013]. In this context, the detectability index servers as a fitness function to identify the ideal projections. The trajectory optimization algorithm calculates iteratively the detectability index and, in each iteration, the next best projection with the highest detectability index is chosen. This projection is then added to the growing set of ideal projections.

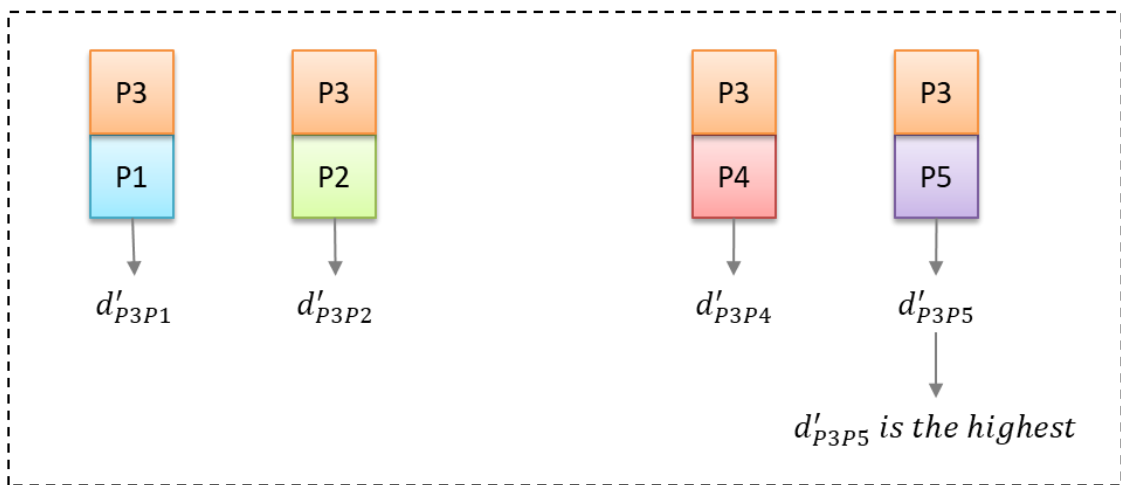
To illustrate this approach, we show an example in Figure 6.5 with a set of 5 projections with the goal to find the best first 3 projections. In the first iteration, the set of ideal projections is empty. The detectability index d' is calculated for each individual projection. In our example, the third projection has the highest detectability index and therefore will be added to the set of ideal projections. In the second iteration, the already selected third projection will be added to each of the remaining projections and the detectability index is recalculated. In this iteration, the system matrix A contains two projections (see section 2.3). After each iteration, its size increases by one more projection.

In this study, we will optimize the acquisition trajectory for different number of ideal projections with $N \in \{8, 18, 24, 36, 72, 90, 120\}$.

1. Iteration



2. Iteration



3. Iteration

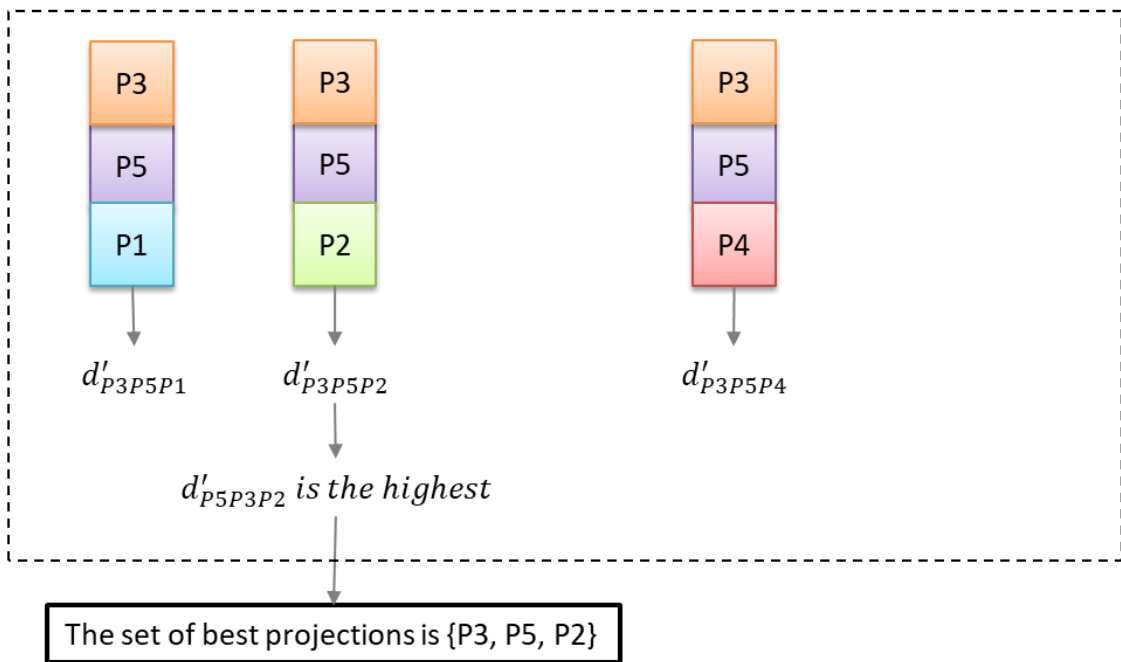


Figure 6.5: A greedy algorithm is used as an optimization algorithm to find out the set of ideal projections

Weighting Map:

A weighting map is applied to reduce the detectability index of the projections near the already selected projections. This procedure helps to have more angle information about the feature, since adjacent projections to already chosen ones are less likely to be selected. As a weighting term, we selected a factor of 0.5. Furthermore, the number of projections to be weighted is dynamically selected depending on the desired number of ideal projections as follows:

$$N_{Right/Left} = \frac{1}{2} \cdot \frac{\text{Number of total projections}}{\text{Number of desired ideal projections}} \quad (6.3)$$

- Model Observers

Table 6-1 contains the expressions for the detectability index in spatial and Fourier domain for the two 3D model observers PW (see section 5.1) and NPW (see section 5.2).

Table 6-1: Detectability Index for various 3D model observer

Observer	d'^2_{3D} (Spatial)	d'^2_{3D} (Fourier)
PW MO	$(g \mu_f)^T C_n^{-1} (g \mu_f)$	$\iiint \frac{(MTF \cdot W_{Task})^2}{NPS} df_x df_y df_z$
NPW MO	$\frac{[(g \mu_f)^T (g \mu_f)]^2}{(g \mu_f)^T C_n (g \mu_f)}$	$\frac{[\iiint (MTF \cdot W_{Task})^2 df_x df_y df_z]^2}{\iiint NPS \cdot (MTF \cdot W_{Task})^2 df_x df_y df_z}$

For the calculation of local MTF and NPS, we will use the Fessler's predictors introduced in equations (5.71) and (5.72). For illustration, we write them again in the following table compared with their measurement formulas.

Table 6-2: Measurement and prediction formulas for MTF and NPS

	Measurement	Prediction
MTF	$ \mathcal{F}\{PSF(x, y)\} $	$\frac{ \mathcal{F}\{A^T D\{y\} A e_j\} }{ \mathcal{F}\{A^T D\{y\} A e_j + \beta R e_j\} }$
NPS	$\frac{\Delta x \Delta y}{L_x L_y} \frac{1}{N} \sum_{i=1}^N \mathcal{F}\{ROI_i(x, y) - \overline{ROI}_i\} ^2$	$\frac{ \mathcal{F}\{A^T D\{y\} A e_j\} }{ \mathcal{F}\{A^T D\{y\} A e_j + \beta R e_j\} ^2}$

Regularization:

The regularization strength parameter β in MTF and NPS will be considered as constant, as this is eligible in most cases [Stayman et al. 2013]. In this work, we set $\beta = 10^5$. However, it has to be selected carefully, as it affects considerably the spatial resolution and the amount of noise in CT images. Figure 6.6 shows examples of the reconstruction of a low-contrast sphere for varying values of β .

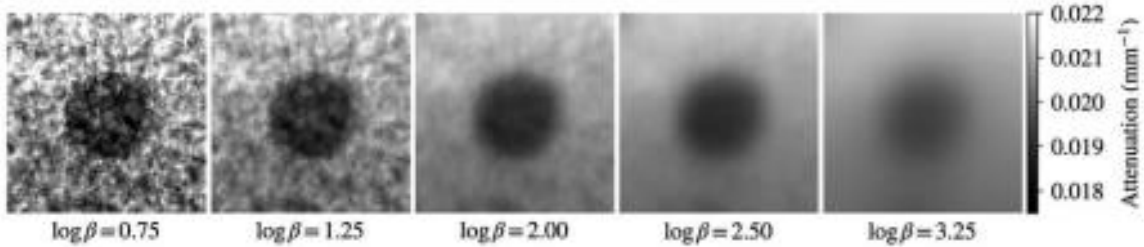


Figure 6.6: Example of a reconstruction of a low-contrast sphere for varying values of β [Uneri et al. 2018]

Fisher Information Matrix:

The calculations of MTF and NPS depend on the evaluation of the term,

$$FIM = \mathbf{A}^T \mathbf{D}\{y\} \mathbf{A} \quad (6.4)$$

This term is referred to as the Fisher Information Matrix (FIM). By multiplying it with the location vector e_j , the column corresponding to the voxel j is extracted. However, an explicit determination of FIM and then extracting the j -th column, is computationally very difficult due to the huge size of the system matrix \mathbf{A} . In his trajectory optimization algorithm, Stayman used one of the approximations formulated by him and Fessler earlier [Stayman et al. 2013]. These approximations deliver accurate results and requires less computation time [Stayman et al. 2004]. But since they are approximations by nature, we use a different approach here to get the accurate results. These steps are listed in the following scheme:

1. Create a volume where the voxel representing the feature location is set to 1. This corresponds to the unit vector e . $\rightarrow e_j$
2. Generate simulated projections of this volume using the system matrix \mathbf{A} (illustrated in section 2.3). This step is also called forward projection. Here a pre-programmed Forward-Projector of the commercially available reconstruction framework CERA will be applied [Siemens 2016]. $\rightarrow \mathbf{A}e_j$
3. Weight the generated projections with the acquired projections. $\rightarrow \mathbf{D}\{y\} \mathbf{A}e_j$

4. The weighted projections are then back-projected using the transpose of the system matrix \mathbf{A} . This step is a part of the FDK reconstruction and has been explained in section 3.2. $\Rightarrow \mathbf{A}^T \mathbf{D}\{y\} \mathbf{A} e_j$

- **Speed-Up Computation**

Since MTF and NPS must be evaluated for each set of projections in each iteration (Total of 6480 ($=360*18$) calculations to obtain the first 18 ideal projections), different techniques can be adopted to speed up the optimization. In the optimization algorithm of Fisher et al., it took several hours for 18 iterations for a volume of size (400 x 400 x 400) voxels [Fischer 2014]. With the following approaches (similar to [Gang et al. 2016]) we reduced the computation time for 18 iterations to less than 11 minutes and evaluating the detectability index requires only 0.09 s to 0.11 s on a HP Z820 workstation with an Intel(R) Xeon(R) CPU E5-2630 0 at 2.60 GHz (2 Processors) and 256 GB of RAM:

First: For each projection i the term $(\mathbf{A}_i^T \mathbf{D}\{y_i\} \mathbf{A}_i e_j)$ will be precomputed and stored prior to the optimization algorithm. Then a summation of these terms over the considered set of projections leads to the total term $(\mathbf{A}^T \mathbf{D}\{y\} \mathbf{A} e_j)$. As can be seen, the single terms only depend of the feature position and so they can be reused and do not have to be recalculated when we examine different model observers for the same feature.

Second: The term $(\mathbf{A}_i^T \mathbf{D}\{y_i\} \mathbf{A}_i e_j)$ is an array of 0.5 GB in size for a volume size of (512 x 512 x 512) voxels. For the acquired 360 projections, we need 180 GB of memory to store the precomputing results. In addition, the size of the RAM limits the number of projections in one set. A 4 GB RAM can only add up to a maximum of 8 arrays of 0.5 GB. To avoid this problem, the individual terms are calculated only for the volume-of-interest, which is significantly smaller than the entire volume. For example, for the sphere feature, the size of an array is only 0.44 MB. Thus, only ca. 161 MB of memory is needed. This is more than 1000 times less memory need than before. In our simulations, the size of the VOI was chosen to be (49 x 49 x 49) voxels around the sphere and (49 x 49 x 31) for the cylinder.

Further acceleration measures are possible. For example, the implementation of certain functions can be parallelized and executed on the GPU.

- **Optimization for multiple features**

The Optimization module can be expanded to consider multiple features in different locations.

With each iteration a detectability index associated with every task function is determined.

The optimizer can then be written as [Ouadah et al. 2017]:

$$\underset{\Omega}{\operatorname{argmax}} \left[\min \{ d_1^2(W_{Task,1}), d_2^2(W_{Task,2}), \dots, d_L^2(W_{Task,L}) \} \right] \quad (6.5)$$

This optimizer aims to maximize the minimum detectability over L task functions. It guarantees a specific minimum detectability for all tasks. As this problem is non-convex, it can be solved by using the covariance matrix adaptation-evolution strategy (CMA-ES) algorithm [Ouadah et al. 2017].

6.1.5 Reconstruction module

- **Reconstruction Method**

The selected projections are further processed with CERA, a Siemens software package for CT reconstruction. It offers a high-speed processing using CUDA-based GPU implementation and parallel computing [Siemens 2016]. CUDA is a parallel language of Nvidia to execute code on the graphics card. As a reconstruction method, we used the filtered Backprojection technique. But we have to be aware that the estimation of MTF and NPS is based on the Penalized Likelihood algorithm and must be actually reconstructed with this method to achieve the best reconstruction quality. However, we assume that the ideal projections should also deliver good results for different reconstruction approaches.

Additional pre- and postprocessing steps enhance the quality of the reconstructed volume. Examples of these functions are [Siemens 2016]:

- Bad Pixel Correction: A detector with defective pixels results in wrong measured values. The bad pixel correction module approximates new values for these pixels according to the surrounding pixels.
- Beam Hardening Correction: This module compensates the non-linear attenuation when the X-ray passes through different material.
- Discrete Fourier Transform Filtering: This high-pass filtering step has been already presented in section 3.2. In this study we use a Shepp kernel filter. Parameters like the convolution length and scale are set automatically by CERA.

- **Projection Matrices**

To define the geometry of the acquisition trajectory, each position of the source-detector is modelled with a projection matrix. This matrix implicitly describes the relation between the voxels of the volume and the pixels of the detector for every projection. It is of dimension 3 x 4 and has 10 degrees of freedom (DoF) [Fischer 2014].

- 3 DoF, describes the position of the source
- 3 DoF, describes the orientation of the main X-ray beam
- 2 DoF, depends on the pixel length and the source-detector-distance
- 2 DoF, depends on the shift of the detector against the main X-ray beam in both directions in the detector plane

It is not to be confused with the system matrix A , which explicitly defines the contribution of each voxel to each pixel.

6.1.6 Evaluation module

The evaluation module is essential for assessing and comparing the quality of the reconstruction for different sets of projections. For this purpose, we will use the following two error metrics, which have been already presented in section 3.3:

- Standard deviation SD
- Root Mean Square Error RMSE

As reference reconstruction we use an FDK reconstruction with 2000 projections. To be able to compare the different reconstructions visually, we scale them with the identical histogram range. In this study, however, we will scale the entire reconstruction and the VOI reconstruction differently to enhance its contrast. This is useful because the feature has a different material than the phantom.

6.2 Trajectory Optimization for 2D features

6.2.1 Flowchart of the task-based 2D detectability index

The trajectory optimization algorithm presented in section 6.1.1 is extended to perform the optimization for 2D features. Mainly, we will add an observer module and extend the evaluation module to include the CHO model observers. In this work, we use the CHO observers to evaluate the results of the optimization with the PW- and NPW-based observers and not for the optimization itself. Figure 6.7 shows the flowchart of this algorithm. In the following sections, we will discuss in particular the added modules in more detail.

6.2.2 Object module

Just as for the optimization for 3D features, we also use the same phantom here. As a feature, we take the horizontal cross-sectional area of the cylinder. So, the feature is a circle with a diameter of 3.1 mm and Titanium as material. Another possibility would be to consider one of the main circles of the sphere. A square as feature can also be examined here if we use the longitudinal cross-section of the cylinder. More complicated features can also be explored. But since they are very difficult to define in binary form, they can be also extracted from a reference reconstruction. This method was implemented in the optimization algorithm in this work. The user can choose between two options (1: Binary definition, 2: Extract from the reconstruction) when defining the features. The second possibility is more general but has the disadvantage that possible reconstruction errors such as artifacts can be taken into account. The Fourier representation of a circle feature as a function of its diameter can be seen in the examples in Figure 5.3. It can be observed that, the task function of a small circle accounts high-frequency components while a large circle has primarily low and midfrequency components.

6.2.3 Simulation module

Since we have the same phantom as in the optimization for 3D features, we will use the same acquired 360 projections for the optimization.

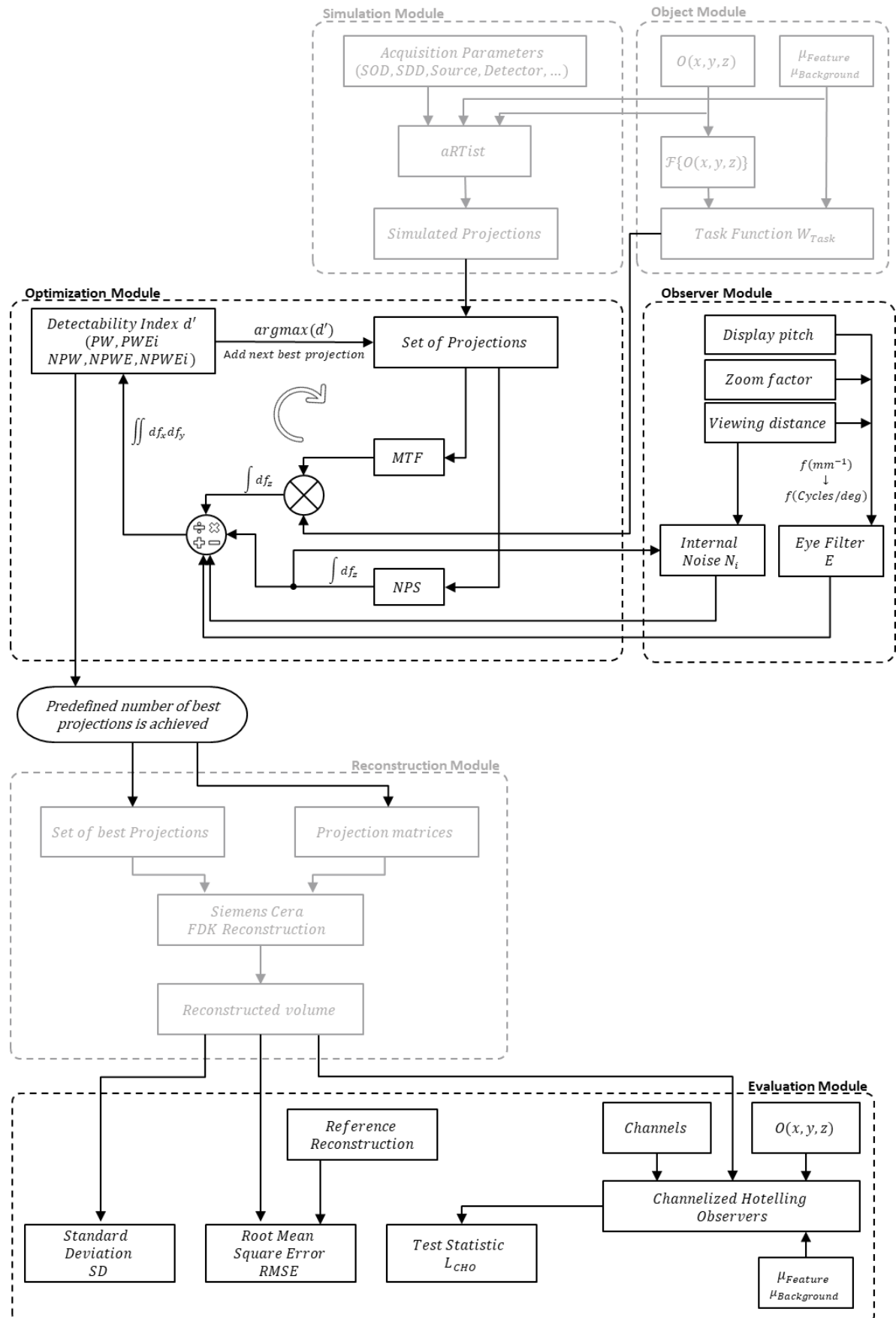


Figure 6.7: Flowchart of the task-driven trajectory optimization for 2D features

6.2.4 Observer module

One of the main differences between the optimization for 2D and 3D features is the introduction of an Observer module. For some model observers, knowledge about human perception is incorporated. Two important parameters play a role here. The contrast sensitivity function of the human eye, which is modeled by an eye filter (see section 5.6.3) and the internal noise (see section 5.6.4). We have presented two eye filters in the basics chapter. However, since they both provide similar results, we will continue to use only the filter in equation (5.78). This outcome has also been reported by Bouwman et al., when he examined the influence of multiple eye filters on the detection accuracy of a disk-shaped object [Bouwman et al. 2014]. The eye filter is expressed as a function of the angular frequency f_{deg} (cycles per degree). However, since it is multiplied by MTF, NPS and W which are represented in f_x and f_y (in the unit mm^{-1}) in the Fourier domain, it must be formulated depending on both and not of f_{deg} . Such a conversion has been represented by Zhao et al. and is [Zhao et al. 2017]:

$$f_{x,y} = f_{deg} \cdot \tan^{-1} \left(\frac{1}{d_{view}} \right) \cdot \left(\frac{a_{Display}}{a_{Image}} \lambda \right). \quad (6.6)$$

Where, d_{view} is the viewing distance in mm (distance between the human observer and the display), $a_{Display}$ is the display pixel pitch, a_{Image} is the pixel pitch of the image (corresponds to the pixel pitch of the detector), and λ is a display zoom factor. In this work, we have: $d_{view} = 50$ mm, $a_{Display} = 0.258$ mm for a display of type HP LP3065 with a resolution of 2560 x 1600 pixels, $a_{Image} = 0.1$ mm, and $\lambda = 1$.

In Figure 6.8 we show a 2D and a cross-sectional 3D view of the used eye filter. It can be seen that the filter suppresses low and high frequencies.

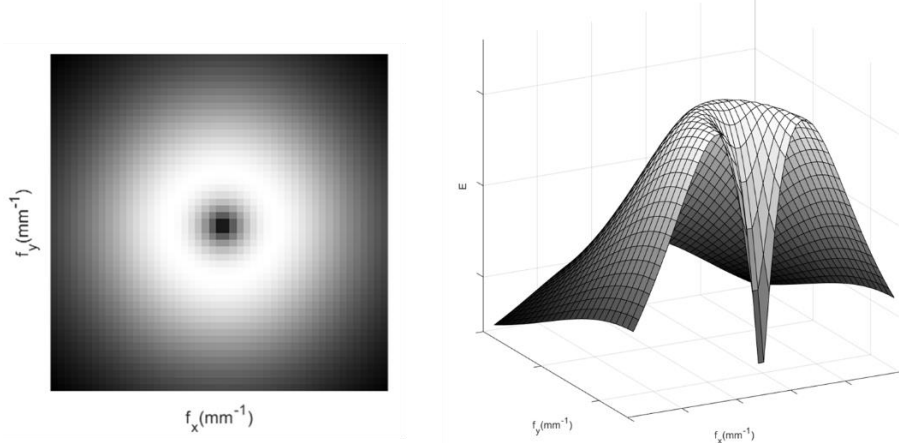


Figure 6.8: 2D and 3D visualization of the eye filter. f_x and f_y are the spatial frequencies in the x and y directions, respectively

6.2.5 Optimization module

Since a 2D feature is one pixel “thick” in z coordinate direction in reality, the optimization algorithm explained in section 6.1.4 remains unchanged.

- **Model Observers**

A summary of the 2D model observers discussed in chapter 5 is given in the Fourier domain in Table 6-3. It should be noted that the 3D MTF , NPS and W_{Task} should be integrated over the frequency direction f_z before the multiplication with the eye filter E . In general, this integration step should be performed across the direction orthogonal to the 2D image. In our case, it is the z direction.

Table 6-3: Detectability Index for various 2D model observer

Observer	d'^2_{3D} (Fourier)
PW MO	$\iint \frac{(\int MTF \cdot W_{Task} df_z)^2}{\int NPS df_z} df_x df_y$
PWE<i>i</i> MO	$\iint \frac{E^2 (\int MTF \cdot W_{Task} df_z)^2}{E^2 \int NPS df_z + N_i} df_x df_y$
NPW MO	$\frac{[\iint (\int MTF \cdot W_{Task} df_z)^2 df_x df_y]^2}{\iint (\int NPS df_z) \cdot (\int MTF \cdot W_{Task} df_z)^2 df_x df_y}$
NPWE MO	$\frac{[\iint E^2 \cdot (\int MTF \cdot W_{Task} df_z)^2 df_x df_y]^2}{\iint (E^4 \cdot \int NPS df_z) \cdot (\int MTF \cdot W_{Task} df_z)^2 df_x df_y}$
NPWE<i>i</i> MO	$\frac{[\iint E^2 \cdot (\int MTF \cdot W_{Task} df_z)^2 df_x df_y]^2}{\iint (E^4 \cdot \int NPS df_z) \cdot (\int MTF \cdot W_{Task} df_z)^2 + N_i df_x df_y}$

6.2.6 Reconstruction module

Both the reconstruction method and the reconstruction parameters are the same as for the reconstruction of the 3D features (see section 6.1.5). There are several methods in the literature to improve the quality of the reconstruction, such as incorporating prior knowledge about the object into the reconstruction [Stayman et al. 2012]. Since this is not the goal of this study, such methods are not integrated into this work.

6.2.7 Evaluation module

Besides the standard metrics SD and RMSE (see section 3.3), we will use the CHO model observers for the evaluation of the reconstruction. The aim is to calculate the detectability index of the set of projections selected by the PW- and NPW-based model observers and figure out which model they match best.

- **Channelized Hotelling Observers**

The CHO model observer computes a scalar test statistic L according to the equation (5.53). Then a decision in terms of the detection task is made in favor of the feature present hypothesis if the calculated test statistic is greater than a threshold criterion. In this work, we will rather compare the values of the calculated test statistic L for different reconstructions to each other. The highest value here means that the detectability with the corresponding set of projections is also the highest.

However, the choice of the number of channels and their parameters is very important for the results of the CHO observers. The channel selection was chosen in accordance with values from the literature. It was validated for nodule detection in medical CT and delivered good correlation with the results of a human observer [Wunderlich et al. 2008]. Below, we introduce the channels that are used in this study.

GB channels:

For the Gabor channels, we select the following parameters:

- a) 4 passbands $\left[\frac{1}{64}, \frac{1}{32}\right]$, $\left[\frac{1}{32}, \frac{1}{16}\right]$, $\left[\frac{1}{16}, \frac{1}{8}\right]$, and $\left[\frac{1}{8}, \frac{1}{4}\right]$ cycles/pixel, with 4 central frequencies $f_c = \frac{3}{128}, \frac{3}{64}, \frac{3}{32}$, and $\frac{3}{16}$ cycles/pixel and widths $\omega_s = 56.48, 28.24, 14.12$, and 7.06 pixels
- b) 5 Orientations $\theta = 0, \frac{1}{5}\pi, \frac{2}{5}\pi, \frac{3}{5}\pi, \text{ and } \frac{4}{5}\pi$
- c) 2 phase offsets $\gamma = 0, \frac{1}{2}\pi$

This makes 40 channels in total. Figure 6.9 shows the first 15 Gabor channels.

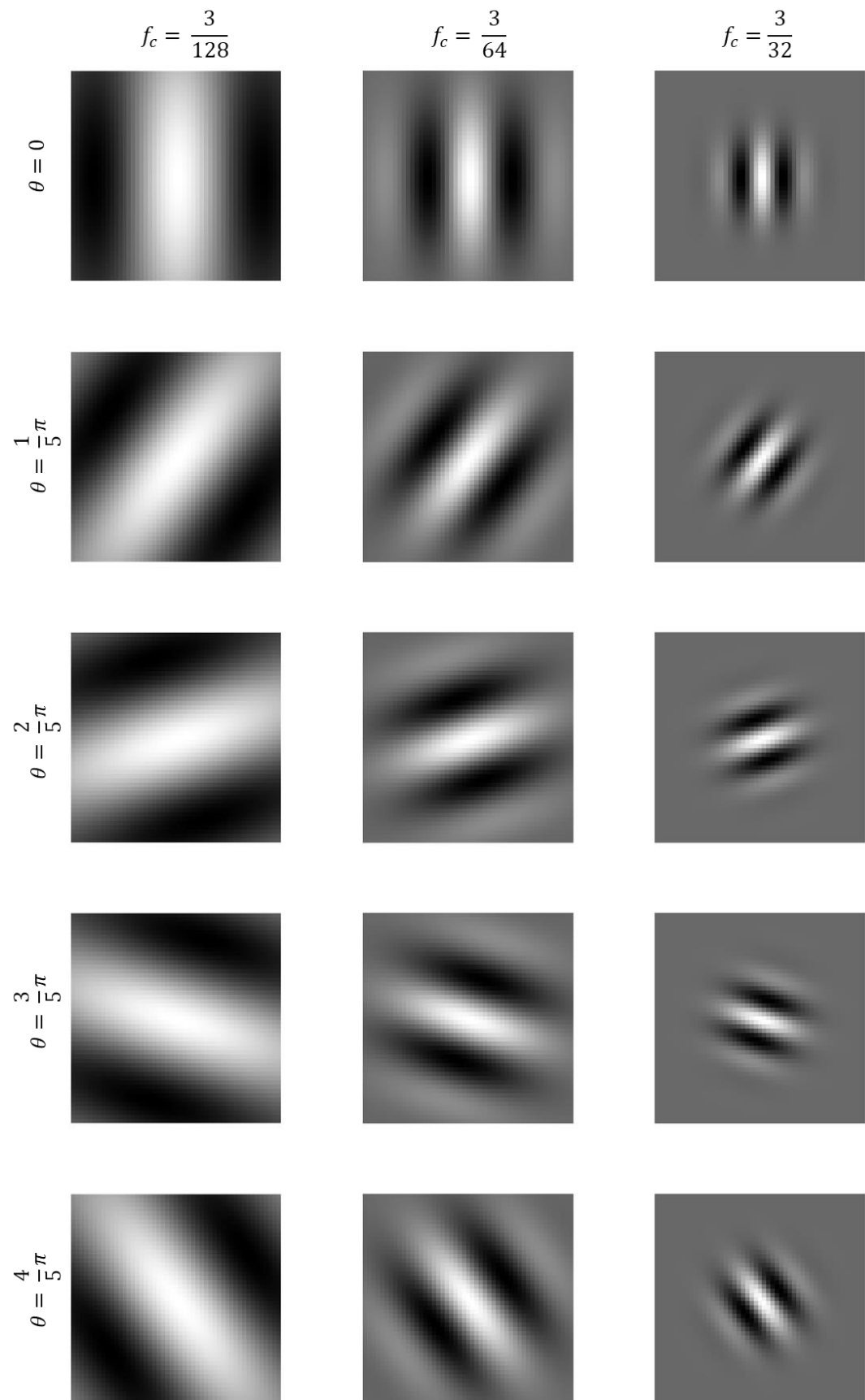


Figure 6.9: Spatial form of the first 15 Gabor channels

S-DOG and D-DOG channels:

Since all other parameters except the standard deviation σ_j are constant, only these will be modified to create new channels. A total of 3 S-DOG and 10 D-DOG channels are generated. Figure 6.10 illustrates the frequency response for the 3 S-DOG channels and the first 5 D-DOG channels.

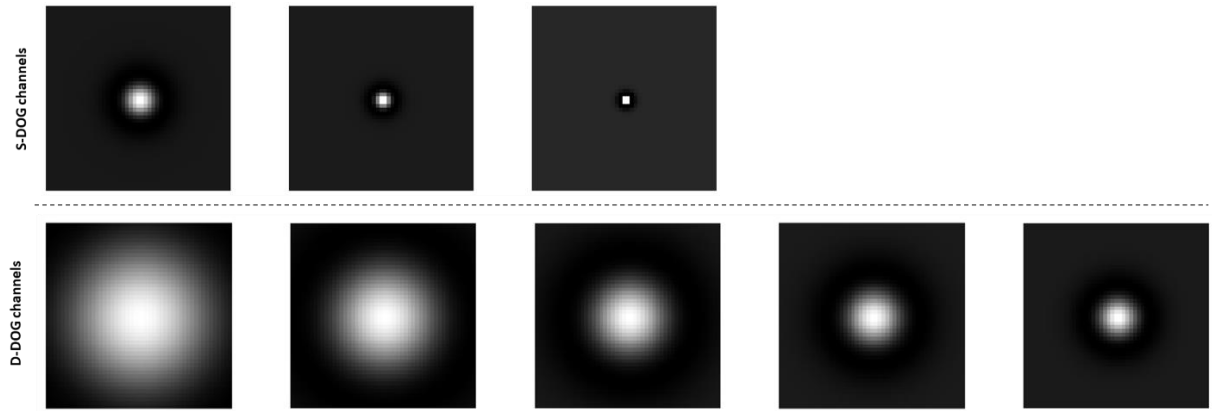


Figure 6.10: Images of the used 3 S-DOG channels and the first 5 D-DOG channels

SQR channels:

We selected 4 SQR channels with the following passbands $\left[\frac{1}{64}, \frac{1}{32}\right]$, $\left[\frac{1}{32}, \frac{1}{16}\right]$, $\left[\frac{1}{16}, \frac{1}{8}\right]$, and $\left[\frac{1}{8}, \frac{1}{4}\right]$ cycles/pixel. In order to understand the dimensionality of these channels, we also show the SQR channels in 3D in Figure 6.11.

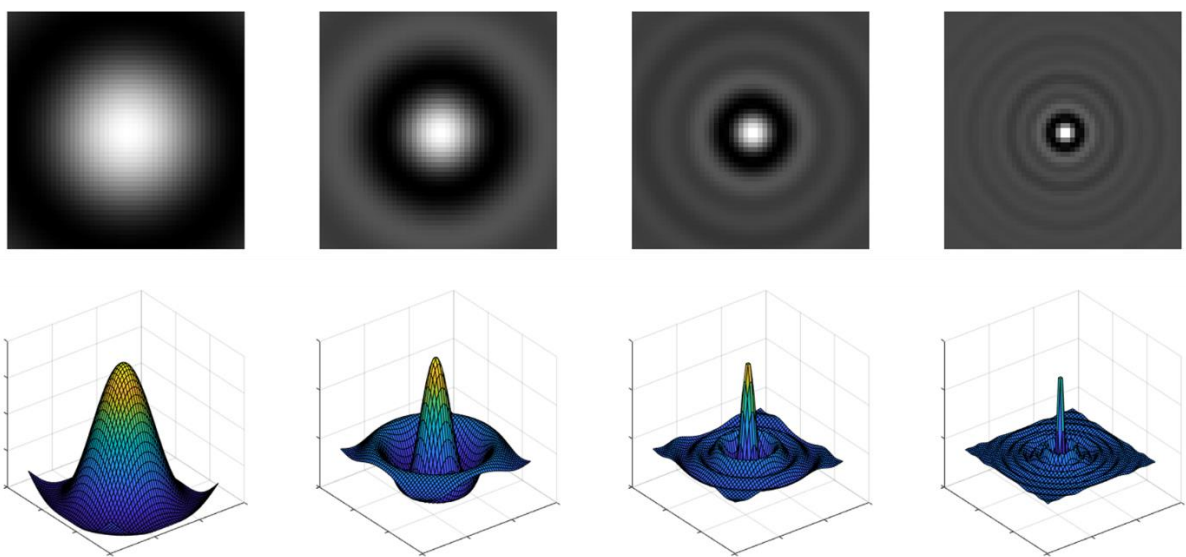


Figure 6.11: 2D and 3D representation of the used SQR channels

7 Results and Discussion

7.1 Trajectory Optimization for 3D features

This chapter presents the results of the trajectory optimization for the two 3D features (Sphere and Cylinder) and two 3D model observers (PW and NPW) presented in section 6.1. Figure 7.1 shows the arrangement of the coordinate system for each feature. This layout defines the sectional views shown later for the reconstructed volume. The origin is located in the center point of the sphere or cylinder respectively. The Z-axis of the coordinate system is defined to be in the same direction as the axis of rotation. The X-axis is defined to be perpendicular to the front view of the phantom. Then, the Y-axis is the third axis perpendicular to the XZ plane.

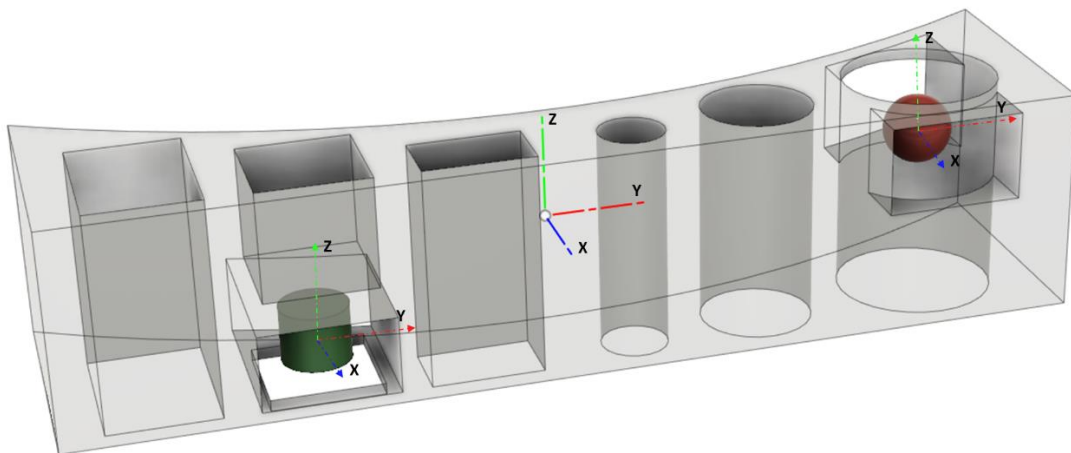


Figure 7.1: Phantom with the indicated sectional views (XY, XZ and YZ) for each feature (Sphere and Cylinder)

7.1.1 Feature 1: Sphere

For the feature “Sphere”, three different sets with 8, 24 and 90 projections are computed with equidistant distributed projections and projections selected with the proposed trajectory optimization algorithm. Their corresponding reconstruction will be compared and discussed in this section. The results with the additional sets (18, 36, 72 and 120 projections) are shown in Appendix B.

- **Trajectory optimization with a set of 8 ideal projections:**

In Figure 7.2, three reconstructions (B, C and D), based on 8 different distributed projections, are shown and compared to a reconstruction with 360 projections, which serves as a reference reconstruction. Each image shows a zoomed region (Magnification of factor 3) around the sphere in different planes. The lower images are a 3D rendering with a fixed threshold that differentiates between material and environment. This threshold is the same for all reconstructions, which is legal because the gray values were previously matched.

We clearly state that the reconstruction with the 8 projections given by the optimization algorithm (C and D) yields much better results than the reconstruction with the 8 equidistant projections (B). In each case, SD and RMSE were evaluated and listed in Table 7-1.

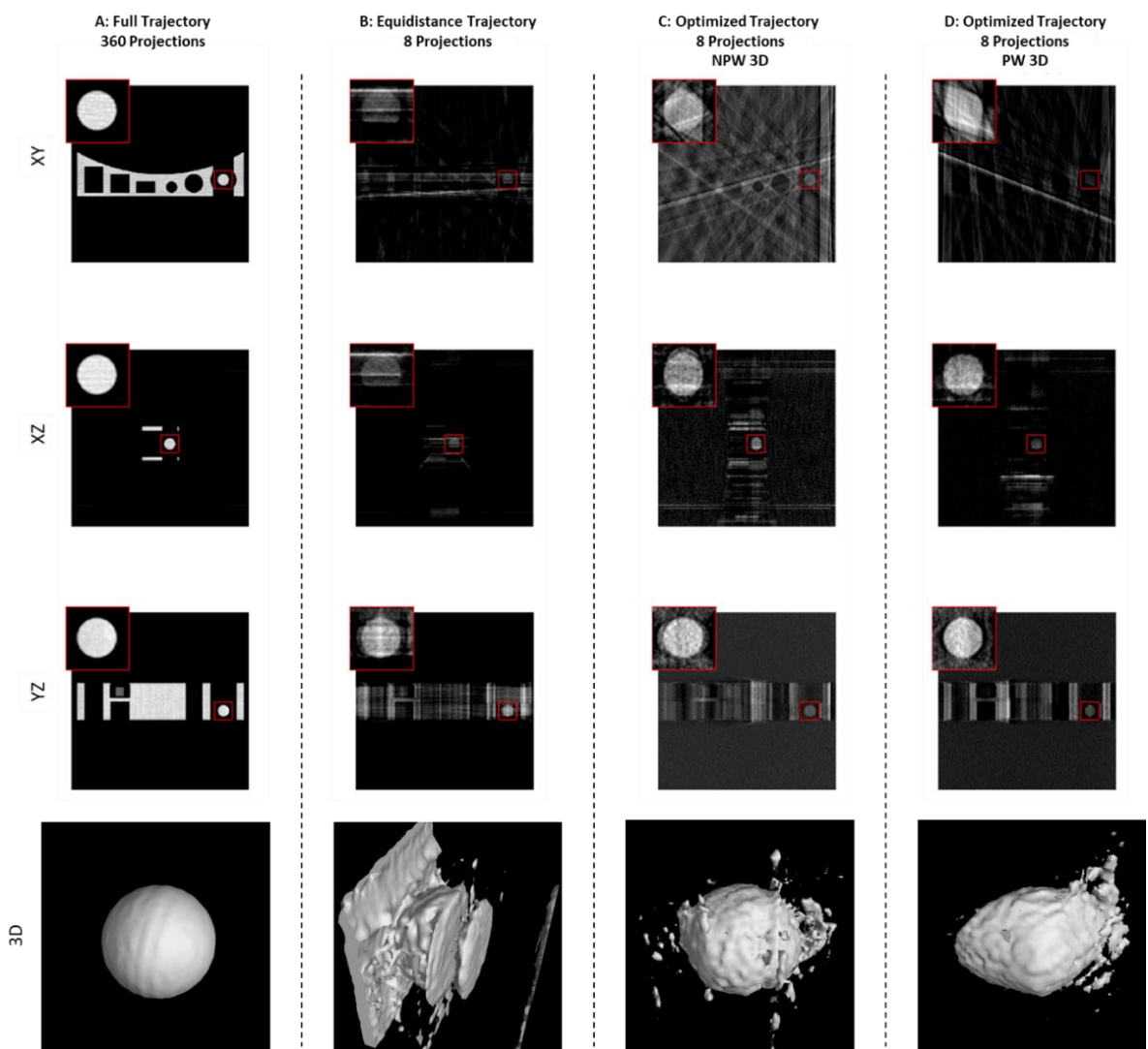


Figure 7.2: Four FDK reconstructions of the phantom with focus on the sphere are shown. A: Reference reconstruction with full angular range (360 projections). B: Reconstruction with 8 equidistant distributed projections. C and D: Reconstructions with 8 projections selected based on the NPW and PW model observers, respectively

Table 7-1: Quantitative evaluation of standard trajectories with 360 and 8 equidistant distributed projections and optimized trajectories for a set of 8 projections with NPW and PW model observers in comparison to the reference reconstruction with 2000 projections (lower values of SD and RMSE correspond to better results)

	<i>Equi 360</i>	<i>Equi 8</i>	<i>Opt 8 (NPW)</i>	<i>Opt 8 (PW)</i>
SD	0.96	4.41	1.53	1.93
RMSE	1.04	4.88	1.99	3.13

Comparing SD for the three reconstructions, we realize that the NPW- and PW-based optimization improves this metric by 65 % and 56 % respectively compared to the equidistance reconstruction.

From Figure 7.2 we see that especially in the XY and XZ planes, that the equidistance trajectory exhibits strong artifacts. This can be seen very well in the poor 3D reconstruction, since a complete half of the sphere is missing. For the PW-based reconstruction, the XY plane and the 3D representation show a strong geometrical deviation about an axis that is inclined by around 25° to the X-axis. To understand the reasons behind these deviations in the reconstruction, we display the standard and task-based optimized orbits in Figure 7.3. This figure shows also the source-detector X-rays that passes through the center of the sphere.

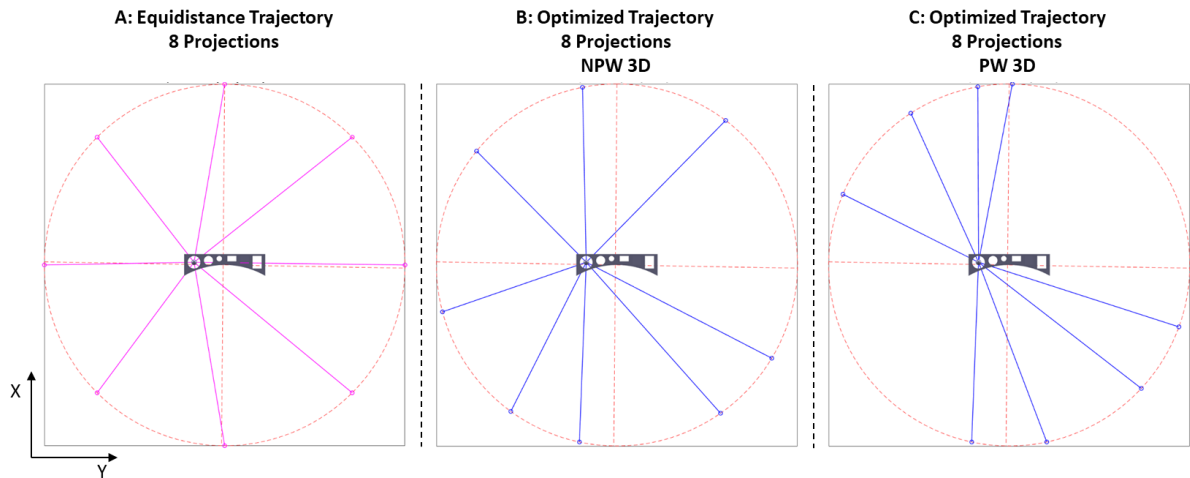


Figure 7.3: Illustration of the task-based optimized trajectories with 8 projections using the PW and NPW model observers for the feature “Sphere”

From Figure 7.3 we can clearly observe two facts:

First, we notice that projections that cause artifacts due to the lack of penetration of the phantom in Y-direction are avoided in both optimized trajectories (B and C). This optimization insight can be mathematically demonstrated as follows:

For the used phantom with edge length $l = 4.5$ cm and a linear attenuation coefficient $\mu = 1.533 \text{ cm}^{-1}$, the ideal ratio of the initial and the measured X-ray value according to the Lambert-Beer's Law along this direction is given as follows: $I/I_0 = e^{-\mu l} = e^{-4.5*1.533} = 0.001$. For the imaging system we set the noise level to 1 % which corresponds to the ratio $I/I_0 = 0.01$. This means that high-attenuation projections in the Y -direction, where scatter and noise dominate, have a very poor detectability index. These projections then have been neglected by both model observers. This lack of penetration can also be triggered by the presence of a very high-density material which causes the X-ray to be almost completely attenuated, resulting in dark zones on the projections.

Second, the optimized orbit based on the PW model observer is shown to favor only two limited angular range of views. These views are the projections with the least attenuation through the phantom at the location of the sphere. However, this limited angular range restricts the amount of information that can be gained during the reconstruction and strong artifacts like the geometric deviation are present in the final volume. In contrast, the NPW-based optimization delivers more widely distributed projections which results in more angular information. This explains why the quality of the reconstruction for the PW model observer is clearly worse compared the NPW model observer for this part.

- **Trajectory optimization with a set of 24 ideal projections:**

Figure 7.4 evaluates the reconstruction quality of the sphere over a range of 24 projections. The quantitative evaluation with SD and RMSE indicates a better performance of the NPW-based optimization ($SD = 1.44$ and $RMSE = 1.70$) as compared to an optimization with the PW model observer ($SD = 1.18$ and $RMSE = 3.49$). Identical to the optimization with 8 projections, the reconstruction with the projections selected by the PW model observer leads to geometrical deviations in the XY plane.

To demonstrate this, representations of the equidistance and optimized trajectories with a set of 24 projections are illustrated in Figure 7.5. The angular range of the projections selected by the PW model observer is similar to the results of the optimization with only 8 projections. All projections are present within two angular views. For the NPW-based optimization, we can clearly identify five angular ranges that are distributed over the entire circular orbit.

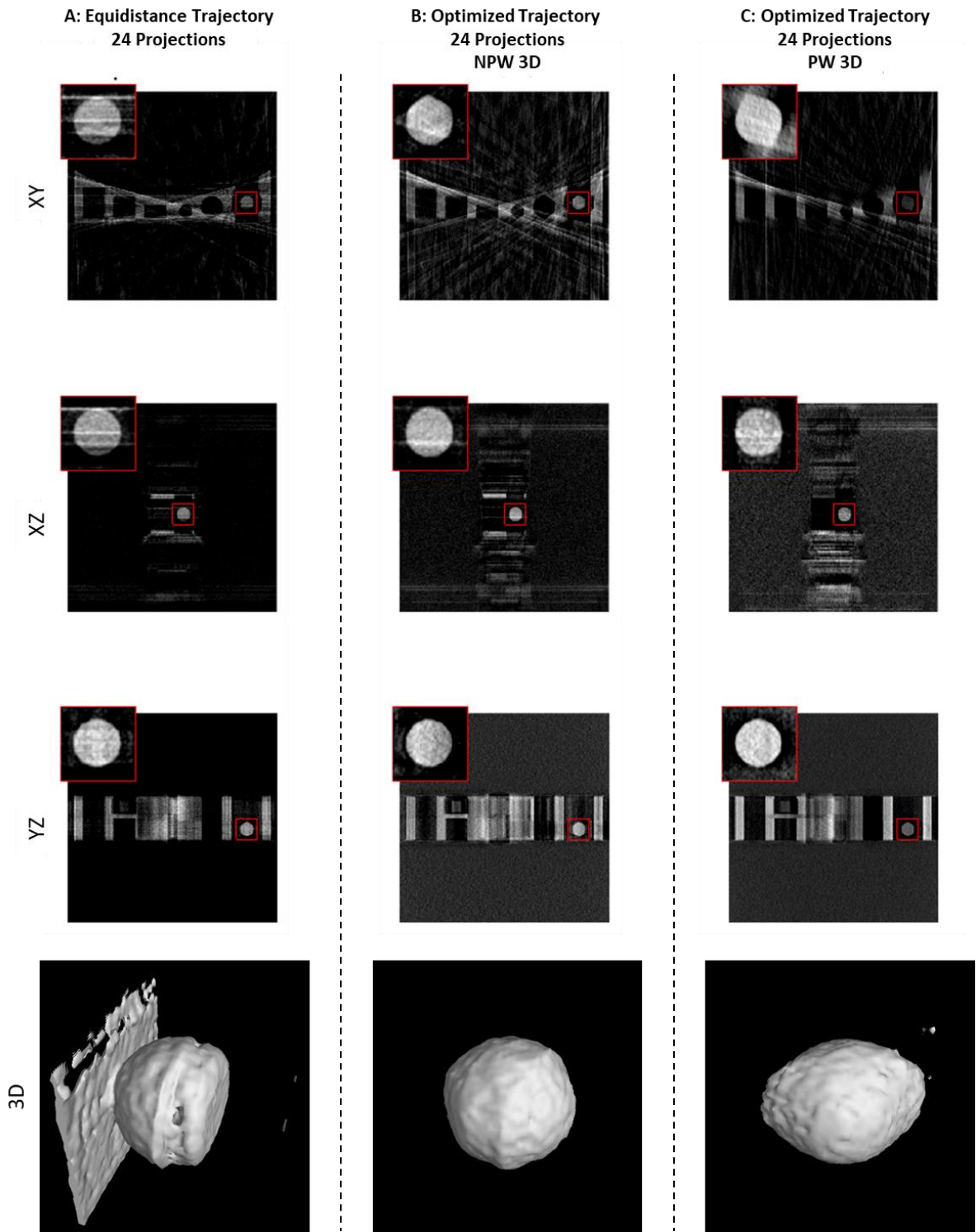


Figure 7.4: Trajectory optimization evaluated with 24 projections. As in Figure 7.2, both model observers improve the quality of the reconstruction compared with a reconstruction with 24 equidistant distributed projections

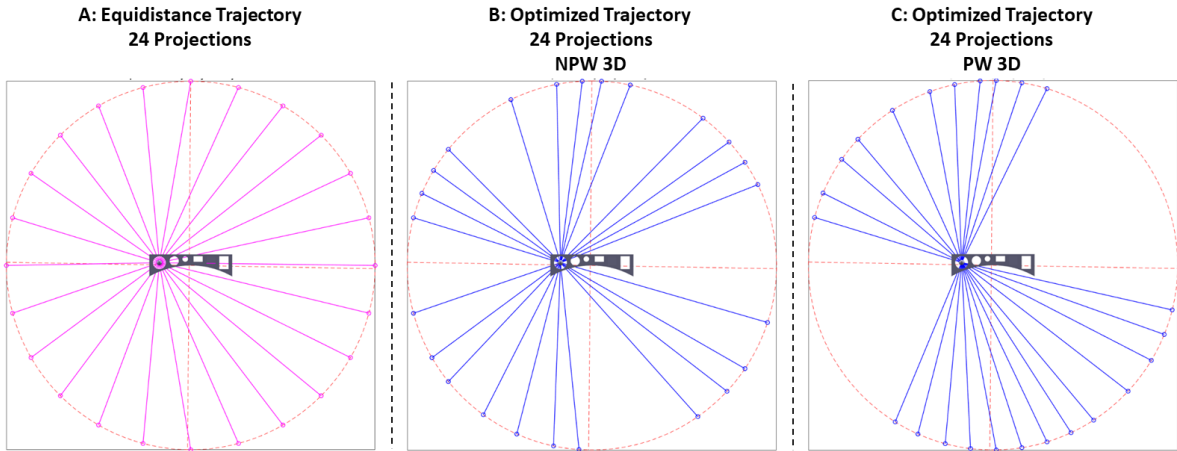


Figure 7.5: Illustration of the task-based optimized trajectories with 24 projections using the PW and NPW model observers

- **Trajectory optimization with a set of 90 ideal projections:**

Figure 7.6 qualitatively shows that in this case the PW model observer ($SD = 1.00$) outperforms the NPW model observer ($SD = 1.30$) and the uniform circular orbit ($SD = 1.34$) for a set of 90 selected projections. For optimization with a low number of projections, the NPW model observer has delivered better results. For a higher number however, the quality of the reconstruction based on the PW model observer optimization is better. This has also been confirmed for the set of 120 projections, where SD was 1.27 and 1.02 respectively for NPW and PW (see reconstructions in Appendix C.4). Comparing with $SD = 1.25$ for a trajectory with 90 uniformly distributed projections, the PW model observer has enhanced the quality of the reconstruction with 18 % while the NPW model observer achieved no visible improvement.

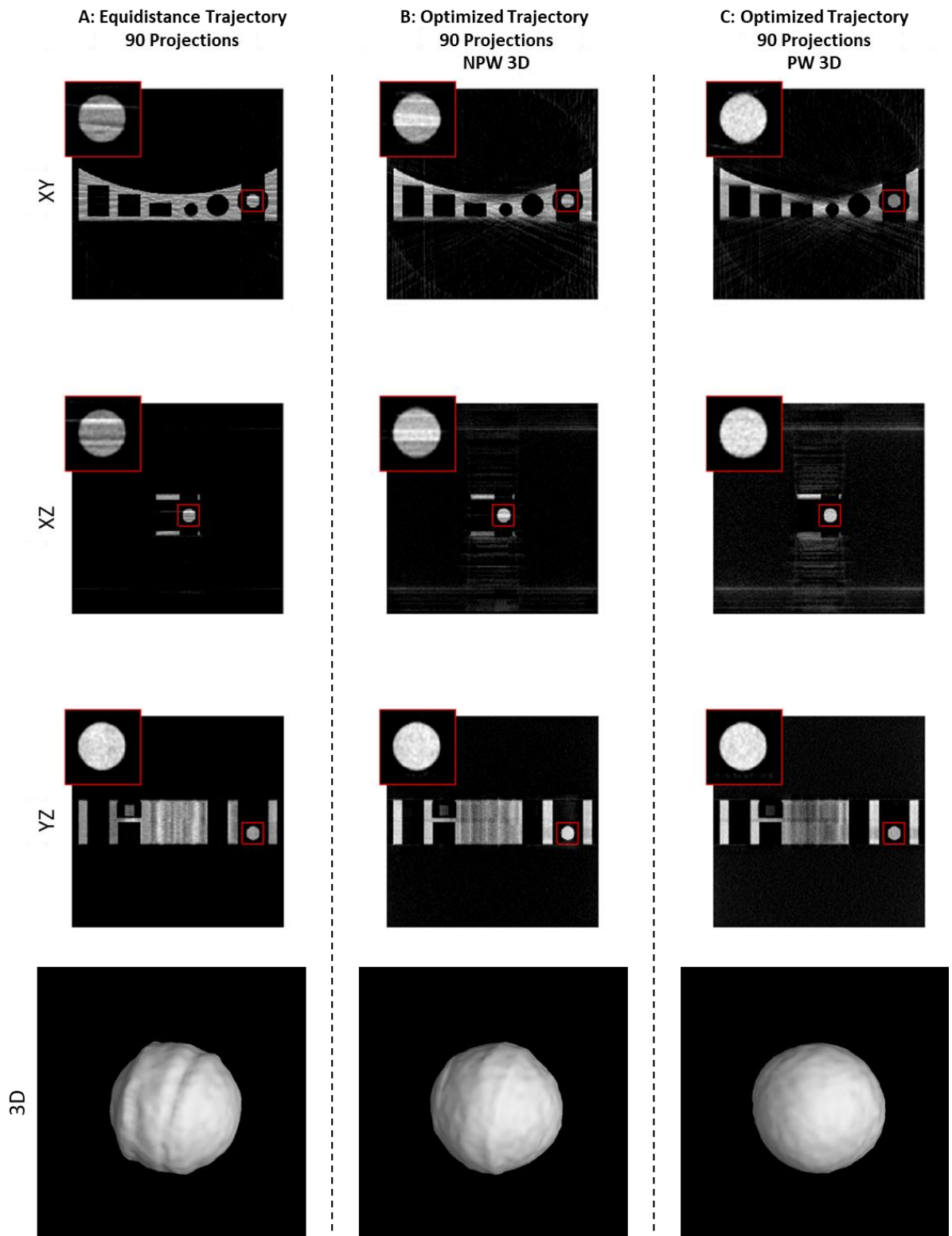


Figure 7.6: Trajectory optimization evaluated with 90 projections. For a high number of projections, the PW model observer improves the quality of the reconstruction better than the NPW model observer. The equidistance trajectory still shows some artifacts

Another way to compare both model observers is to look at their results after each iteration. Since the detectability index increases after each iteration, we show in Figure 7.7, the values normalized to 1. Here we display the calculated detectability index after each iteration until the 10-th iteration for an optimization with the NPW (left) and PW (right) model observers. The dotted blue line shows the projection chosen in this iteration. The angle of this projection is given on the X-axis, which ranges up to 360°.

Progress of the NPW detectability index:

In the first iteration, the NPW model observer shows two very narrow areas with two peaks very well. These two areas refer to the projections that look directly at the sphere and separate it from the phantom. At these two positions, the X-ray passes through the sphere without the phantom attenuating it. These two projections are then chosen during the first and second iterations. Until the 10-th iteration, a differentiability between the calculated values of the detectability index of the associated projections can be observed very well. The next ideal projection increases the detectability index so that it is recognizable.

Progress of the PW detectability index:

In contrast, the PW model observer shows a different behavior. In the first iteration, two areas with two minima are more visible. These correspond to the projections in the Y-direction and are therefore avoided. After each iteration, the difference between favorable and poor projections becomes smaller. After the 10-th iteration, this differentiability is very small and can therefore lead to incorrect optimization results, since each projection then increases the detectability index by almost the same proportion. However, this finding can be useful in the pure detection task of a feature. Then the PW model observer can identify the presence of a feature with less projections than the NPW model observer. This also explains why the PW detectability index does not change very much when a new best projection is added. Then the model observer has already recognized the feature "sphere" and confirmed its presence. In the case of the NPW model observer, this finding seems to be confirmed only after several iterations, which of course yields very good results in the optimization as we need a good differentiation of the projections.

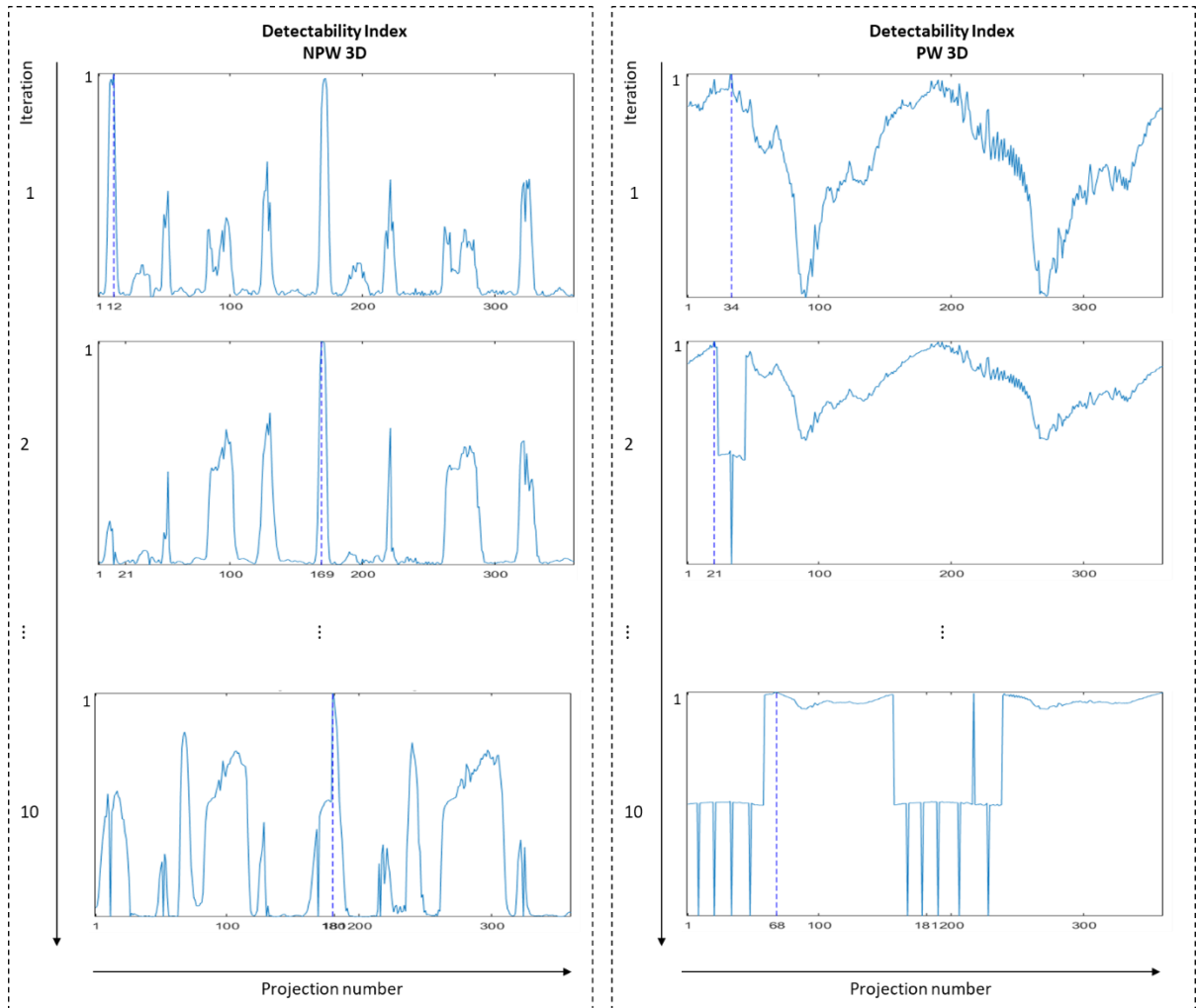


Figure 7.7: Map of the normalized detectability index for each iteration of the trajectory optimization algorithm. The detectability index is shown over all circular angles for both the PW and NPW model observers. In each iteration the projection with the highest detectability index is chosen. The dotted blue line indicates the selected projection

7.1.2 Feature 2: Cylinder

As a second feature, we will examine in this section the trajectory optimization for a cylinder. The cylinder is made of titanium and has a lower attenuation coefficient (0.742 cm^{-1}) compared to the phantom that is made of steel (1.5433 cm^{-1}). In the following, the cylinder is used to evaluate the model observers regarding a low-contrast feature. In the previous section 7.1.1, the evaluation was performed for a high-contrast feature because both the sphere and the phantom have identical attenuation coefficients.

- **Trajectory optimization with a set of 18 ideal projections:**

Figure 7.8 (C and D) shows the image reconstructions associated with the selected projections computed from the NPW and PW model observers compared to a full reconstruction with 360 projections (A) and a reconstruction with 18 uniformly distributed projections (B). With the standard trajectory (B) the cylinder completely disappears. The task-driven optimized trajectories (C and D) considerably outperform the equidistance trajectory, with the greatest improvement is observed in the three planes of the NPW-based optimization. The detectability index for the optimized trajectory increased by a factor of 1.21 and 1.41 respectively for the NPW and PW model observers compared to the standard circular orbit. Like shown in Table 7-2, both the NPW- and PW-based optimization improves the standard deviation by 72 % and 73 %, respectively.

Table 7-2: Quantitative evaluation of standard trajectories with 360 and 18 equidistant distributed projections and optimized trajectories for a set of 18 projections with NPW and PW model observers in comparison to the reference reconstruction with 2000 projections

	<i>Equi 360</i>	<i>Equi 18</i>	<i>Opt 18 (NPW)</i>	<i>Opt 18 (PW)</i>
<i>SD</i>	0.52	3.62	1.00	0.99
<i>RMSE</i>	0.54	3.97	2.08	4.71

Figure 7.8 (D) shows the geometrical deviation of the cylinder in planes parallel to the XY plane. The largest deviation occurs around the X-axis. This effect was also observed for the feature “sphere”, which is probably caused by the limited angular acquisition. Plotting the optimized trajectories against the standard equidistance trajectory in Figure 7.9, confirms these findings. This effect can also be observed in the XZ plane. We note that the cross-section of the cylinder is best reconstructed with the NPW model observer. In the PW-based reconstruction, the cross-section is bigger than it is in real.

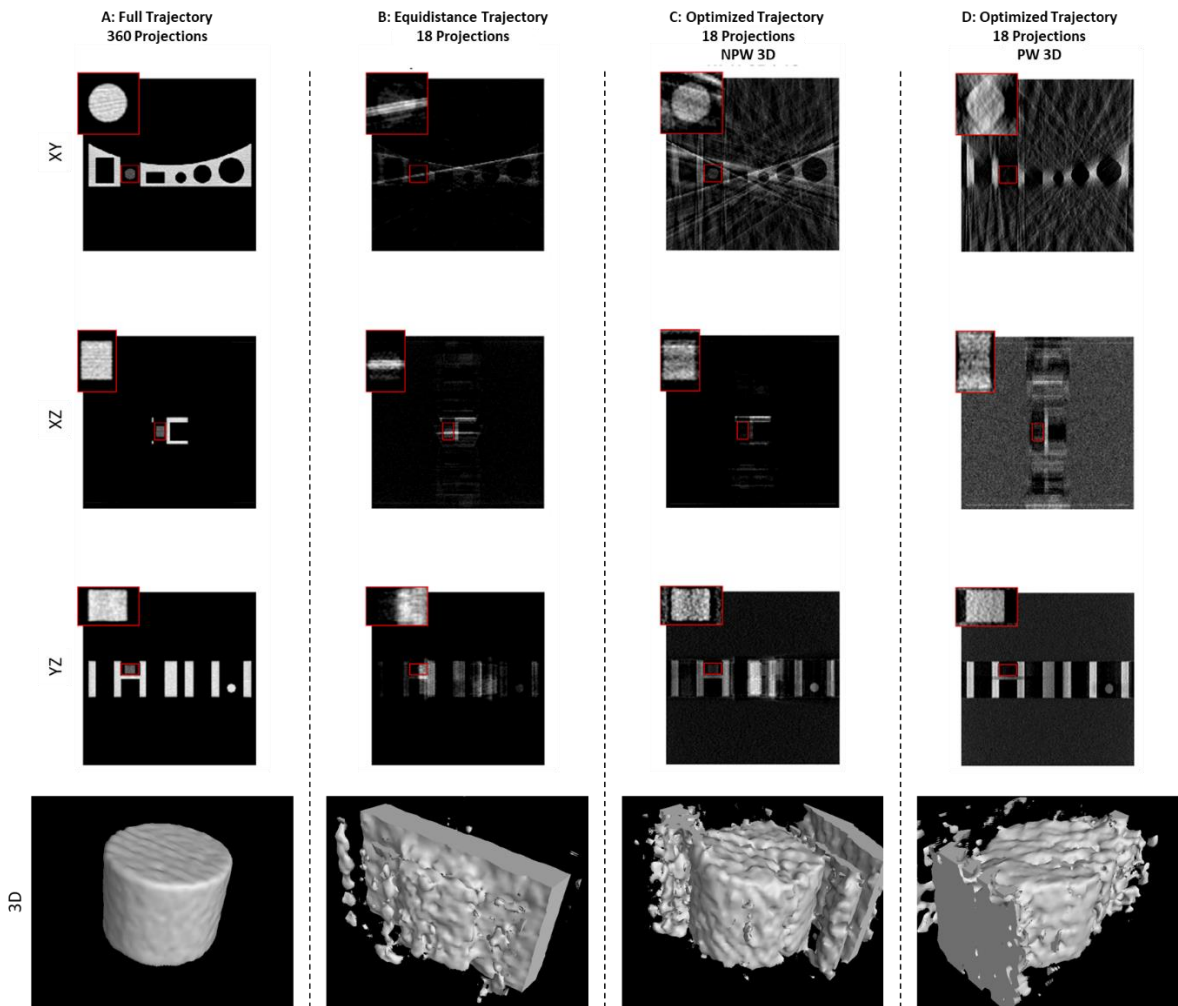


Figure 7.8: Four FDK reconstructions of the phantom with focus on the Cylinder are plotted. A: Reference reconstruction with 360 projections. B: Reconstruction with 18 equidistance distributed projections. C and D: Reconstructions with 18 projections selected based on the NPW and PW model observers, respectively

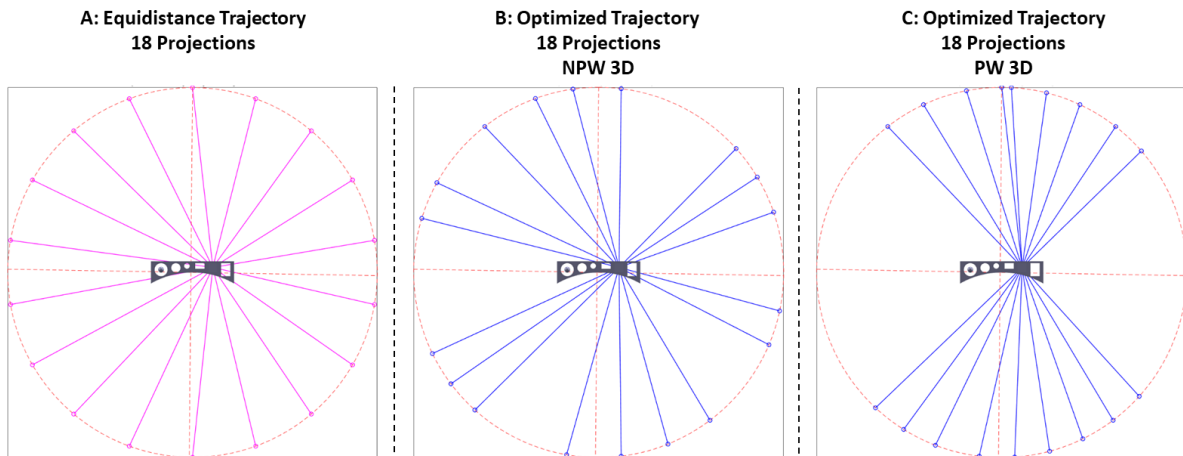


Figure 7.9: Illustration of the task-based optimized trajectories with 18 projections using the PW and NPW model observers for the feature “Cylinder”

For the feature “sphere”, we were able to achieve good reconstruction results even with only 8 projections (see Figure 7.2). For the cylinder, although we were able to improve the quality of the reconstruction with the identical number of projections compared to the standard trajectory (see Appendix C.1), it was still poor compared to the reference reconstruction. This also explains the bad values of RMSE. These were 3.81 and 4.83 for the NPW- and PW-based optimized trajectories, respectively. For a reconstruction with 360 projections, this value was only 0.54. To get the first good results with the optimization algorithm, we need at least 18 projections (see Figure 7.8). Two reasons can be decisive here:

First, the cylinder has a low attenuation coefficient and thus it appears with a low contrast in the reconstructed volume. Therefore, we need a higher number of projections to improve its contrast.

Secondly, the cylinder is geometrically a bit more complicated than the sphere, since in the three main orthogonal planes it gives two different cut surfaces than the sphere showing the same view in the three planes. If we cut off the cylinder with a plane at an angle (in a similar way to the geometry of the cone-beam), the result is an ellipse as a cutting curve.

- **Trajectory optimization with a set of 24 ideal projections:**

The reconstruction of the cylinder under three different trajectories with 24 projections is plotted in Figure 7.10. The SD metric is almost identical for both optimized trajectories (0.99 for NPW and 0.92 for PW). In the XY plane, brighter areas can be seen in the NPW-based reconstruction. This explains the slightly worse value of SD against the PW-based reconstruction. Compared to SD = 1.41 for the equidistant trajectory, this is still a very good improvement in terms of the data variation within the feature. However, referring to the agreement with the reference reconstruction, the NPW-based trajectory provides the better match: here we have RMSE = 1.68 for NPW and 4.08 for PW.

- **Trajectory optimization with a set of 90 ideal projections:**

In Figure 7.11 we see that the PW-based optimization delivers a slightly better reconstruction than the optimization based on the NPW model observer and the equidistant distributed acquisition with 90 projections. This is consistent with the results found for the feature “sphere” for a high number of ideal projections.

For SD and RMSE, we have identical values for both models. For the NPW-based optimization, SD and RMSE were 0.62 and 2.05, respectively. For the PW optimization SD and RMSE were 0.60 and 2.05 respectively. Although both models are quantitatively the same,

qualitatively the NPW model observer delivers slightly worse images: in the XY and XZ planes, an artifact in the form of a line is very well recognizable. This artifact lies in the Y-direction and probably appeared due to the absorption problems in this direction.

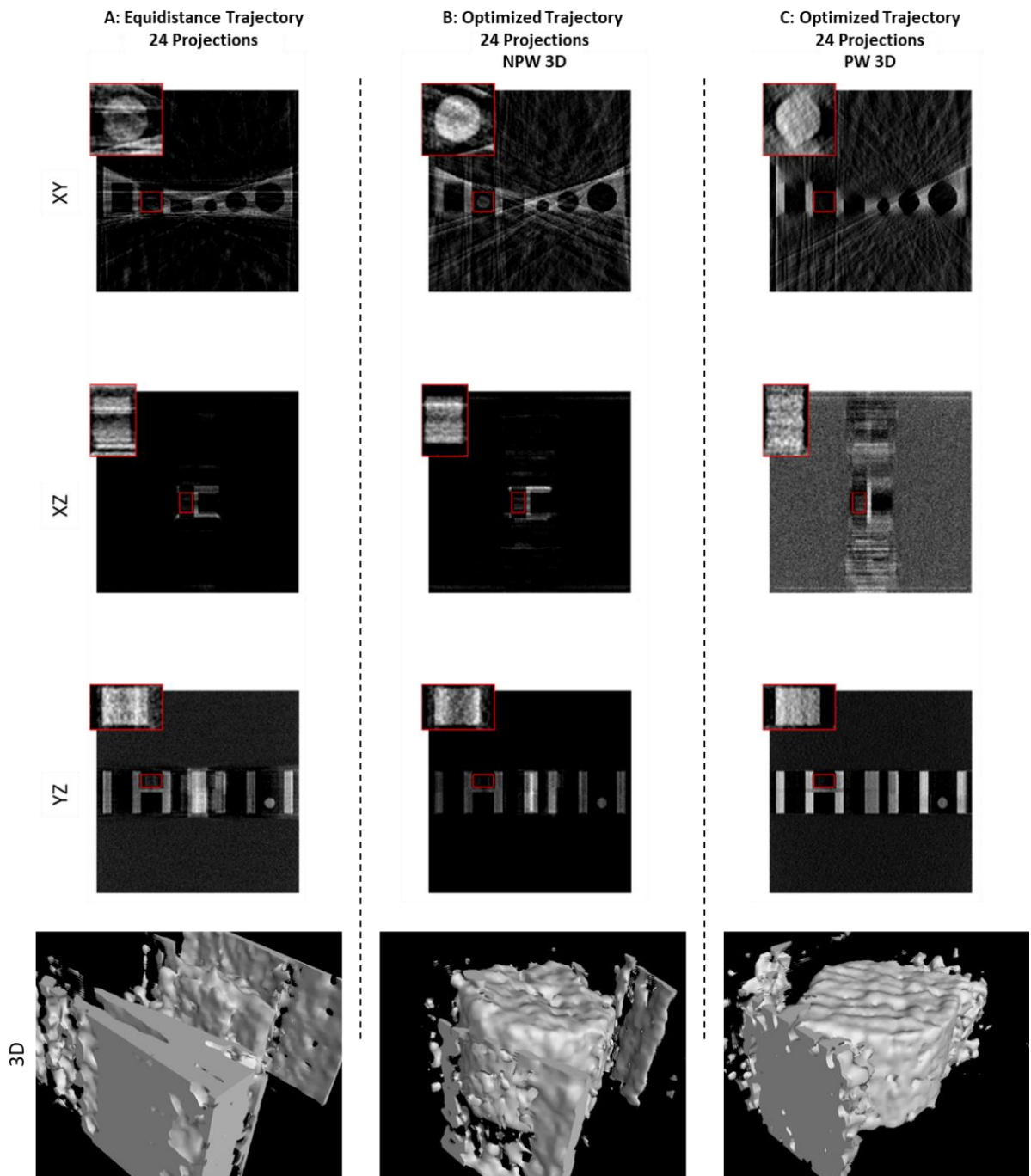


Figure 7.10: Trajectory optimization evaluated with 24 projections. As in Figure 7.8, both model observers improved considerably the quality of the reconstruction compared with a reconstruction with 24 equidistant distributed projections

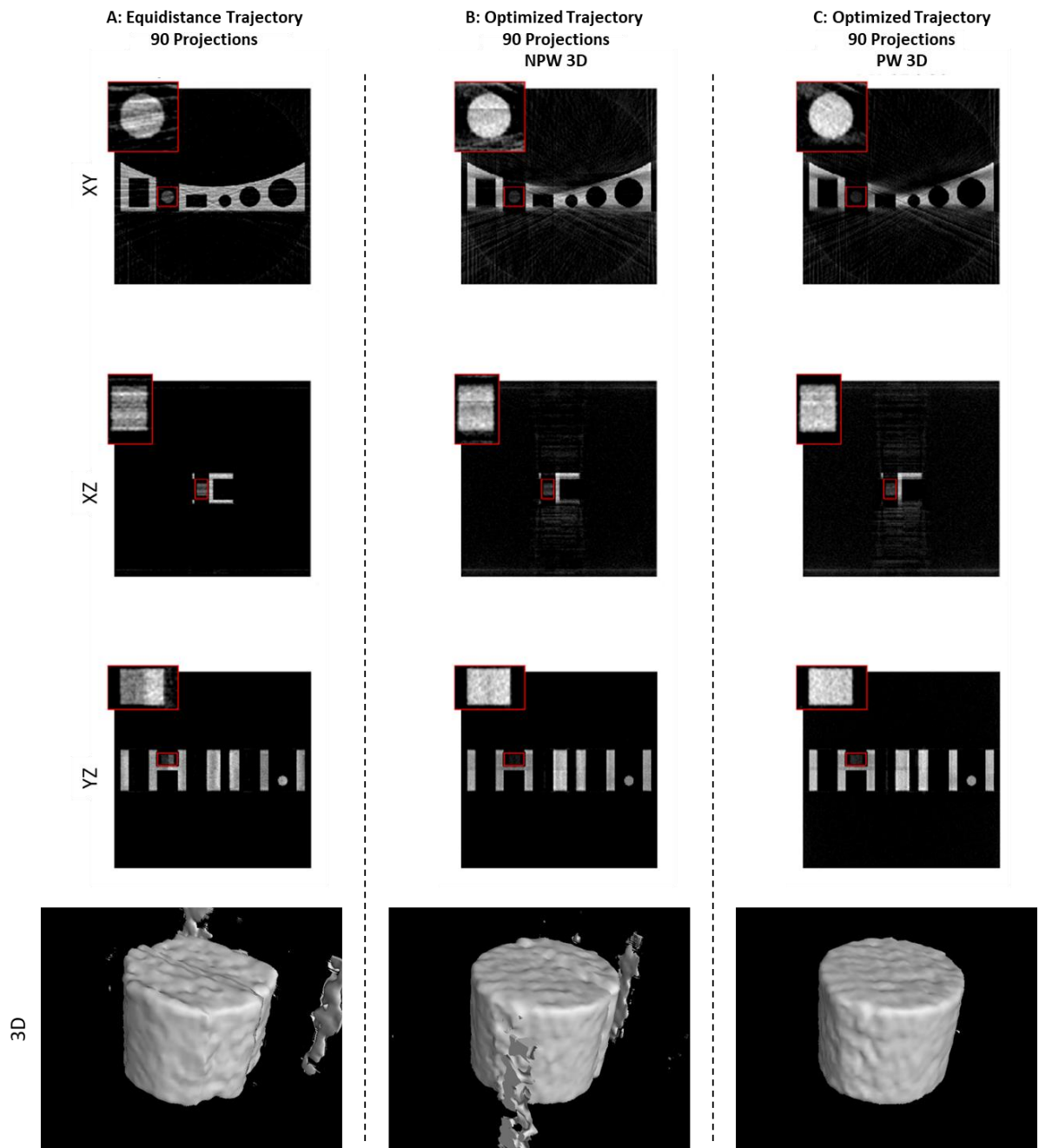


Figure 7.11: Trajectory optimization evaluated with 90 projections. For a high number of projections, the PW model observer improves the quality of the reconstruction better than the NPW model observer. The equidistance trajectory and the NPW-based optimized trajectory still show some artifacts

7.2 Trajectory Optimization for 2D features

In this section we present firstly the results of the trajectory optimization for the 2D feature "circle" with five different 2D model observers (NPW, NPWE, NPWEi, PW and PWEi). As in the previous section for 3D features, we will illustrate here only a part of the results for the following sets of projections: 18, 24 and 90 projections. The corresponding reconstructions are given in Figure 7.12. The optimization with the remaining sets can be found in Appendix D. Secondly, we evaluate the results of the PW- and NPW-based model observers with the CHO model observers. Our goal is to find out if such models are suitable for the trajectory optimization.

In order to investigate the influence of the eye filter and the internal noise on the Detectability Index, we consider the three NPW-based model observers (NPW, NPWE and NPWEi) and the other two PW-based model observers (PW and PWEi) separately. A quantitative evaluation of the selected trajectories is given in Table 7-3. The green mark indicates that the model observer in the first column would be the best choice according to the metrics or the CHO model observers in the first line.

NPW-based model observers:

For almost all sets of projections (small variations in the metrics are neglected), the NPW model observer has the best values for the standard deviation (SD). It means that the reconstruction with such a model has less noise around the feature. Based on the evaluation with RMSE, on the contrary, the NPWE model observer has yielded much better results in 6 out of 7 sets of projections (except for 90 projections). Thus, with this model, a good agreement with the reference reconstruction can be achieved. Especially with 120 projections, we could use the NPWE model observer to get a 50 % better RMSE value than the NPW model observer. For all CHO model observers, assuming a 5 % error variation in the values, we could observe a match with the RMSE values and thus also with the NPWE model observer. The NPWEi model observer has delivered the worst results.

PW-based model observers:

In the evaluation of the PW and PWEi model observers, we can observe a separation of the suitability of each model in certain ranges of the number of projections. At low numbers (up to 36 projections in our case), the PW model observer was better for both metrics (SD and RMSE). For a higher number of projections, it was rather the NPWEi model observer, which

then provided the better reconstruction quality. Both findings are also confirmed by the CHO models.

Table 7-3: Quantitative evaluation (SD and RMSE) of the optimized trajectories for different number of projections (N). The CHO model observers serve here to calculate the test statistic L for the set of projections selected by the NPW- or PW-based model observer

ModelObserver	N	CHO GB	CHO S-DOG	CHO D-DOG	CHO SQR	SD	RMSE
NPW	8	0,55	0,47	0,29	0,90	1,28	3,88
NPWE	8	0,82	0,90	0,45	1,42	1,29	3,24
NPWEi	8	0,83	0,86	0,42	1,36	1,65	3,43
NPW	18	0,82	0,60	0,39	1,22	0,89	3,61
NPWE	18	0,77	0,70	0,44	1,38	0,98	3,15
NPWEi	18	0,98	0,72	0,44	1,37	1,01	3,43
NPW	24	1,07	0,69	0,44	1,33	0,86	3,39
NPWE	24	0,82	0,72	0,44	1,33	0,96	3,21
NPWEi	24	1,18	0,78	0,48	1,42	0,90	3,23
NPW	36	0,94	0,66	0,42	1,28	0,80	3,21
NPWE	36	0,93	0,76	0,45	1,37	0,72	2,78
NPWEi	36	0,88	0,75	0,47	1,40	0,71	2,97
NPW	72	1,04	0,73	0,47	1,39	0,65	2,93
NPWE	72	1,27	1,03	0,55	1,57	1,18	2,63
NPWEi	72	1,05	0,81	0,50	1,53	0,70	3,22
NPW	90	1,82	1,14	0,65	1,92	0,57	2,41
NPWE	90	1,85	1,24	0,67	1,91	0,93	2,63
NPWEi	90	1,38	1,19	0,65	2,01	0,64	2,13
NPW	120	1,61	0,98	0,59	1,79	0,60	2,76
NPWE	120	1,85	1,91	0,82	2,27	0,59	1,42
NPWEi	120	1,63	0,88	0,55	1,63	0,68	3,04
PW	8	2,87	0,52	0,34	1,09	1,23	3,64
PWEi	8	1,39	0,55	0,35	1,04	1,35	3,78
PW	18	1,04	0,74	0,47	1,46	0,92	3,61
PWEi	18	1,17	0,81	0,44	1,37	0,86	3,76
PW	24	0,96	0,66	0,44	1,35	0,88	3,89
PWEi	24	0,91	0,63	0,42	1,27	0,93	3,94
PW	36	1,14	0,63	0,42	1,31	0,85	4,04
PWEi	36	0,89	0,65	0,43	1,33	0,81	3,87
PW	72	1,37	0,65	0,44	1,34	0,72	3,99
PWEi	72	1,52	0,82	0,51	1,53	0,69	2,72
PW	90	1,85	0,92	0,56	1,63	0,51	2,49
PWEi	90	2,10	1,27	0,65	1,83	0,65	1,72
PW	120	1,42	0,72	0,47	1,41	0,66	3,35
PWEi	120	1,60	0,83	0,52	1,51	0,62	2,50

To give a better illustration of the results, we graphically show in Appendix E the overall results for both metrics (SD and RMSE). The progressions of the individual graphs confirm what we have discussed in this section.

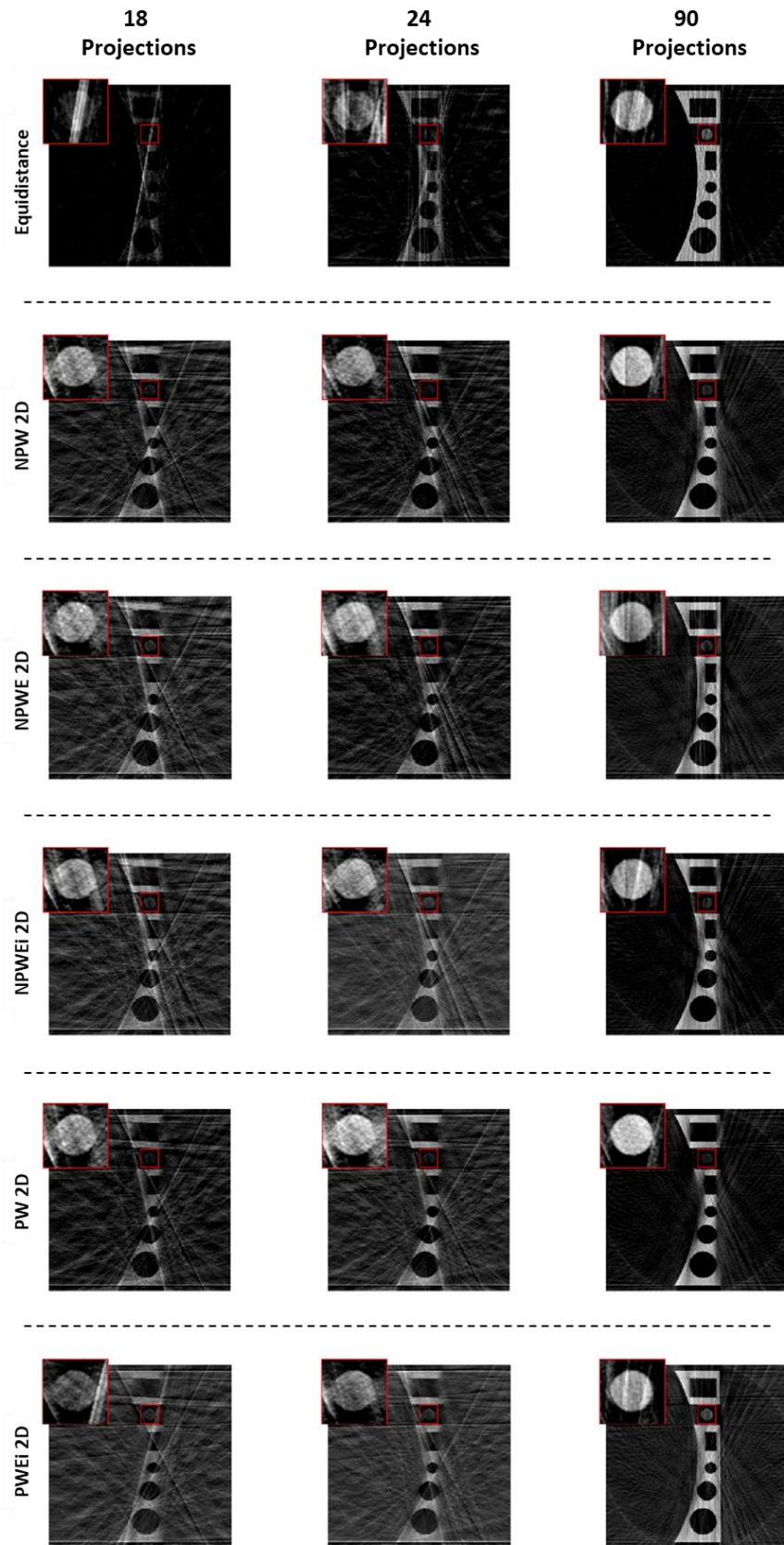


Figure 7.12: Reconstruction of a single slice with 18, 24 and 90 equidistant projections. The same slice is also reconstructed with 18, 24 and 90 optimized projections based on five different 2D model observers

8 Conclusions

Task-based trajectory optimization algorithm:

In this work we introduced a task-based trajectory optimization algorithm for an industrial CT application which incorporates CAD data of the object to be scanned. This optimization algorithm, which is implemented with different model observers successfully finds the set of ideal projections that have the highest amount of information for a feature inside the object and thus provides high quality of image reconstruction for the related region. This is often the case in many industrial applications where only a specific region-of-interest (or volume-of-interest) is relevant and has to be reconstructed with high image quality and preferably with few projections to significantly reduce the scan time.

Computing time:

Regarding the computing time of our proposed trajectory optimization algorithm, we have runtimes of only few minutes on a commercial workstation compared to several hours for a previous implementation in the literature [Fischer et al. 2016]. These speed-up improvements were necessary to evaluate different features with different model observers and for different set of projections in a reasonable amount of time. However, for an inline CT application, this optimization algorithm must be applied only once for an object, as the output can then be used many times for the same object series.

Trajectory optimization of high- vs. low-contrast 3D features:

As we have demonstrated in sections 7.1.1 and 7.1.2, the optimization algorithm delivers good results for features with high- and low-contrast. Especially the trajectory optimization of a low-contrast feature has considerably demonstrated the benefits of an optimized trajectory, as the standard trajectory requires more projections to successfully detect the low-contrast feature. For such features, the proposed optimization algorithm provides high quality of reconstruction by using fewer projections.

Trajectory optimization with low vs. high number of ideal projections for 3D features:

Generally, one can state that the NPW model observer is well suited to provide high image quality for the reconstruction with small numbers of projections selected by the proposed optimization algorithm. In contrast, the PW model observer showed good imaging results when optimizing over a large set of projections. Based on the qualitative metric SD, this change has occurred in about 72 projections for both the high and low-contrast features.

Trajectory optimization of a simple vs. more complex 3D features:

The findings for the trajectory optimization for high- and low-contrast features and for a lower and higher number of projections also apply to a slightly more complicated feature. What changes is that, for a satisfactory reconstruction, we need more projections than for a simpler feature. For the sphere, we were able to achieve good reconstruction quality with the first 8 optimized projections. For the cylinder this was not possible and only with 18 optimized projections the reconstruction was satisfactory.

Detection task:

The PW model observer is more sensitive towards a detection task. They can correctly (in our case) detect the presence of a feature with less projections than the NPW model observer. However, this high sensitivity can lead to false detection results. In order to investigate this, several objects with and without the feature need to be examined to qualitatively describe the number of false detections. However, this is not part of this work and can be investigated in a future study.

Analysis of the 2D model observers that incorporate the human perception:

For the trajectory optimization of 2D features, the model observers that incorporate the human perception have demonstrated in certain cases a discernible and qualitatively measured improvement over the purely mathematical PW and NPW model observers.

Based on SD as a metric, the NPW model observer was better for 6 out of the 7 sets of projections. However, if we consider RMSE as the assessment metric, then we find that the NPWE (thus adding the eye filter) provides the better match with the real part.

In the case of the PWEi model observer, an enhancement in the quality of the reconstruction for a high number of projections was observed. However, for a small set of projections (up to 36 projections) the PW model observer outperformed the PWEi model observer.

Here we can summarize that the anthropomorphic model observers are suitable for the trajectory optimization, but their application depends very much on the number of projections and on what goal is pursued: that is, whether we want less noise in the reconstruction or rather we want good agreement with the reference reconstruction.

Analysis of the Channelized Hotelling Observers (CHO) towards trajectory optimization:

The CHO model observers have demonstrated a very good agreement with the results from the quantitative analysis of the NPW and PW-based 2D model observers. Then the

qualitatively good reconstructions were always and with almost all the CHO model observers recognized. However, as we have adopted the design and the tuning of the channels from an earlier study, it would be highly advisable to optimize these parameters for each individual case to increase the quality of the optimization.

Possible extensions of the proposed optimization framework:

- The proposed trajectory optimization algorithm can be extended to include more arbitrary geometries (e.g., a 3D spherical trajectory instead of a simple circular orbit, variation of the source-object-distance (SOD) or the source-detector-distance (SDD), different magnifications of the X-ray source, etc.).
- The metrics MTF and NPS (see equations (5.71) and (5.72)) were measured locally at a single point, which is mostly the center of the feature. The validity of this approach was discussed in section 5.6.1, then for a small VOI both values change only very slightly within it. An important challenge would be to relate these metrics to the entire volume-of-interest rather than a single point when optimizing for a large feature. The calculation of the average values over VOI could be an option.
- For simplicity, the regularization strength parameter β was considered as constant. However, previous work [Gang et al. 2014] showed that the implementation of a regularization map with a spatially-varying parameter could be helpful to determine the detectability index.
- In general, our optimization algorithm has delivered very good results for simulated data. Next, it would be important to test the algorithm for real measurements as well. Then in a real measurement, various types of artifacts can occur, which we have only added up to a certain amount in the simulated data. In addition, the misalignment between the real and simulated trajectories can also have an impact. Then we would optimize in the wrong place, which can provide suboptimal projection choices. This also offers the possibility to perform a sensitivity analysis for the optimization algorithm against geometrical variations of the trajectory or even of the object itself.
- In this work we focused on the optimization of the trajectory. In order to further improve the quality of the reconstruction, it would be optimal to combine our results

with further measures for the optimization of the reconstruction algorithm or the reconstruction itself. In addition, we reconstructed the selected projections using the FDK method. However, for the determination of the parameters MTF and NPS, we used the PL approach. Therefore, it is advisable to integrate the PL reconstruction into our algorithm in order to achieve the optimal image quality. This method also offers more freedom in the parameter design and is more suitable for the reconstruction of arbitrary trajectories than the FDK method, especially if we extend the optimization to a 3D trajectory.

- In this work we examined three different task functions: 3D sphere, 3D cylinder and 2D circle. These features are a bit simpler than what can be found in a complex industrial component. Therefore (like proposed above), the validity of this optimization algorithm should be tested on real applications or more complex task functions like cracks or other defects in the material.
- In section 7.2 we have optimized the trajectory to the middle circle of the cylinder. A couple of 2D model observers have delivered very good reconstruction quality and that with just a few projections. Of course, this is because we do not consider the entire structure of the cylinder, but just a 2D slice. This offers the possibility for the cylinder to optimize the trajectory for each of its 2D slice and then add the selected projections together. That could be particularly purposeful and qualitatively much better for very complex features.

Bibliography

- Abbey, Craig K., Barrett, Harrison H.: Human- and model-observer performance in ramp-spectrum noise: effects of regularization and object variability, In: *J. Opt. Soc. Am. A* (18), p. 473–488, 2001.
- Andersen, A. H., Kak, A. C.: Simultaneous Algebraic Reconstruction Technique (SART): A superior implementation of the ART algorithm, In: *Ultrasonic Imaging* (6), p. 81–94, 1984.
- Archibald, Neil K., Clarke, Michael P., Mosimann, Urs P., Burn, David J.: The retina in Parkinson's disease, In: *Brain: a journal of neurology* (132), p. 1128–1145, 2009.
- Batenburg, K. Joost, Palenstijn, Willem Jan, Balázs, Péter, Sijbers, Jan: Dynamic Angle Selection in Binary Tomography, In: *Comput. Vis. Image Underst.* (117), p. 306–318, Elsevier Science Inc., New York 2012.
- Bouwman, Ramona W., van Engen, Ruben E., Dance, David R., Young, Kenneth C., Veldkamp, Wouter J. H.: Evaluation of Human Contrast Sensitivity Functions Used in the Non-prewhitening Model Observer with Eye Filter, In: *Fujita H., Hara T., Muramatsu C. (eds) Breast Imaging* (8539), p. 715–722, Springer-Verlag, 2014.
- Brankov, Jovan G.: Evaluation of the channelized Hotelling observer with an internal-noise model in a train-test paradigm for cardiac SPECT defect detection, In: *Physics in medicine and biology* (58), p. 7159–7182, 2013.
- Burgess, Arthur E., Li, Xing, Abbey, Craig K.: Visual signal detectability with two noise components: anomalous masking effects, In: *J. Opt. Soc. Am. A* (14), 1997.
- Buzug, Thorsten: Computed Tomography. From Photon Statistics to Modern Cone-Beam CT, Springer-Verlag, Berlin, Heidelberg 2008.
- Desai, Nikunj, Singh, Abhinav, Valentino, Daniel: Practical Evaluation of Image Quality in Computed Radiographic (CR) Imaging Systems, In: *Proceedings of SPIE-The International Society for Optical Engineering* (7622), 2010.
- Dremel, Kilian: Modellbildung des Messprozesses und Umsetzung eines modellbasierten iterativen Lösungsverfahrens der Schnittbild-Rekonstruktion für die Röntgen-Computertomographie. Dissertation, Julius-Maximilians-Universität Würzburg, Würzburg 2017.
- Ebensperger, Thomas K.: Konzeption, Umsetzung und Evaluierung eines linsenlosen Röntgenmikroskopes. Dissertation, Julius-Maximilians-Universität Würzburg, Würzburg 2014.
- Ferrero, Andrea, Favazza, Christopher P., Yu, Lifeng, Leng, Shuai, McCollough, Cynthia H.: Practical implementation of Channelized Hotelling Observers: Effect of ROI size, In: *Proceedings of SPIE-the International Society for Optical Engineering* (10132), 2017.

- Fischer, Andreas: CT Reconstruction with Object Specific Non-Standard Trajectories. Master thesis, Technical University of Munich, Munich 2014.
- Fischer, Andreas, Lasser, Tobias, Schrapp, Michael, Stephan, Jürgen, Noël, Peter B.: Object Specific Trajectory Optimization for Industrial X-ray Computed Tomography, In: *Nature Scientific reports* (6), 2016.
- Fraunhofer EZRT: Web Page of Manufacturer, Accessed on 01.04.2019, Available from: <https://www.iis.fraunhofer.de/de/profil/jb/2018/roentgen-von-ueberall>
- Gang, Grace, Wang, Wenying, Mathews, Aswin, Siewerssen, Jeffrey H., Stayman, Webster J.: Task-Driven Imaging on an Experimental CBCT Bench: Tube Current Modulation and Regularization Design, In: *Proceedings of the International Meeting on Fully Three-Dimensional Image Reconstruction in Radiology and Nuclear Medicine*, p. 708–714, 2017.
- Gang, Grace J.: Task-Based Imaging Performance in 3D X-Ray Tomography: Noise, Detectability, and Implications for System Design. Dissertation, University of Toronto, Toronto 2014.
- Gang, Grace J., Lee, Junghoon, Stayman, J. Webster, Tward, Daniel J., Zbijewski, W., Prince, Jerry L., Siewerssen, Jeffrey H.: Analysis of Fourier-domain task-based detectability index in tomosynthesis and cone-beam CT in relation to human observer performance, In: *Medical physics* (38), p. 1754–1768, 2011.
- Gang, Grace J., Siewerssen, Jeffrey H., Stayman, J. Webster: Task-Based Design of Fluence Field Modulation in CT for Model-Based Iterative Reconstruction, In: *Conference proceedings. International Conference on Image Formation in X-Ray Computed Tomography* (2016), p. 407–410, 2016.
- Gang, Grace J., Stayman, J. Webster, Zbijewski, Wojciech, Siewerssen, Jeffrey H.: Task-based detectability in CT image reconstruction by filtered backprojection and penalized likelihood estimation, In: *Medical physics* (41), 2014.
- Gordon, Richard, Bender, Robert, Herman, Gabor T.: Algebraic Reconstruction Techniques (ART) for three-dimensional electron microscopy and X-ray photography, In: *Journal of Theoretical Biology* (29), p. 471–481, 1970.
- Heeger, David: Signal Detection Theory (Lecture Notes in Neural Science), New York University, New York 1997.
- Herminso, Villarraga-Gómez, Smith, Stuart T.: Optimal Specimen Orientation in Cone-beam X-ray CT Systems (For Dimensional Metrology), In: *American Society for Precision Engineering*, p. 509–515, 2015.

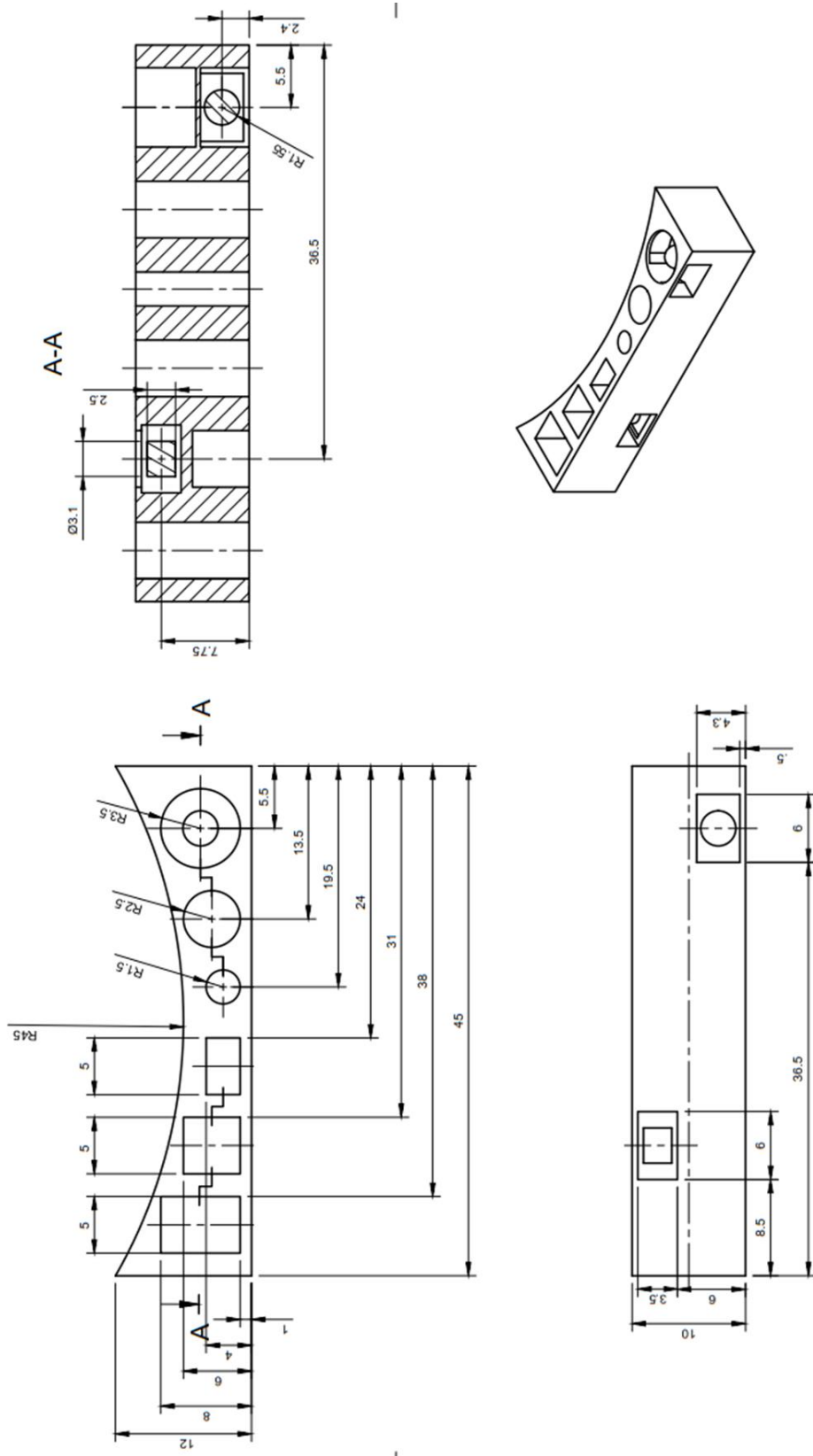
- Hutchison, David, Kanade, Takeo, Kittler, Josef, Kleinberg, Jon M., Kobsa, Alfred, Mattern, Friedemann et al.: Breast Imaging (Lecture Notes in Computer Science), Springer International Publishing, Cham 2014.
- Ishida, M., Doi, K., Loo, L. N., Metz, C. E., Lehr, J. L.: Digital image processing: effect on detectability of simulated low-contrast radiographic patterns, In: *Radiology* (150), p. 569–575, 1984.
- Krimmel, Sven: Limited view angle tomography for single material objects in non-destructive testing with X-rays. Dissertation, Technical University of Munich, Munich 2006.
- Lee, Seung-Wan, Lee, Chang-Lae, Cho, Hyo-Min, Park, Hye-Suk, Kim, Dae-Hong, Choi, Yu-Na, Kim, Hee-Joung: Effects of Reconstruction Parameters on Image Noise and Spatial Resolution in Cone-beam Computed Tomography, In: *J. Korean Phy. Soc.* (59), p. 2825–2832, 2011.
- Li, Ke, Garrett, John, Chen, Guang-Hong: Correlation between human observer performance and model observer performance in differential phase contrast CT, In: *Medical physics* (40), 2013.
- Myers, Kyle J., Barrett, Harrison H.: Addition of a channel mechanism to the ideal-observer model, In: *J. Opt. Soc. Am. A* (4), p. 2447–2457, 1987.
- Ott, Julien: Iterative reconstruction in CT: Using mathematical model observers to determine low dose images' trustworthiness. Dissertation, University of Lausanne, Lausanne 2016.
- Ouadah, S., Jacobson, M., Stayman, J. W., Ehtiati, T., Weiss, C., Siewerdsen, J. H.: Task-Driven Orbit Design and Implementation on a Robotic C-Arm System for Cone-Beam CT, In: *Proceedings of SPIE-the International Society for Optical Engineering* (10132), 2017.
- Petrov, Dimitar, Marshall, Nicholas W., Young, Kenneth C., Bosmans, Hilde: Systematic approach to a channelized Hotelling model observer implementation for a physical phantom containing mass-like lesions: Application to digital breast tomosynthesis, In: *Physica medica PM* (58), p. 8–20, 2019.
- Placidi, G., Alecci, M., Sotgiu, A.: Theory of adaptive acquisition method for image reconstruction from projections and application to EPR imaging, In: *Journal of Magnetic Resonance Series B*, p. 50–57, 1995.
- Racine, Damien, Viry, Anaïs, Becce, Fabio, Schmidt, Sabine, Ba, Alexandre, Bochud, François O. et al.: Objective comparison of high-contrast spatial resolution and low-contrast detectability for various clinical protocols on multiple CT scanners, In: *Medical physics* (44), p. 153-163, 2017.
- Russo, Paolo: Handbook of X-ray imaging. Physics and technology (Series in medical physics and biomedical engineering), CRC Press, Boca Raton 2017.

- Samei, Ehsan, Robins, Marthony, Chen, Baiyu, Agasthya, Greeshma: Estimability index for volume quantification of homogeneous spherical lesions in computed tomography, In: *Journal of medical imaging* (5), 2018.
- Schoener, Karsten: Development of Methods for Scatter Artifact Correction in Industrial X-ray Cone-beam Computed Tomography. Dissertation, Technical University of Munich, Munich 2012.
- Schrapp, Michael Johannes: Multi Modal Data Fusion in Industrial X-ray Computed Tomography. Dissertation, Technical University of Munich, Munich 2015.
- Siemens: CERA User Manual Version 4.1.0, 2016.
- Stayman, J. W., Siewerdsen, J. H.: Task-Based Trajectories in Iteratively Reconstructed Interventional Cone-Beam CT, In: *Proceedings of the International Meeting on Fully Three-Dimensional Image Reconstruction in Radiology and Nuclear Medicine*, p. 257–260, 2013.
- Stayman, J. W., Zbijewski, W., Otake, Y., Uneri, A., Schafer, S., Lee, J. et al.: Penalized-likelihood reconstruction for sparse data acquisitions with unregistered prior images and compressed sensing penalties, In: *Proceedings of SPIE-The International Society for Optical Engineering*, 2011.
- Stayman, J. Webster, Fessler, Jeffrey A.: Efficient calculation of resolution and covariance for penalized-likelihood reconstruction in fully 3-D SPECT, In: *IEEE transactions on medical imaging* (23), p. 1543–1556, 2004.
- Stayman, J. Webster, Otake, Yoshito, Prince, Jerry L., Khanna, A. Jay, Siewerdsen, Jeffrey H.: Model-based tomographic reconstruction of objects containing known components, In: *IEEE transactions on medical imaging* (31), p. 1837–1848, 2012.
- Suresh, P., M.Suganthi, M., Senthilraja, S.: Noise Reduction in Computed Tomography Image Using WB-Filter, In: *International Journal of Scientific & Engineering Research*, p. 243–247, 2014.
- Tseng, Hsin-Wu: Task-Based Image Quality Assessment in X-Ray Computed Tomography. Dissertation, University of Arizona, Tucson 2015.
- Uneri, A., Zhang, X., Yi, T., Stayman, J. W., Helm, P. A., Theodore, N., Siewerdsen, J. H.: Image quality and dose characteristics for an O-arm intraoperative imaging system with model-based image reconstruction, In: *Medical physics* (45), p. 4857–4868, 2018.
- Vaishnav, J. Y., Jung, W. C., Popescu, L. M., Zeng, R., Myers, K. J.: Objective assessment of image quality and dose reduction in CT iterative reconstruction, In: *Medical physics* (41), 2014.
- Vennart, W.: ICRU Report 54: Medical imaging—the assessment of image quality, In: *Radiography* (3), p. 243–244, Elsevier, 1997.

- Vogel, Jakob, Lasser, Tobias, Gardiazabal, José, Navab, Nassir: Trajectory optimization for intra-operative nuclear tomographic imaging, In: *Medical Image Analysis* (17), p. 723–731, Elsevier, 2013.
- Wagner, Robert, Weaver, Kenneth: An Assortment Of Image Quality Indexes For Radiographic Film-Screen Combinations - Can They Be Resolved?, In: *Application of Optical Instrumentation* (35), p. 83–94, 1972.
- Williams, Charles Sumner, Becklund, Orville A.: Introduction to the optical transfer function, SPIE Press, Bellingham, Washington 2002.
- Wunderlich, Adam, Noo, Frédéric: Evaluation of the impact of tube current modulation on lesion detectability using model observers, In: *30th Annual International Conference of the IEEE Engineering in Medicine and Biology Society*, p. 2705–2708, 2008.
- Xue, Lin, Suzuki, Hiromasa, Ohtake, Yutaka, Fujimoto, Hiroyuki, Abe, Makoto, Sato, Osamu, Takatsuji, Toshiyuki: Numerical Analysis of the Feldkamp–Davis–Kress Effect on Industrial X-Ray Computed Tomography for Dimensional Metrology, In: *Journal of Computing and Information Science in Engineering* (15), ASME, 2015.
- Yendiki, A., Fessler, J. A.: Analysis of observer performance in detecting signals with location uncertainty for regularized tomographic image reconstruction, In: *Conference: Nuclear Science Symposium Conference Record, 2004 IEEE Volume (4)*, p. 2620–2624, 2004.
- Yendiki, Anastasia, Fessler, Jeffrey A.: Analysis of observer performance in known-location tasks for tomographic image reconstruction, In: *IEEE transactions on medical imaging* (25), p. 28–41, 2006.
- Zhang, Ge Lu: Numerical Observers for the Objective Quality Assessment of Medical Images. Dissertation, Université d'Angers, Angers 2014.
- Zhao, Chumin, Kanicki, Jerzy: Task-Based Modeling of a 5k Ultra-High-Resolution Medical Imaging System for Digital Breast Tomosynthesis, In: *IEEE transactions on medical imaging* (36), p. 1820–1831, 2017.
- Zheng, Ziyi, Mueller, Klaus: Identifying sets of favorable projections for few-view low-dose cone-beam CT scanning, In: *11th international meeting on "Fully three-dimensional image reconstruction in radiology and nuclear medicine"*, p. 314–317, 2011.
- Zikuan, Chen, Ruola, Ning: Volume fusion for two-circular-orbit cone-beam tomography, In: *Appl. Opt.* (45), p. 5960–5966, 2006.

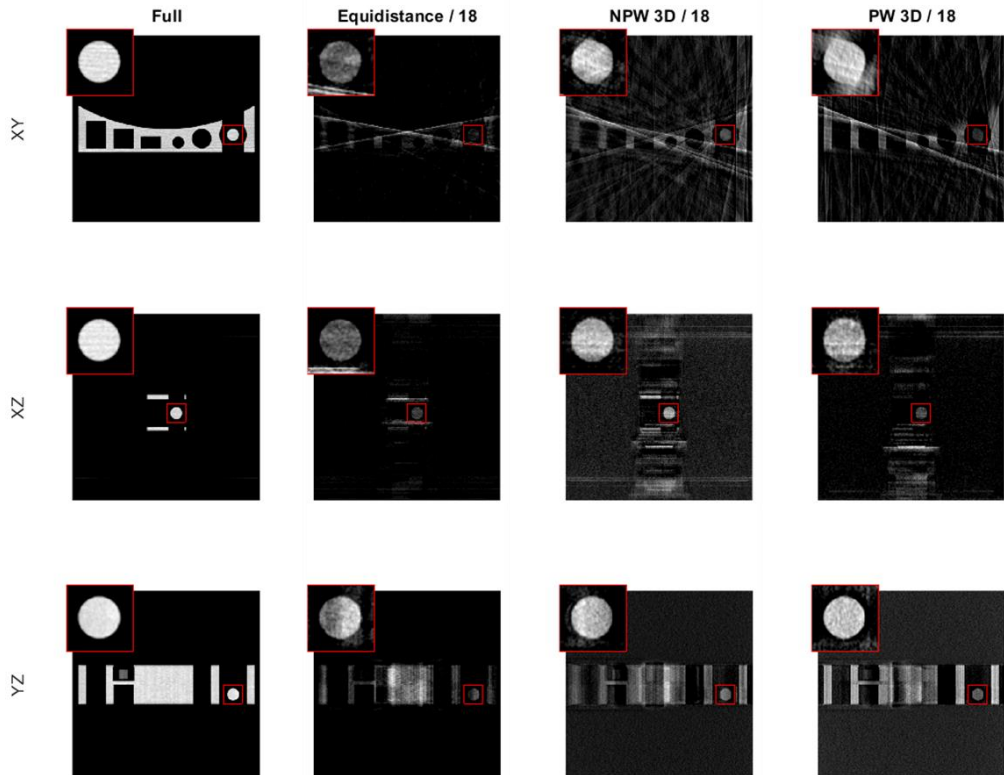
Appendix

Appendix A: Dimensions of the used phantom. The phantom is composed of three parts: The body, a sphere and a cylinder. Measurements are given in millimeters

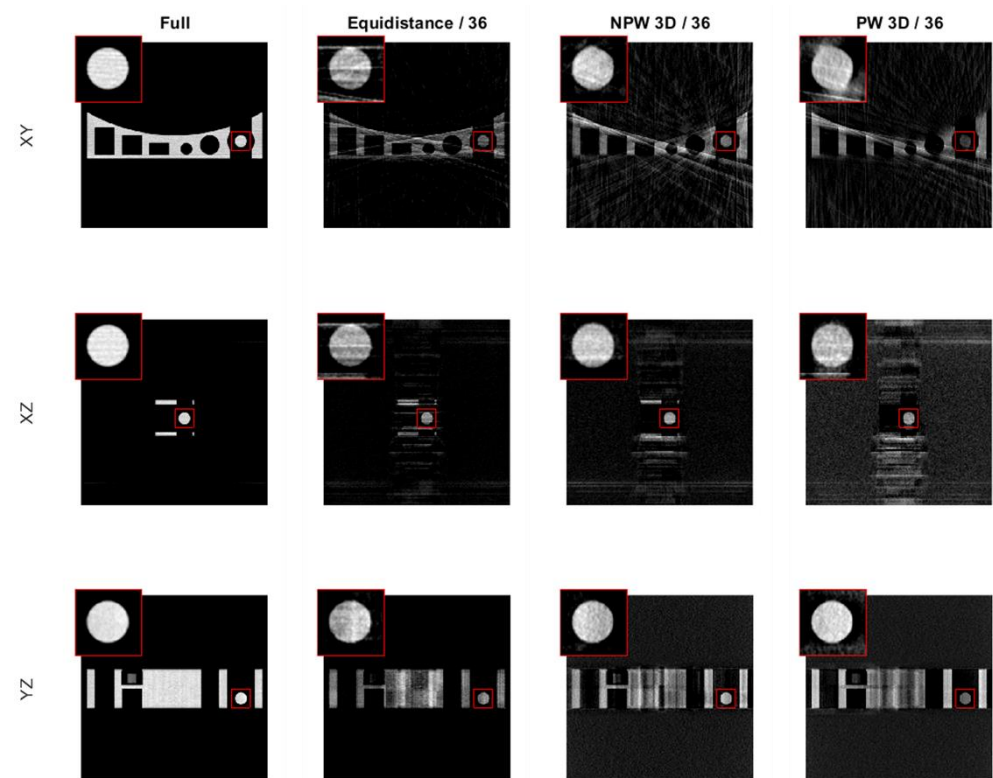


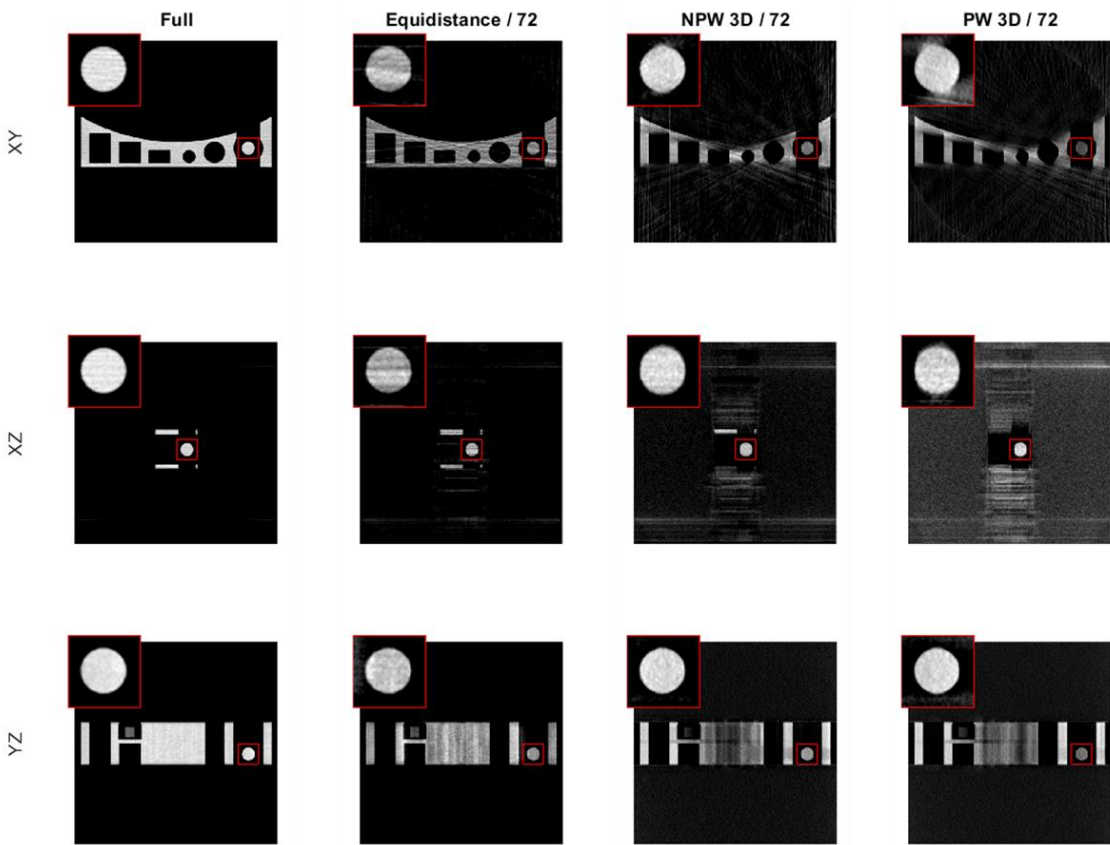
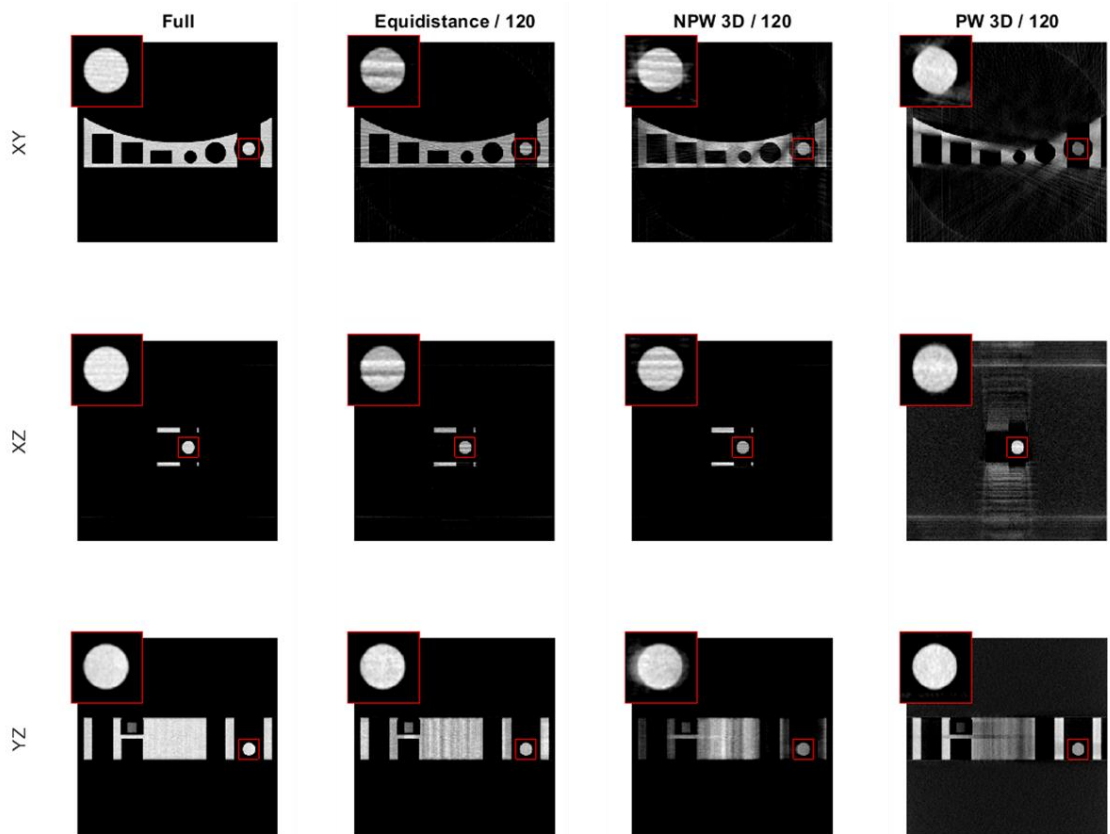
Appendix B: Results of the trajectory optimization for the sphere as feature for different number of ideal projections and for two different 3D model observers

Appendix B.1: Reconstruction of the sphere with 18 ideal projections



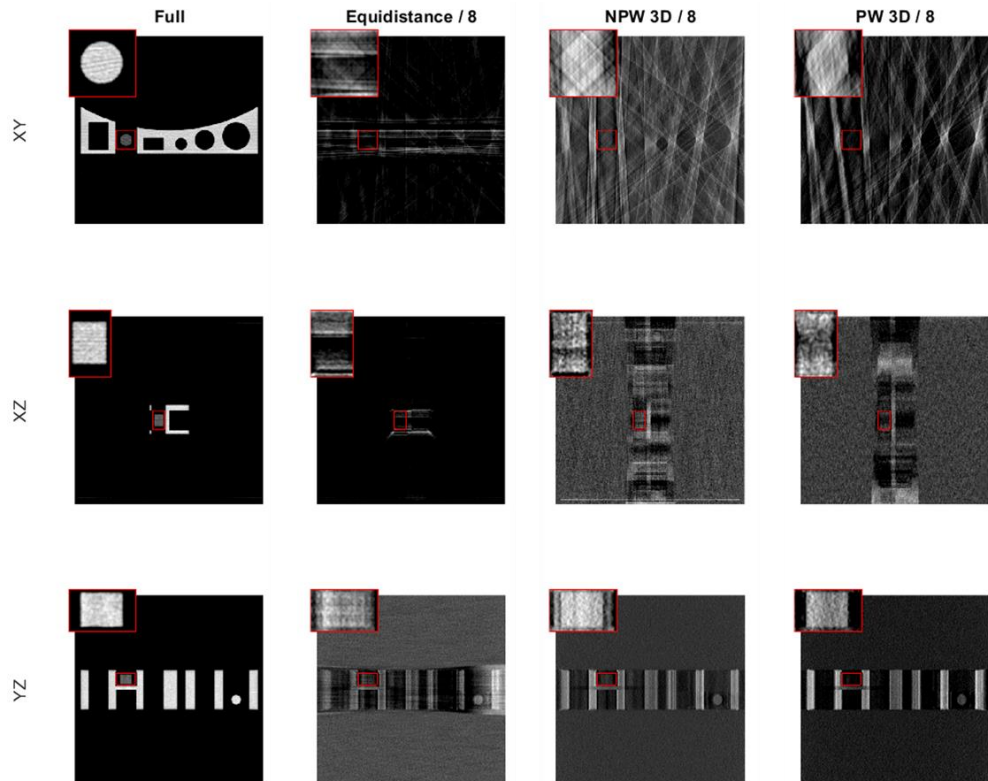
Appendix B.2: Reconstruction of the sphere with 36 ideal projections



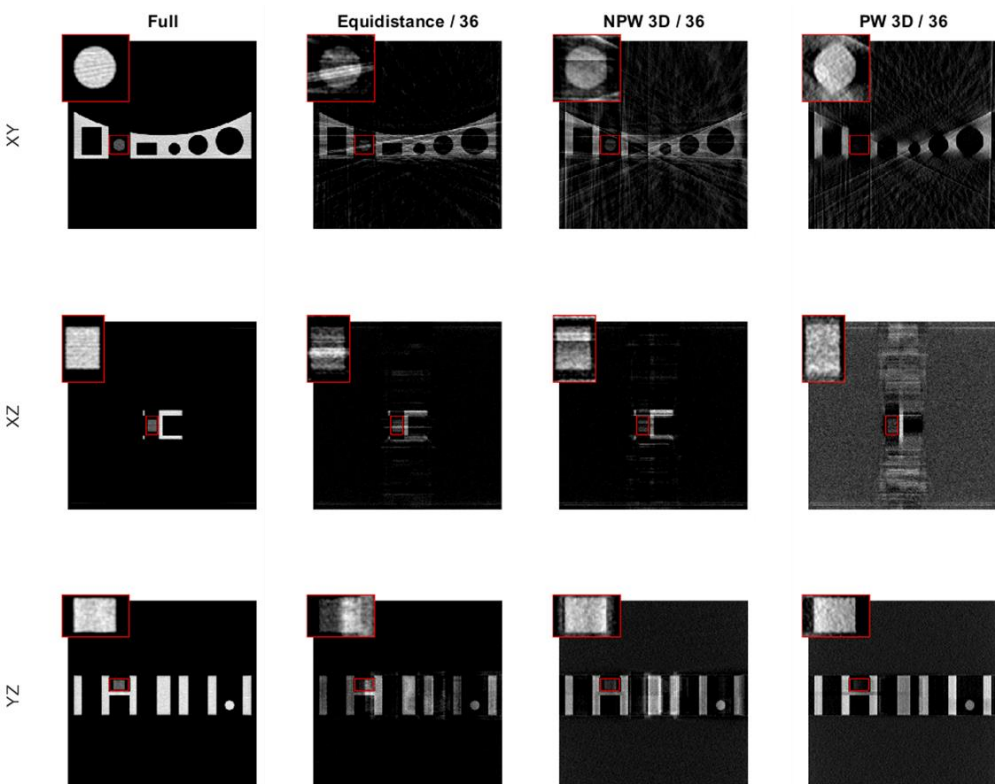
Appendix B.3: Reconstruction of the sphere with 72 ideal projections**Appendix B.4:** Reconstruction of the sphere with 120 ideal projections

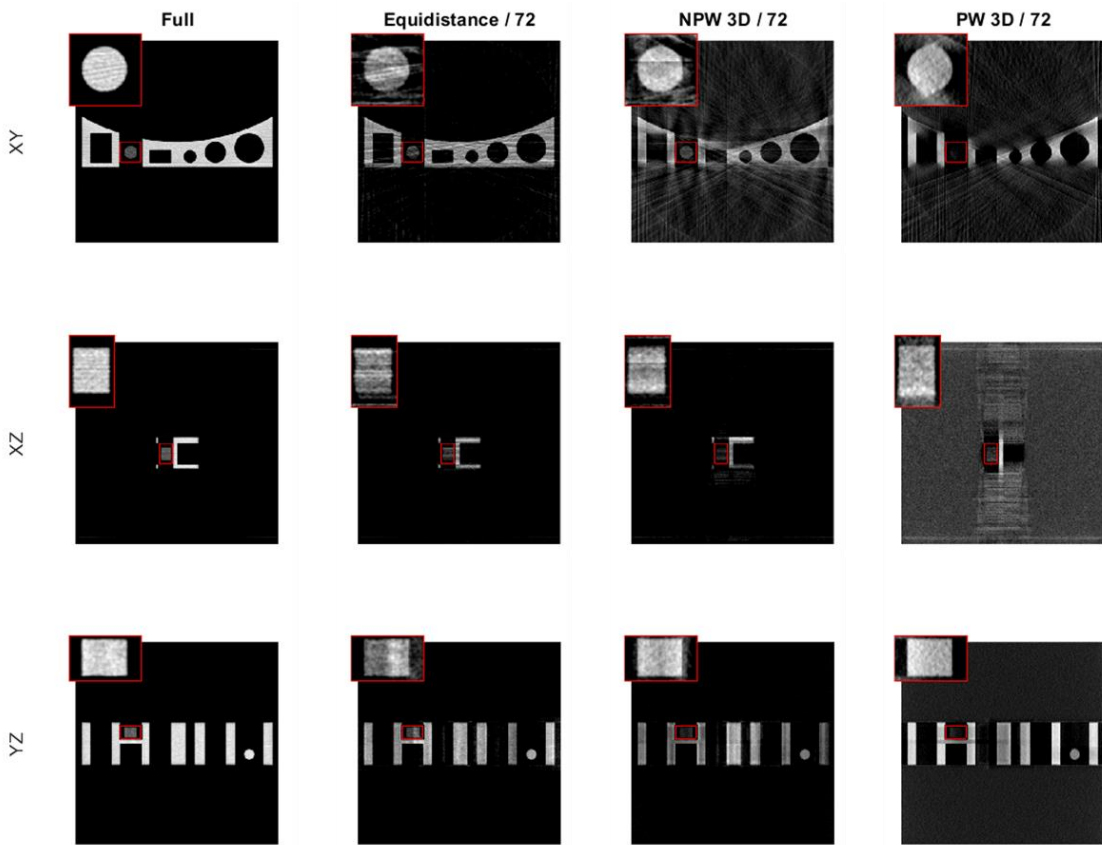
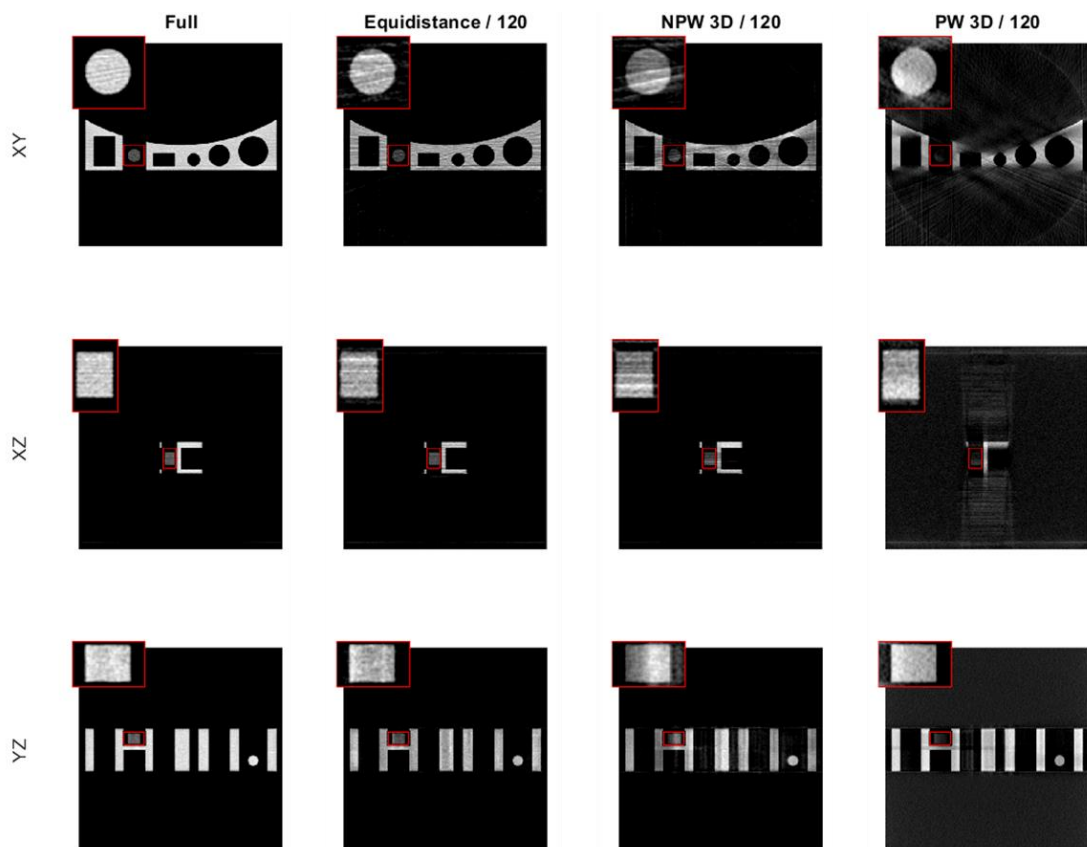
Appendix C: Results of the trajectory optimization for the cylinder as feature for different number of ideal projections and for two different 3D model observers

Appendix C.1: Reconstruction of the cylinder with 8 ideal projections

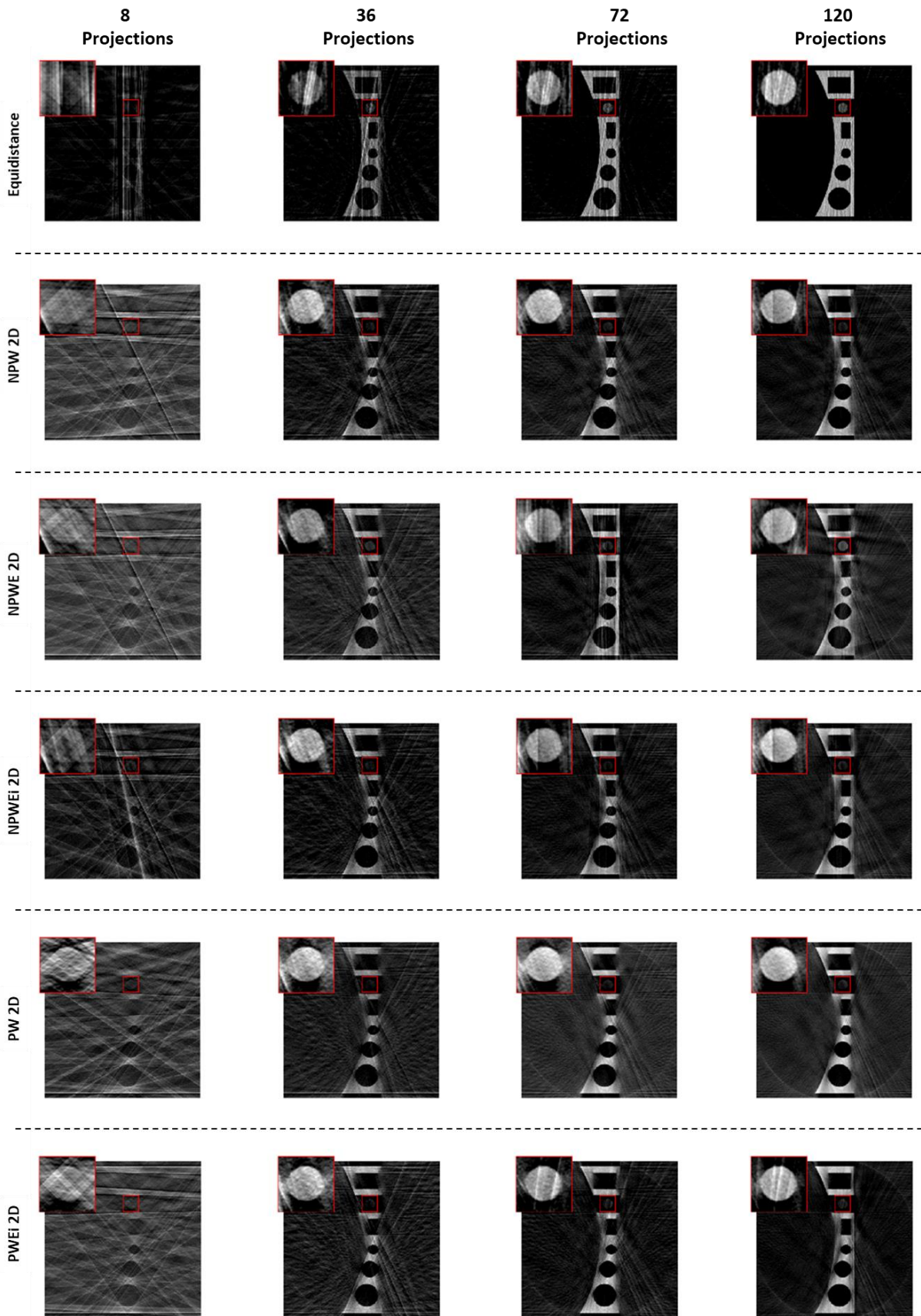


Appendix C.2: Reconstruction of the cylinder with 36 ideal projections



Appendix C.3: Reconstruction of the cylinder with 72 ideal projections**Appendix C.4: Reconstruction of the cylinder with 120 ideal projections**

Appendix D: Results of the trajectory optimization for the circle as feature for different number of ideal projections and for five different 2D model observers



Appendix E: Results of the evaluation (SD and RMSE) of the trajectory optimization for the circle as feature for different number of ideal projections and for five different 2D model observers

